The Pennsylvania State University

The Graduate School

John and Willie Leone Family Department of Energy and Mineral Engineering

A COMPARISON OF PATCHY SATURATION VELOCITY MODELS TO ULTRASONIC TESTS

A Thesis in

Energy and Mineral Engineering

by

Giancarlo Bonotto

Submitted in Partial Fulfillment

of the Requirements

for the Degree of

Master of Science

August 2016

The thesis of Giancarlo Bonotto was reviewed and approved* by the following:

Eugene C. Morgan
Assistant Professor of Petroleum and Natural Gas Engineering
Thesis Co-Advisor

Zuleima T. Karpyn
Professor of Petroleum and Natural Gas Engineering;
Quentin E. and Louise L. Wood Faculty Fellow in Petroleum and Natural Gas Engineering;
Thesis Co-Advisor

Derek Elsworth
Professor of Energy and Geo-Environmental Engineering

*Signatures are on file in the Graduate School

ABSTRACT

Characterization and monitoring of underground reservoir properties is of paramount importance for a multitude of disciplines. Acoustic wave velocity measurements, like in seismic surveys and well logs, are one of the most attractive approaches to gather information about reservoirs, as they provide reliable information with the needed spatial coverage and resolution required for many applications. Yet, the estimation of this parameter in partially saturated rocks can be a challenging assignment due to uncertainties associated with heterogeneities in fluid saturation. In order to analyze and interpret field data at partial saturation conditions, patchy saturation models are used to perform fluid substitution simulations, although commonly some of their underlying assumptions are deliberately ignored. Therefore, this work aims to experimentally investigate the performance of widely used patchy models (Gassmann-Voigt, White's spherical and White et al. layered model) at controlled patchy saturation conditions. Patchy saturated samples were created in the laboratory using a simple saturating and stacking methodology and submitted to ultrasonic tests at two wave frequencies (100 and 250 kHz). From the laboratory data and predictions of the models, it was found that the models based on Biot's theory seem to perform better, as they presented errors smaller than Gassmann-Voigt and are based on more realistic assumptions. Moreover, a simpler velocity average method appears to perform just as well, if not better, than these more complex and commonplace models, since it presented the smallest deviations from the experimentally measured velocities.

TABLE OF CONTENTS

LIST OF FIGURES

LIST OF TABLES

ACKNOWLEDGEMENTS

First, I would like to express my sincere gratitude to my advisors, Dr. Eugene C. Morgan and Dr. Zuleima T. Karpyn, who gave me invaluable guidance and support throughout my time at Penn State and made this work possible.

I also would like to thank Dr. Derek Elsworth for the honor of having him in my thesis committee and for the great discussions and insights about this work.

I am grateful to Dr. Parisa Shokouhi and Yingjun Guan for providing access to the CITEL Laboratory at Penn State and for all advice and help with my experimental setup.

Dr. Luis F. Ayala H. for his great encouragement and guidance during my Master's studies.

All my professors at the EME Department for their wonderful classes and contributions to my professional and personal growth.

All employees at the EME Department, especially Jaime Harter, for their unconditional support and advice.

The Science without Borders Program, therefore, the Brazilian People, and The Geological Survey of Brazil, its Chairman, Directors and all employees, for believing in my potential and giving me the opportunity and financial support that made this work a reality.

The Penn State Institutes of Energy and the Environment for the financial support necessary to realize my experiments.

My great friends at Penn State, especially Abraham, Renzo, Romulo, Ian, my "school and UFRGS time" friends for giving me friendship and strength indispensable to go further.

My girlfriend and friend, Gabriela, for all understanding and support throughout my studies at Penn State.

Finally, I would like to thank all my family for the inspiration, support and love that have pushed me forward. I will be forever grateful.

Chapter 1

Introduction

Motivation

Characterization and monitoring of underground reservoir properties, such as lithology, rock properties and saturating fluids, is of paramount importance for a multitude of disciplines. Among them, one can cite environmental and water resources engineering, mining engineering, hydrogeology, geology, petroleum and natural gas engineering. In general terms, these are important properties for any discipline that works with projects related to the underground environment. For example, in carbon capture and sequestration (CCS) projects, where CO_2 must be safely stored away from the atmosphere for thousands of years, it is imperative to be able to predict, monitor and verify the storage performance (Benson and Cook, 2005; Benson, 1980; Shaffer, 2010), which are tasks directly related to the understanding of how CO_2 affects the geological formation and behaves in such environment. Similarly, in petroleum and natural gas recovery projects there is a strong need to accurately forecast the performance of the hydrocarbon reservoir under various operational conditions, thus maximizing the economic recovery and minimizing and assessing the risk associated to the project, which can encompass a capital investment of hundreds of millions of dollars (Ertekin et al., 2001; Fanchi, 2006). Again, such forecast, generated by simulation engineers with the help of reservoir simulation tools, is strongly dependent on the quality of the input data used by the engineer on the heterogeneities and anisotropy of the rock and fluid properties throughout the reservoir (Ertekin et al., 2001; Fanchi, 2006). Moreover, the remediation of ground water resources, which accounts for approximately two-thirds of all freshwater available worldwide (Lehr, 2002; Nace, 1971), equally requires a good knowledge of the reservoir properties in order to enable the accurate prediction of the

contamination extension and transport, as well as the correct implementation of the recommended remediation technology (Bhandari et al., 2007; Lehr, 2002; Naftz and Davis, 1999). Analogously, groundwater production projects and usage of disposal wells also require the characterization and monitoring of reservoir properties (Bahadori and Zeidani, 2012; Deb, 2014; Pehme, 2009). In fact, this is the case for any underground fluid injection, extraction and/or remediation project. Therefore, understanding, predicting and monitoring underground reservoir properties is important for other applications as the study of glaciers and permafrost, analysis of underground biological process, assessment of environmental impacts and risks and so forth (Adler, 1992; Arcone, 2002; Bhandari et al., 2007; Lehr, 2002; Mavko et al., 2009; Shean and Marchant, 2010).

In this context, seismic surveys and well-logging are one of the most attractive approaches to gather information about reservoirs, since they provide reliable information with the needed spatial coverage and resolution required for many applications (Fallis, 2013; Gadallah and Fisher, 2013; King, 2009; Lei and Xue, 2009; Pehme, 2009). Seismic prospecting is a technique that provides one of the highest depth of penetration. Nevertheless, there are disadvantages in terms of acquisition cost, resolution and interpretation, since the relationships between seismic attributes, such as acoustic velocities, and rock properties (like porosity and pore saturation) are not unique (Mavko et al., 2009; Pehme, 2009). Moreover, the interpretation of seismic images has some degree of conceptual uncertainty as the background of the geoscientist can easily bias it (Bond et al., 2007). Therefore, seismic measurements should be combined with other available geophysical tools in order to appropriately establish rock properties throughout the geological formation (Mavko et al., 2009; Pehme, 2009). One example of an advantageous combination is the simultaneous usage and analysis of seismic and modern well logs that bring information about the vicinity of the borehole at much higher resolution, since seismic can reliably infer structural information acquired into the area distant from the wellbore (Dewan, 1983; Pehme, 2009). A good example of such logging technique would be the modern sonic logs,

which use acoustic waves at sonic frequencies (around 25 kHz) to produce information with good vertical resolution, which is related to the spacing between receivers (usually 2 feet), but small depth of penetration (Dewan, 1983). The higher the frequency (the shorter the wavelength) of the acoustic wave, the smaller is the depth of penetration and the higher is the resolution of the collected information (Dewan, 1983; Fallis, 2013; Mavko et al., 2009; Pehme, 2009). Both of these methods, seismic surveys and sonic logs, strongly rely on the usage of rock physics and elastic wave propagation in porous media in order to gather information on lithology, fluid types and saturations, pore pressure, fractures, confining stress and other rock properties (Dewan, 1983; Fallis, 2013; King, 2009).

Yet, the estimation of seismic parameters in partially saturated rocks can be a challenging assignment due to uncertainties associated to heterogeneities in fluid saturation, porosity, permeability and other rock and flow properties (Monsen and Johnstad, 2005). In the case of determining pore fluid types and saturations, acoustic wave velocities and attenuation are important parameters that need to be investigated (Fallis, 2013; Lebedev et al., 2009; Mavko and Nolen-Hoeksema, 1994; Mavko et al., 2009). Nevertheless, the lack of information about fluid saturation distribution within the rock generates a strong uncertainty on the prediction of these parameters, as different models developed for this purpose, such as the White-Dutta-Odé, Gassmann-Voigt-Reuss bounds, produce significantly different predictions, being the choice between them dependent on the information on saturation distribution, as they are sensitive to this parameter (Caspari et al., 2011; Lebedev et al., 2009; Mavko et al., 2009; Toms et al., 2007). Therefore, this work aims to better investigate experimentally and theoretically the impact of saturation distribution on wave velocity and performance of different patchy models.

Chapter 2

Literature Review

2.1 Basic Reservoir Properties

Most of the underground reservoirs found in nature are composed by sedimentary rocks, specially sandstones, which account for around 60% of all petroleum reservoirs (Fallis, 2013), for example. Sandstone formations are also present in many aquifers, such as the Guarani aquifer in South America (Pehme, 2009; Rodriguez et al., 2013; Takahashi and Mourão, 2012), and are usually high permeability and high porosity reservoir rocks. These rock properties and also the type and distribution of saturating fluids represent one of the most critical properties of a underground reservoir (Best, 1992; Fallis, 2013; Pehme, 2009). Permeability is an intrinsic rock property that represents its ability to transmit fluids within its connected pore spaces. Nevertheless, permeability relative to different fluids also depends on the level of saturation of the fluids, pore space characteristics, wettability and saturation history (Karpyn et al., 2010; Klinkenberg, 1941); Permeability is derived from the Darcy's law equation (Darcy, 1856), which follows below, and is usually expressed in terms of Darcy or millidarcy.

$$Q = \frac{A * k * \Delta P}{\mu * \Delta X}$$

Where:

Q = volumetric flow rate in the porous media [cm^3/sec];

A = area perpendicular to the flow direction [cm^2];

k = permeability of the medium [Darcy];

μ = dynamic viscosity of the fluid [centipoise];

ΔP = pressure difference [Atmosphere];

ΔX = length parallel to the flow direction [cm];

Porosity is another intrinsic rock property and represents the volume of void space, or pore space, in the rock in relation to the total volume of the rock. This property is related to permeability, nevertheless, their relationship is complex. Porosity is reported as a ratio and is given by the equation below.

$$Porosity = \frac{Volume_{pores}}{Volume_{total}}$$

Where:

$Porosity$ = ratio between pore space and total rock volume [ratio];

$Volume_{pores}$ = volume of the pore space (open space) within the rock, including fluids [cm^3];

$Volume_{total}$ = total or bulk volume of the rock, including the solid and pore space [cm^3].

As previously mentioned, pore fluid type and distribution is another important reservoir property that is also crucial at defining the viability of any project related to extraction of underground fluids. The main fluids naturally found in the underground environment are water, oil and gas (Fallis, 2013). Their distribution in the underground environment is usually not homogeneous, in fact, even the saturation distributions produced in relatively homogeneous and isotropic samples by controlled imbibition and drainage experiments at bench scale are commonly not uniform (Cadoret and Marion, 1995; Karpyn et al., 2010). As it can be seen in the Figure 1 (Karpyn et al., 2010), even at fairly homogeneous synthetic environments, there is a strong occurrence of heterogeneities in the distribution of fluids. Figure 1, part (a), presents the oil blob, or patches, volume map along the length of a glass bead pack sample at the end of a drainage cycle and also the vertical position and volume of randomly selected clusters presented in part (b). Figure 1, part (b), shows a three-dimensional visualization of the selected oil clusters and their relative size and positioning in the glass bead pack after the drainage cycle. Therefore, this is not a surprise that this kind of fluid distribution heterogeneity is also observed in natural underground reservoirs.

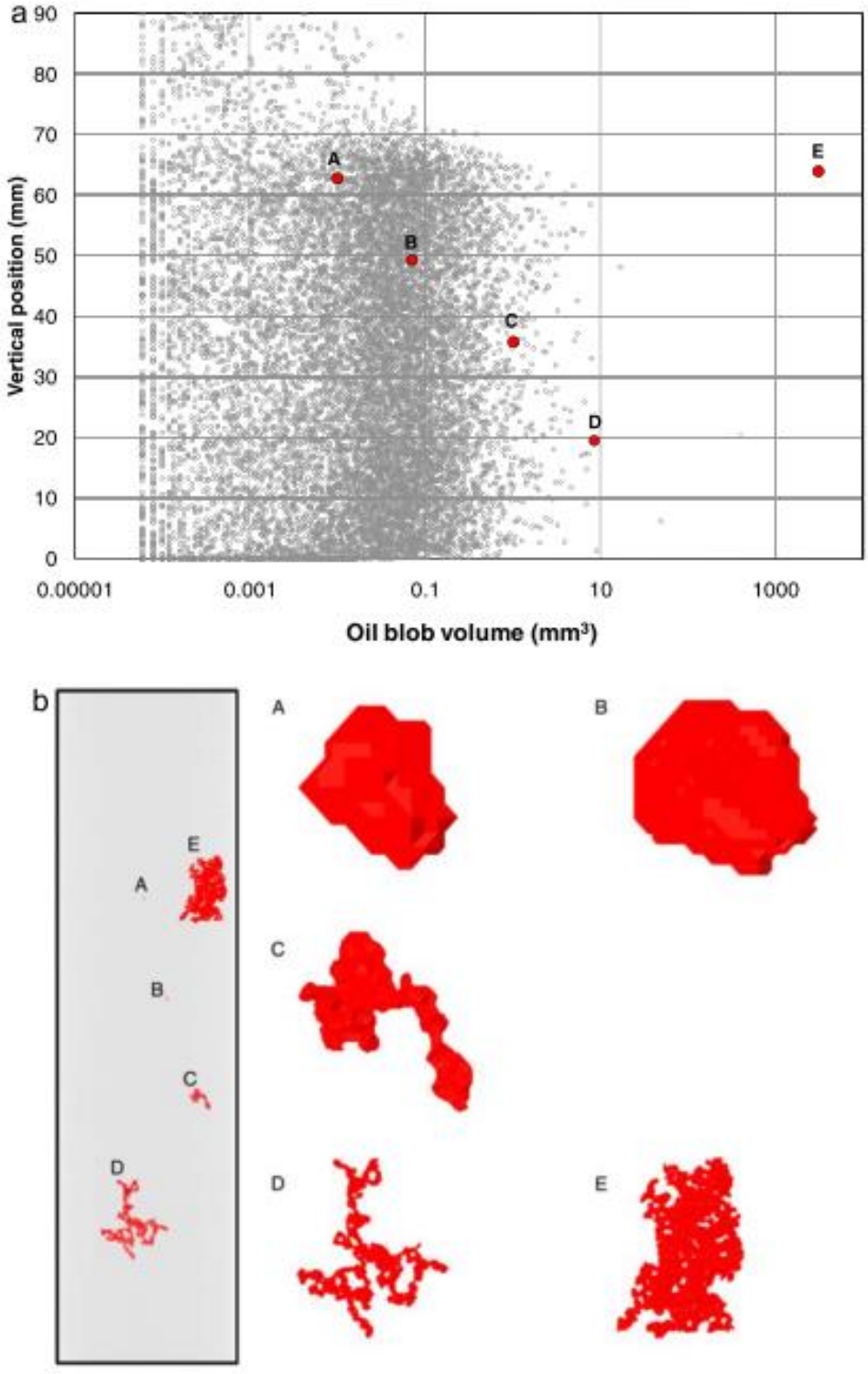

Figure 1. (a) Map of oil patch volumes along the length of a bead pack at the end of a drainage cycle, including the vertical location of randomly selected oil patches. (b) Three-dimensional visualization of individual oil patches and their relative location and dimension in the glass bead pack (Extracted from Karpyn et al., 2010).

2.2 Acoustic waves

Acoustic waves, or sound waves, are disturbances in a medium caused by pressure oscillations that travel in the same direction as the vibration they impose to the medium at a certain frequency (Rossing et al., 2012). This phenomenon founds application in the most variable fields, from music and medicine to geological/geophysical surveys (Cheeke, 2012; Mavko et al., 2009; Pehme, 2009; Rossing et al., 2012). One of the most classical ways to classify acoustic waves is using different frequency ranges, based especially on the frequencies that humans can hear (20 Hz to 20 kHz). For instance, acoustic waves above 20 kHz are classified as ultrasonic, whereas waves below that range are called infrasound (Rossing et al., 2012). Geophysical surveys using the propagation of acoustic waves through the earth are important because they can provide reliable information with the needed spatial coverage and resolution required for many applications (Fallis, 2013; Gadallah and Fisher, 2013; King, 2009; Lei and Xue, 2009; Pehme, 2009). Geophysical exploration surveys are produced by generating, recording and analyzing acoustic waves (also often called seismic waves) that travel through the subsurface of the Earth (Fallis, 2013; Pehme, 2009). Any given acoustic source usually generates four types of acoustic waves, which are the compressional (P-wave), shear (S-wave), Rayleigh and Love waves (Fallis, 2013). The last two, Rayleigh and Love, are surface waves and propagate parallel to the surface receiving the wave source, which can also be used for geophysical interpretation through, for example, spectral or multi-channel analysis, but receive reduced attention in geophysical exploration (Fallis, 2013; Pehme, 2009). On the other hand, P- and S-waves are defined as body waves as they travel outward in all directions from the source and trough the interior of the medium being investigated. P-waves, which are faster than S-waves, are longitudinal waves that vibrate the medium parallel to the direction of propagation of the wave. In

the case of S-waves, the medium vibrates transversely to the direction of propagation of the wave, which causes the wave to move slower. It is important to notice that usually shear waves are not transmitted through fluids since most of them present negligible shear strength. Figure 2 presents the direction of propagation of the P-, S-, Love and Rayleigh waves and also the particle motion orientation for them.

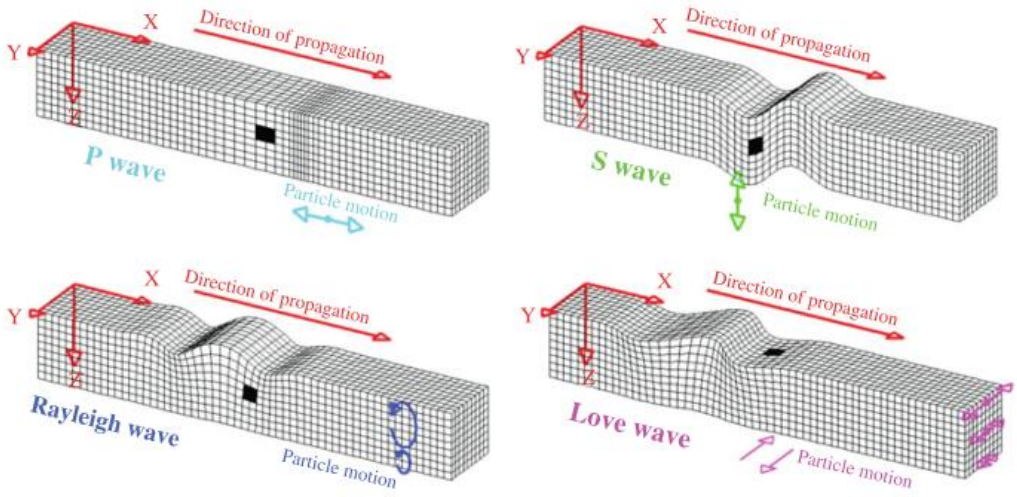

Figure 2. Direction of propagation and particle motion orientation for the P-, S-, Love and Rayleigh waves. Extracted from Fallis (2013).

The basic principle of a seismic survey or an acoustic well log is to initiate a wave pulse at or near the surface of the area to be analyzed and record the amplitudes and travel times of the waves, which then enable posterior analysis of different seismic parameters (Fallis, 2013). Acoustic wave velocity is one of the most important parameters for the interpretation of seismic data, as it is relatively easy to measure and many relationships between velocity and reservoir properties are available and reasonably well established (Best, 1992; Fallis, 2013; Mavko et al., 2009). For instance, the shear and compressional wave velocities in a homogeneous and isotropic

elastic media are given by the equations below, which shows that wave velocity is dependent on rigidity, bulk modulus, shear modulus and density of the medium. Rigidity (M) is a measurement of rock's resistance to both shearing and compression and is defined as (Dewan, 1983):

$$M = K + 4/3\,\mu$$

Compressional wave velocity (Vp) in an elastic solid is dependent on the rock's density (ρ) and rigidity (M). Conversely, shear wave velocity (Vs) depends only on shear modulus and density. Therefore, the expressions defining Vp and Vs boil down to (Dewan, 1983; Mavko et al., 2009):

Equation 1. P-wave velocity

$$Vp = \left(\frac{M}{\rho}\right)^{\frac{1}{2}} = \left(\frac{K + 4/3\mu}{\rho}\right)^{\frac{1}{2}}$$

Equation 2. S-wave velocity

$$Vs = \left(\frac{\mu}{\rho}\right)^{\frac{1}{2}}$$

$$\rho = [(1 - \emptyset) * \rho_m] + [\emptyset * \rho_f]$$

Where:

Vp = compressional wave velocity [m/sec]

Vs = shear wave velocity [m/sec]

M = Rigidity of the rock [Pa].

K = Bulk modulus of the rock [Pa].

μ = Shear modulus of the rock [Pa].

ρ = Density of the rock [kg/m^3].

$\emptyset$ = porosity of the rock [kg/m^3].

ρ_m = Density of the mineral rock frame [kg/m^3].

ρ_f = Density of the pore fluid [kg/m^3].

2.3 Relationships between reservoir properties and acoustic wave properties

In the following sections, empirical and theoretical relationships between some main reservoir properties and acoustic wave parameters are presented, especially in terms of wave velocity or slowness (inverse of velocity), since this is the main parameter of interest in this work. In terms of wave velocity and its behavior, it is possible to divide sedimentary rocks in two groups (Schön, 2015):

- Dense rocks with virtually no porosity and, therefore, no pore fluid, which consequently have their velocity controlled by the mineral composition, for example, such as Anhydrite and salt.
- Rocks with considerable porosity, which have a velocity range that depends on porosity, rock consolidation and cementation, mineral composition, pore shape, pore fluid type and distribution, pressure and temperature. Sandstone, dolomite, limestone would make part of this group.

In this work, the second group, composed by porous reservoir rocks, in the one of interest as their acoustic velocities are influenced by pore fluid properties and saturation.

2.3.1 The effect of rock porosity on velocity

From Equation 1 it can be observed that the stiffer, the more rigid a medium is, the higher the velocity is expected to be. Conversely, the higher the density of the medium, the lower the velocity. Moreover, as we can see from the variables of this expression, the velocity is affected only by the overall density and rigidity of the rock, as the wavelength is usually several times larger than the size of the pores and grains of the rock. For example, at a sonic frequency of 25 kHz, the wavelengths are 4 to 12 inches (10 to 30 cm) in the formations of interest (Dewan, 1983), hence, the wave does not sense small features of the rock but overall parameters. Consequently, changes in porosity would affect velocity through its impact on these overall parameters. From the Vp equation we see that if an increment in porosity decreases the rigidity of the rock faster than its density, there is a reduction in wave velocity, which in fact is usually the case (Dewan, 1983). There are theoretical expressions that correlate compressional velocity and porosity of a medium, nevertheless, they are not really usable in normal well-log analysis as they require information about elastic properties of pore fluid, grain material and empty rock frame (Dewan, 1983; Hartley, 1981), which are unknowns in most cases. Therefore, there is a strong use of empirical relationships to describe porosity from velocity, or vice-versa. In this case, the most popular empirical expressions would be the Wyllie Relation and the Simpler Travel Time-Porosity Conversion (Dewan, 1983). There are several other empirical relations that can be used for this purpose, such as Nur's modified Voigt average, Geertsma's relations, Han's relations, Tosaya's relations and Castagna's relations (Mavko et al., 2009). The Wyllie Relation (Dewan,

1983; Wyllie et al., 1958) is given by the equation below and requires information about the wave travel time in the fluid of the zone of investigation, which is usually mud filtrate, travel time of the solid rock matrix and measured travel time of the rock.

$$\emptyset = \frac{(t - t_{ma})}{(t_f - t_{ma})}$$

Where:

t = measured travel time of the porous rock [μsec/feet];

t_f = travel time of the pore fluid in the zone of investigation [μsec/feet], usually 189 μsec/feet if fresh mud;

t_{ma} = travel time of the solid rock matrix [μsec/feet], taken as 55.5-51.3 μsec/feet for sandstones, 47.6-43.5 μsec/feet for limestones, 43.5-38.5 μsec/feet for dolomites;

$\emptyset$ = estimated porosity for the investigated formation [ratio].

In the case of the Simpler Travel Time-Porosity Conversion (Dewan, 1983; Raymer et al., 1980) we only need information about the travel time of the solid rock matrix and measured travel time of the rock. Here, porosity is described as:

$$\emptyset = 0.63 * (1 - \frac{t_{ma}}{t})$$

As we can see, even empirical relations require precise information about the lithology, especially dry rock frame, in order to produce appropriate estimations, as there is a significant discrepancy between the travel time of different rock matrices.

2.3.2 The effect of rock mineral composition on velocity

The mineral composition of the rock impacts directly the velocity of both shear and compressional waves since different minerals have different bulk moduli, shear modulus and density. Therefore, the overall mineral composition of the rock can significantly affect the moduli and density of the rock. The stiffer and lighter the minerals presented in the rock, the faster the waves will propagate in this porous medium. The average mineral moduli and density are calculated through a volumetric average of these properties for the different minerals composing the rock frame, being calculated as follows in the equations below. Table 1 presents a compilation of moduli, densities and velocities of for different common minerals, in order to give an idea of the range of variation that can be found these mineral properties.

Table 1. Moduli, density and velocities of common minerals. Adapted from Mavko et al. (2009).

Mineral	Bulk Modulus (GPa)	Shear Modulus (Gpa)	Density (g/cm3)	Vp (km/s)	Vs (km/s)	Poisson ratio
Olivines						
Forsterite	129.8	84.4	3.32	8.54	5.04	0.23
"Olivine"	130	80	3.32	8.45	4.91	0.24
Garnets						
Almandine	176.3	95.2	4.18	8.51	4.77	0.27
Zircon	19.8	19.7	4.56	3.18	2.08	0.13
Epidotes						
Epidote	106.5	61.1	3.4	7.43	4.24	0.26
Dravite	102.1	78.7	3.05	8.24	5.08	0.19
Pyroxenes						
Diopside	111.2	63.7	3.31	7.7	4.39	0.26
Augite	94.1	57	3.26	7.22	4.18	0.25
	13.5	24.1	3.26	3.74	2.72	0.06
Sheet Silicates						
Muscovite	61.5	41.1	2.79	6.46	3.84	0.23
	42.9	22.2	2.79	5.1	2.82	0.28
	52	30.9	2.79	5.78	3.33	0.25
Phlogopite	58.5	40.1	2.8	6.33	3.79	0.22
	40.4	13.4	2.8	4.56	2.19	0.35
Biotite	59.7	42.3	3.05	6.17	3.73	0.21
	41.1	12.4	3.05	4.35	2.02	0.36
Clays						
Kaolinite	1.5	1.4	1.58	1.44	0.93	0.14
"Gulf clays" (Han)	25	9	2.55	3.81	1.88	0.34
Framework silicates						
Perthite	46.7	23.63	2.54	5.55	3.05	0.28
Plagioclase feldspar (Albite)	75.6	25.6	2.63	6.46	3.12	0.35
"Average" feldspar	37.5	15	2.62	4.68	2.39	0.32
Quartz	37	44	2.65	6.05	4.09	0.08
	36.6	45	2.65	6.04	4.12	0.06
	36.5	45.6	2.65	6.06	4.15	0.06
	37.9	44.3	2.65	6.05	4.09	0.08
Quartz with clay (Han)	39	33	2.65	5.59	3.52	0.17
Carbonates						
Calcite	76.8	32	2.71	6.64	3.44	0.32
	63.7	31.7	2.7	6.26	3.42	0.29
	70.2	29	2.71	6.34	3.27	0.32
	74.8	30.6	2.71	6.53	3.36	0.32
	68.3	28.4	2.71	6.26	3.24	0.32
Dolomite	94.9	45	2.87	7.34	3.96	0.3
	69.4	51.6	2.88	6.93	4.23	0.2
	76.4	49.7	2.87	7.05	4.16	0.23

$$K = \sum_{i}^{n} Km_{\,i} * fraction_{\,i}$$

$$G = \sum_{i}^{n} Gm_{\,i} * fraction_{\,i}$$

$$\rho = \sum_{i}^{n} \rho_{M\,i} * fraction_{\,i}$$

Where:

K = Bulk modulus of the rock [GPa]

$Km_{\,i}$= Bulk modulus of the mineral "i" [GPa].

G = Shear modulus of the rock [GPa]

$Gm_{\,i}$= Shear modulus of the mineral "i" [GPa].

ρ = overall mineral bulk density of the rock [kg/m^3].

$\rho_{M\,i}$= bulk density of the mineral "i" [kg/m^3].

$fraction_{\,i}$ = volumetric fraction of the mineral "i" in the overall mineral composition of the rock [%].

In the case of clastic rocks, such as sandstones, the presence of clay can represent a significant extra decrease in shear and compressional velocity, as indicated in a study done by Han et al. (1986) in 75 sandstone samples fully water saturated and at 40 MPa of confining

pressure and 1.0 MPa of pore pressure. The results of this study were compiled and presented by Schön (2015) in Figure 3.

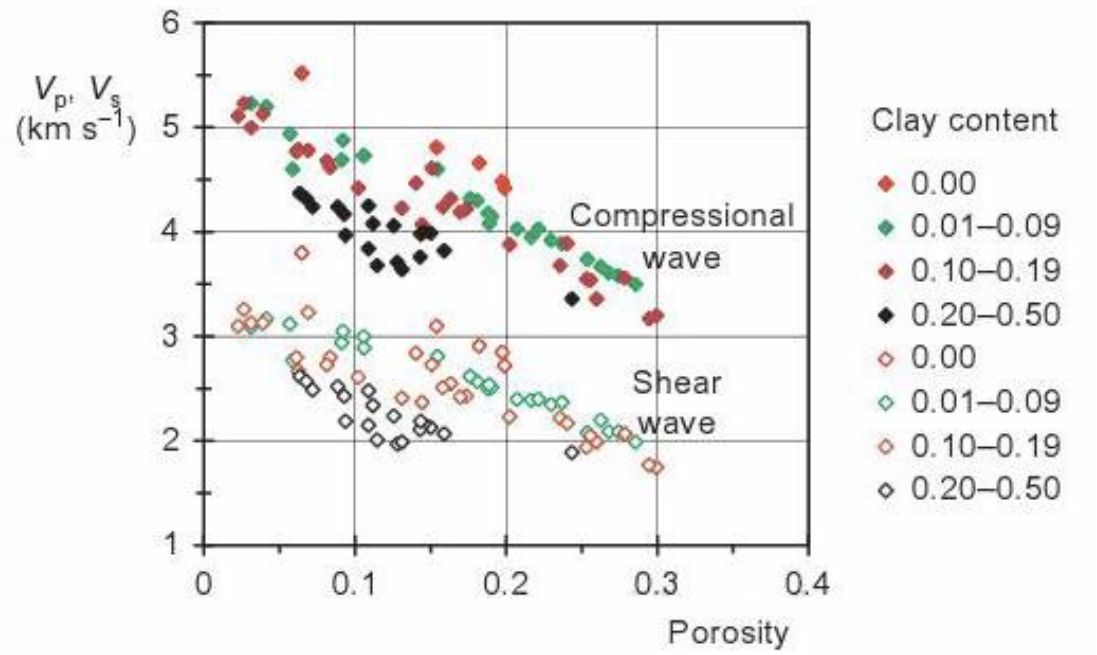

Figure 3. Vp and Vs for 75 sandstone samples at fully water saturated condition. Samples were at 40 MPa confining pressure and 1.0 MPa pore pressure. Extracted from Schön, 2015a and after Han et al. (1986).

2.3.2 The effect of pore fluid type and distribution on velocity

Different pore fluids, commonly water, gas, oil and their mixtures, affect compressional and shear waves as a result of their influence on different effective rock properties, which would be the following (Cadoret and Marion, 1995; King, 2009, 1966; Mavko et al., 2009; Müller et al., 2010; Schön, 2015; Winkler and Murphy III, 1995):

- elastic properties (bulk and shear moduli) and density of the pores and consequently of the rock as a whole;
- change in particle-contact, for example, by swelling of cementing material;
- stress components from interfacial tension and capillary forces in the case of partial saturation situations, manifested by mechanism such as wave induced fluid flow (WIFF).

As mentioned, pore fluids influence the effective properties of the rock through changes in bulk and shear moduli and density of the pores, therefore, it is expected that different pore fluids, which have different moduli and densities, produce different impacts on effective rock properties. Figure 4 is a good representation of this phenomenon and shows the effect produced by three different fluids fully saturating a sandstone, thus, not in a partial saturation condition, subjected to different effective pressures. From Figure 4 it is possible to notice that effective pressure produces a positive effect on velocity, in order words, the higher the effective pressure the higher the velocities, both compressional and shear. Moreover, compressional wave velocity increases from air to kerosene to water and, therefore, represents the tendency of increasing bulk moduli and Vp of these saturating pore fluids.

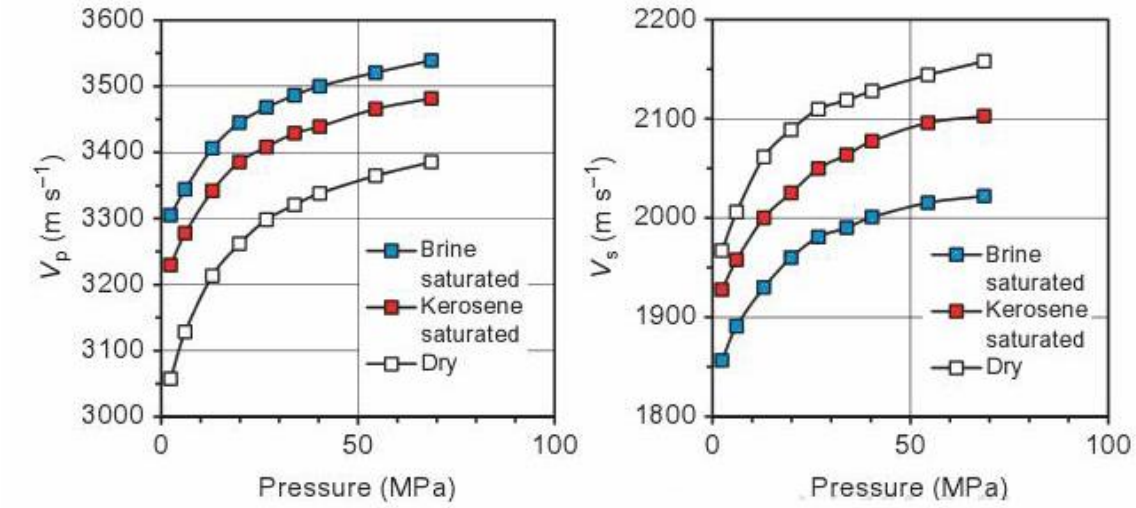

Figure 4. Compressional and shear wave velocity behavior of Boise sandstone samples fully saturated with different pore fluids at different effective pressure levels. Extracted from Schön (2015) *and after* King (1966).

Furthermore, Figure 4 shows that shear wave velocity has a trend opposite to Vp's, where Vs increases from water to kerosene to air, as these fluids do not impose resistance to shear movement and, therefore, do not contribute to the effective shear modulus of the rock. In this case, only the change in density of the fluids affects the performance of Vs, which explains the trend, as density increases from air to kerosene to water. Important to notice that the assumption of fluids having no resistance to shear stress is not applicable for high viscosity fluids such as heavy oil (Schön, 2015; Wang and Nur, 1988).

Moreover, it assumes no interaction between pore fluid and properties of the mineral matrix, which is not necessarily true as King (1966) reported that for Bandera sandstone the compressional wave velocity was faster for kerosene than for water, indicating a softening of the matrix by some clay-water interaction, in that case, swelling. Cadoret et al. (1993) also reported interaction between rock frame and fluids, as he observed a velocity reduction between an extremely dry limestone and a limestone briefly exposed to environment moisture. In fact, the Ve (extensional velocity) was approximately 4% lower for the moisture-wet sample, as shown in

Figure 5. Again, it is caused by some softening of the mineral matrix, which is here attributed to occur due to the introduction of monolayers of water on the internal surface of the rock, thus lowering the surface energy of the grains and thereby decreasing the cohesion and stiffness of the grain contacts (Murphy III et al., 1984; Tutuncu and Sharma, 1992; Winkler and Murphy III, 1995). It is important to notice that in this work the term “dry rock” or “dry condition” will be used to refer to a rock that has some moisture absorbed and, thus, is not extremely dry, so this abrupt reduction in velocity is not observed.

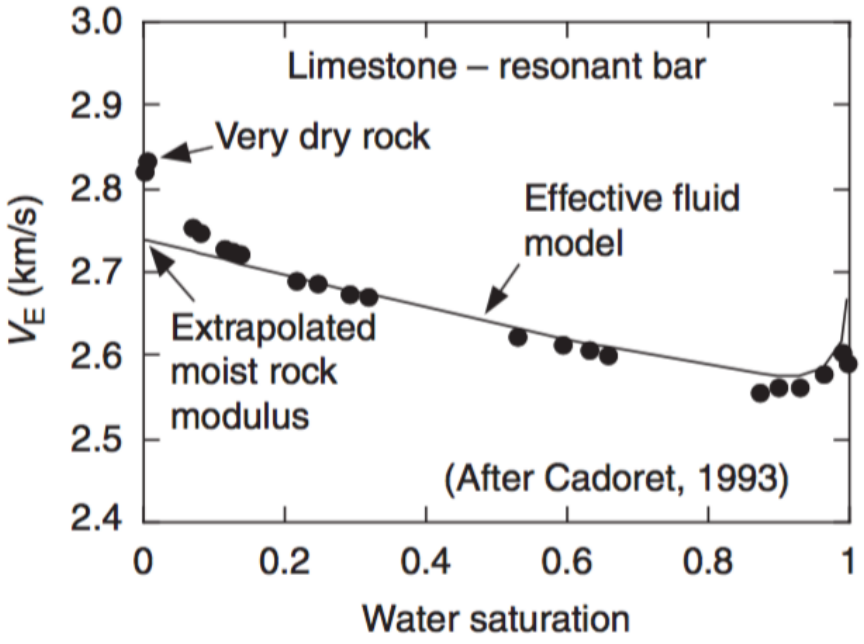

Figure 5. Extensional velocity drop caused by moisture absorption in a Limestone, as observed by Cadoret et al. (1993). *Extracted from* Mavko et al. (2009).

Figure 6 presents the sensitivity of acoustical properties to moisture absorption for different sandstones and carbonates, where normalized shear velocity at ultrasonic frequency decreases with increasing exposure to water moisture. Additionally, Figure 6 shows increasing

shear wave attenuation and decreasing velocity for increasing moisture exposure (Clark et al., 1980; Mavko et al., 2009; Winkler and Murphy III, 1995).

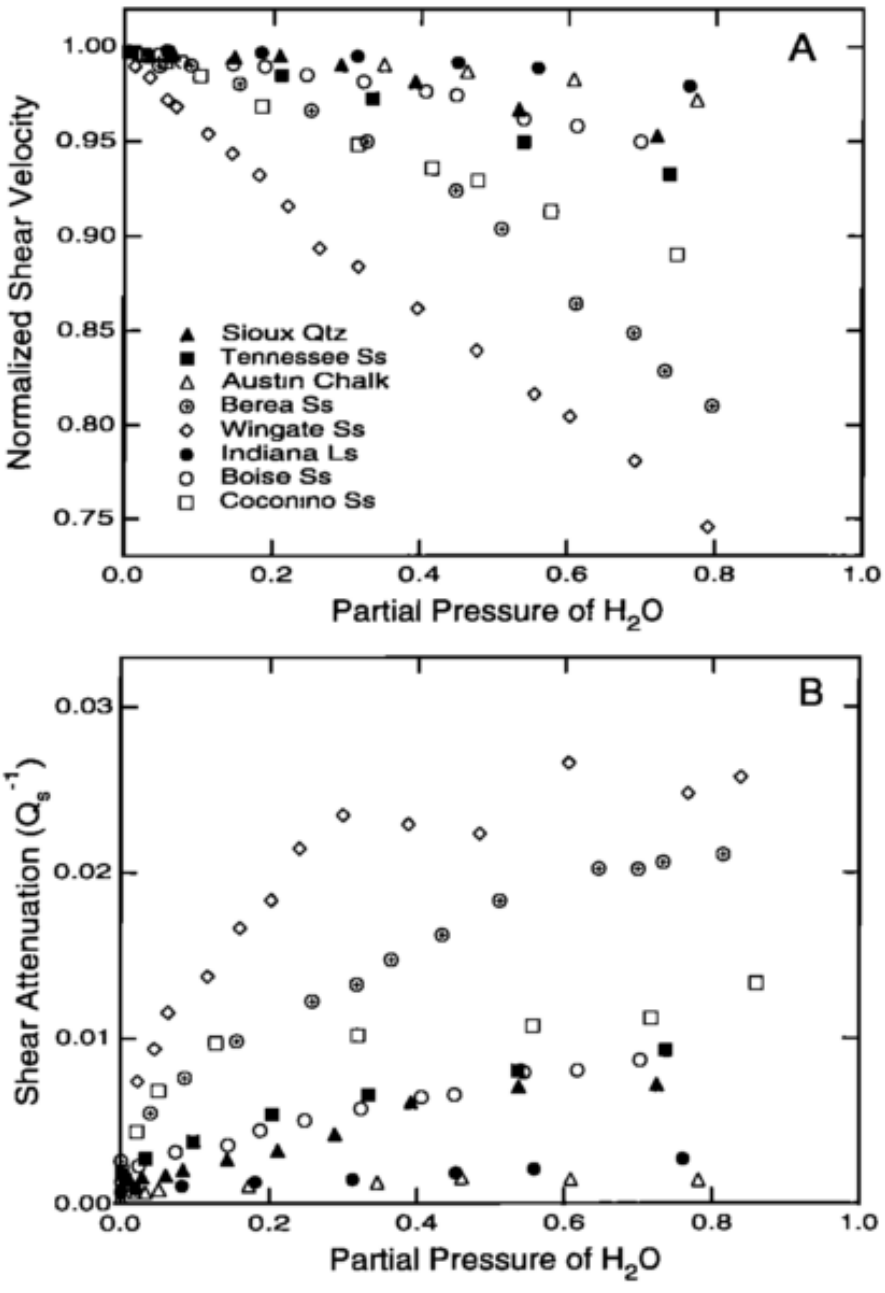

Figure 6. Normalized shear wave velocity and shear attenuation versus partial pressure of water vapor for different rocks after Clark et al. (1980) . *Extracted from* Winkler and Murphy III (1995).

In Figure 7, after Røgen et al. (2005), we have shear and compressional wave velocities versus porosity for a fracture-free carbonate rock from the North Sea region at both dry and fully water saturated conditions. As seen in Figure 7, there is a general trend of decreasing velocities for increasing porosities, phenomena that was already discussed in the Section 2.3.1. However, an extra trend can be observed here, which is the difference in velocities between the dry and fully water saturated rocks, especially at high porosity values. Vp is higher for water saturated samples as there is larger increases in the rock effective bulk moduli than in rock density. On the other hand, Vs is smaller for fully water saturated rocks, which is again most noticeable at higher porosities (Røgen et al., 2005; Schön, 2015). Again, this decrement in Vs for water-wet rock happens because water has negligible resistance to shearing and, therefore, only the increment in bulk density affects Vs, producing the lower S-wave velocities for fully water saturated rocks. The most pronounced differences in velocities are expected at higher porosity values, since larger pore volumes represent larger fluid volumes inside the rock and, therefore, represent larger impact on the effective properties of the rock.

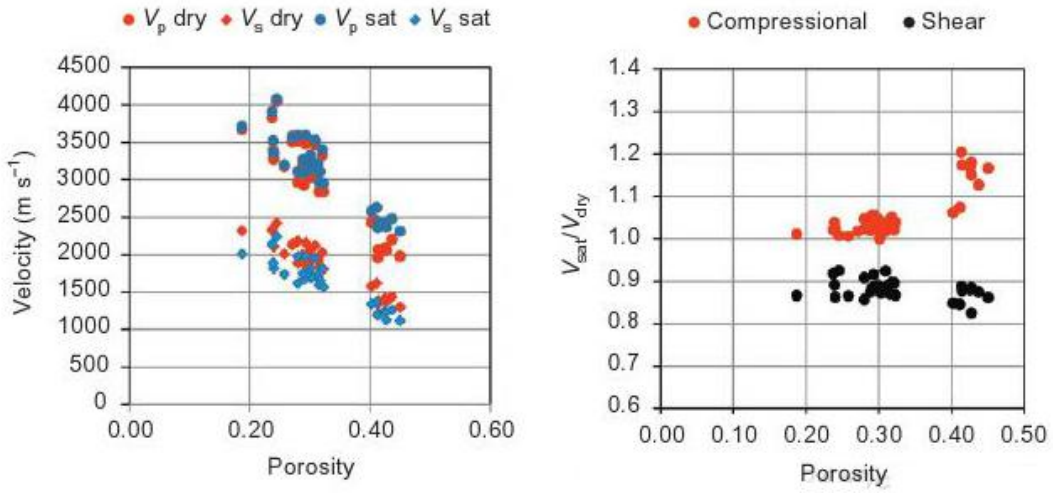

Figure 7. Pore fluid and porosity influence on shear and compressional velocities for unfractured chalk samples. Figure to the ***left*** *presents velocity for dry and fully water-wet rocks with different porosities. Figure to the* ***right*** *shows the ratio between wet and dry rock conditions for S- and P-wave velocity.Extracted from* Schön (2015) *and after* Røgen et al. (2005).

In addition to the effects in acoustic wave velocities produced by changes in porosity, mineral composition, mineral/fluid interactions and stiffness of the different fluids occupying the pore space, there is the effect caused by the frequency of the acoustic wave itself (Cadoret and Marion, 1995; Winkler and Murphy III, 1995). Moreover, in the case of partial saturation conditions, it is important to account for the effect in compressional velocity generated by the distribution of different fluid phases within the porous medium, which can be caused by capillary forces, interfacial tensions, rock permeability, pore size distribution, saturation history and differences in viscosities and bulk moduli (Biot, 1956a; Cadoret and Marion, 1995; Cadoret et al., 1993; Domenico, 1976; Knight and Nolen-hoeksema, 1990; Le Ravalec et al., 1996; Mavko et al., 2009; Schön, 2015; Winkler and Murphy III, 1995). For instance, depending on these parameters, different partial saturation configurations can be produced and consequently result in different behaviors for Vp, as it would dictate the distribution of stresses caused by fluctuations in pore pressure. For Vs, the presence of multiple fluid phases in the porous medium does not consist in a major concern, as fluids are considered to be free of shear resistance. In this context, the concept of Critical Length (Lc) is important to define the behavior of Vp versus saturation for partial saturation situations, which is given by the expression below (Mavko et al., 2009):

$$Lc = \sqrt{\frac{k * K_{fl}}{\eta * f}}$$

Where:

Lc = critical length [meter]

k = Rock permeability [meter ^{2}]

K_{fl}= Bulk modulus of the fluid [Pa].

η = Fluid viscosity [Pa.second]

f = acoustic wave frequency [Hertz]

Critical Length is a crucial parameter, as it represents the maximum scale of saturation heterogeneities that would not generate fluctuations in pore pressure when an acoustic wave travels through the medium. Thus, saturation heterogeneities smaller then Lc would have enough time to dissipate and equilibrate through fluid flow and reach a local isostress condition (Mavko et al., 2009). In this case, the distribution of fluids in the medium would be considered as **uniform** distribution or uniform saturation. Conversely, saturation heterogeneities in a scale larger than Lc would tend to endure and produce lasting pore pressure fluctuations, which ultimately would result in fluid patches of different stiffness within the porous medium. Therefore, each pixel or "patch" at scale equal to or smaller than Lc would have the fluid phases equilibrated within the patch. On the other hand, adjacent patches larger than Lc would not be in equilibrium with each other and would present different effective moduli (Mavko et al., 2009). For this last case, we would have what is defined as a **patchy** fluid distribution or patchy saturation. Figure 8 illustrates the relationship between the scales of Lc and fluid patches, in this case for two fluids represented by the blue and yellow colors. In this figure we consider that Lc is fixed and only the size of the patches varies, consequently, it is possible to notice that depending upon the patch size we can have either a patchy or a uniform saturation for the same saturation level.

Nonetheless, it is important to notice that Lc is inversely proportional to the frequency of the acoustic wave and viscosity of the fluid and proportional to the rock permeability and fluid bulk moduli. Therefore, if we consider that during an acoustic survey the permeability of the rock, the viscosity and bulk moduli of the fluids remain relatively constant, we would have that the higher the wave frequency the smaller the critical length, meaning that smaller heterogeneities in fluid distribution would be sufficient to produce a patchy behavior for Vp. On the other hand, the opposite would be true, thus, the lower the wave frequency the larger the Lc, demanding larger patch sizes in order to achieve a patchy trend for compressional velocity.

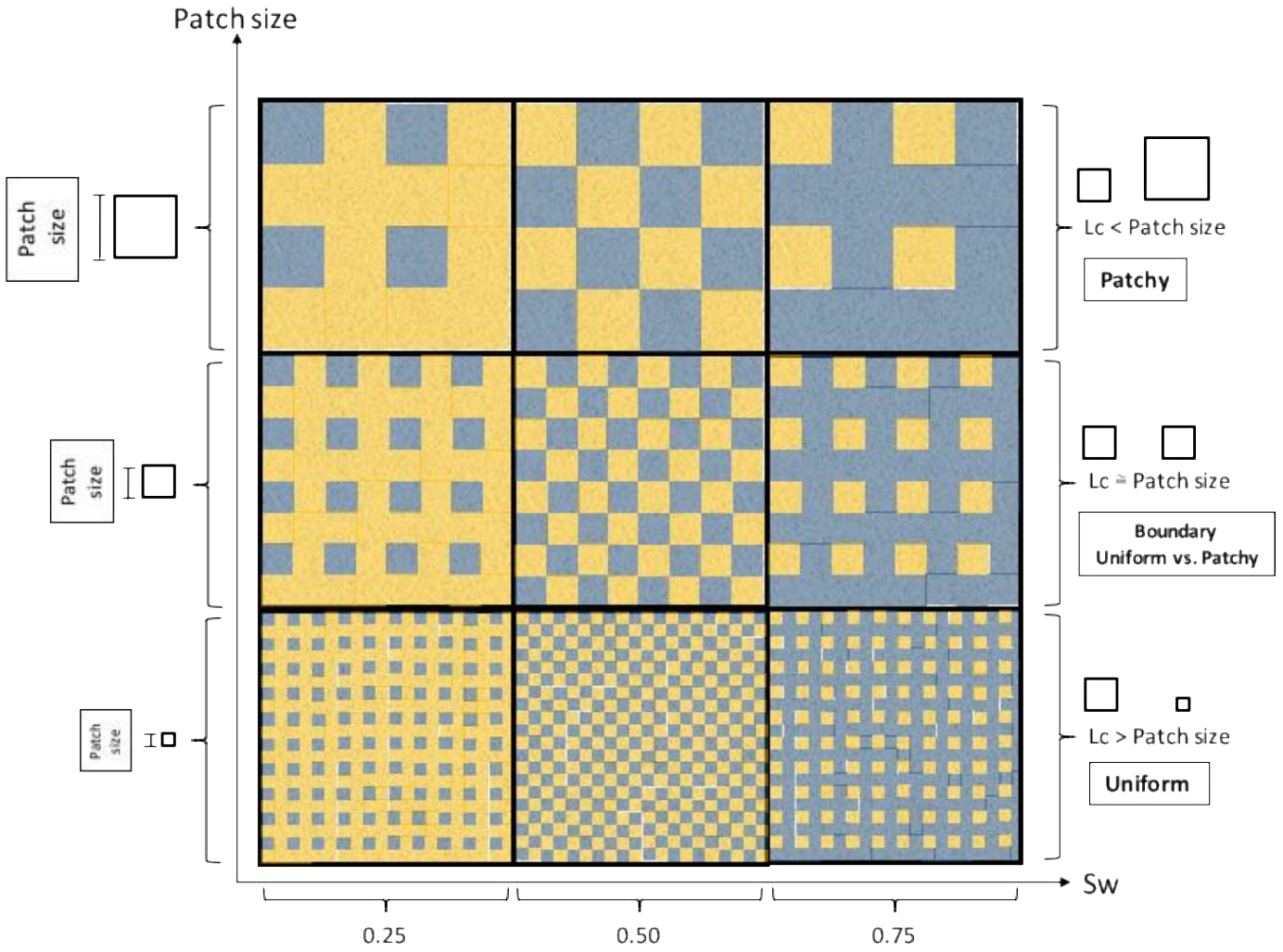

Figure 8. Difference from patchy to uniform saturation. Patchy saturation has the patch size larger than the Critical Length (Lc). For uniform saturation, Lc is larger than the patch size. In this figure it is considered that each patch does not communicate with each other.

Consequently, wave frequency is a key parameter for predicting Vp behavior in relation to saturation. In fact, it is common to refer to uniform saturation as the low-frequency bound and patchy saturation as the high-frequency bound. In the low wave frequency scenario, wavelength tends to be much bigger than the size of the heterogeneities, thus the rock appears to the wave as a homogeneous environment and Vp will be affected by an average of the moduli and densities of the rock components. For high-frequency case, the wavelength is small enough to sense small heterogeneities in the rock and, therefore, Vp will be more affected by the individual components of the rock. (Cadoret and Marion, 1995; Mavko et al., 2009; Winkler and Murphy III, 1995).

As mentioned previously, patchy and uniform saturation result in different behaviors for Vp in relation to saturation, but after all, what is the main difference between them? It depends on how these trends are modeled. For instance, in the case of a uniform saturation of gas and liquid, Vp is expected to steadily decrease as water saturation increases until reaching a certain point (around Sw = 80%) where Vp jumps to higher values until its maximum at 100% water saturation. On the other hand, for the same air / water system, a patchy fluid distribution is anticipated to steadily increase Vp as Sw goes from 0% to 100%. Figure 9 below presents these different trends for Vp, or different **bounds**, for the **patchy** and **uniform** saturation based on Gassmann's equations (Gassmann, 1951) using the fluid mixing models elaborated by Reuss and Voigt (Mavko et al., 2009; Reuss, 1929; Voigt, 1910). In Figure 9 we see that the uniform bound fits well the experimental data from Cadoret et al. (1993), as the wave frequency applied there was low (1 kHz). Anyways, at high water saturation levels we notice a deviation from the uniform bound, indicating the incidence of some "patchy" behavior (Mavko et al., 2009). The calculation of these patchy and uniform saturation bounds and other Vp versus Sw models will be presented in the next chapter.

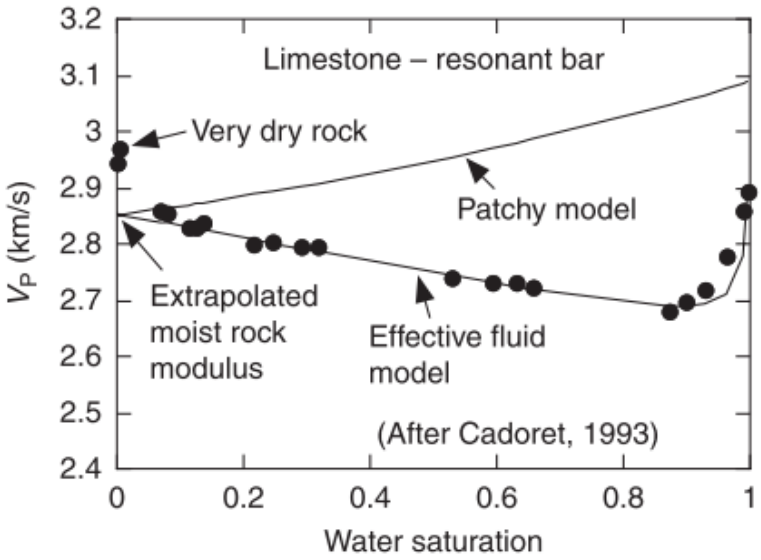

Figure 9. Vp versus water saturation for a limestone tested with a resonant bar and wave frequency of 1 kHz. Experimental data after Cadoret et al. (1993) *and upper and lower bounds after* Mavko et al. (2009). *Figure extracted from* Mavko et al. (2009).

One of the main reasons for having higher compressional velocities at patchy fluid distributions is the fact that pore fluid heterogeneities can produce stiffer regions inside the rock and, therefore, cause a deformation in the acoustic wave that creates a fast path effect, as shown in Figure 10. This phenomena was firstly discussed by (Mukerji et al., 1995) and is often referred to as the "fast path effect", which is more noticeable in the cases where Vp is calculated by using the length of the sample and the wave first peak arrival time (Cadoret and Marion, 1995).

On top of the "fast path effect", there are other intrinsic mechanisms that might be superimposed on it. For instance, Biot created a theory for propagation of wave in fluid saturated porous media that is centered in a macroscopic fluid-flow, in other words, fluid flow induced over the entire porous media. This model is usually called "global flow model" and takes into consideration the relative motion between fluids and the solid rock frame induced by acoustic waves due to inertial and viscous effects (Biot, 1956a, 1956b; Cadoret and Marion, 1995; Winkler and Murphy III, 1995). Hence, as the solid rock frame accelerates, fluid lags behind,

which would result in viscous dissipation of acoustic energy. For waves at low frequency, the size of the viscous skin is larger than the pore size and, thus, solid and fluid move in phase. Here, Vp is at a minimum, attenuation is reduced and Biot theory generates the same results as the Gassmann's equations using Reuss's average (Biot, 1956a; Cadoret and Marion, 1995; Winkler and Murphy III, 1995). At high frequencies, we have the opposite behavior, as viscous skin size is very small, inertial forces are predominant and differential movement between fluid and rock frame takes place. Now, Vp is at maximum and attenuation remains low (Biot, 1956b; Winkler and Murphy III, 1995). Therefore, Biot incorporate the viscous and inertial interactions between fluid and solid and predicts increasing Vp for increasing frequency (Biot, 1962, 1956a, 1956b; Cadoret and Marion, 1995).

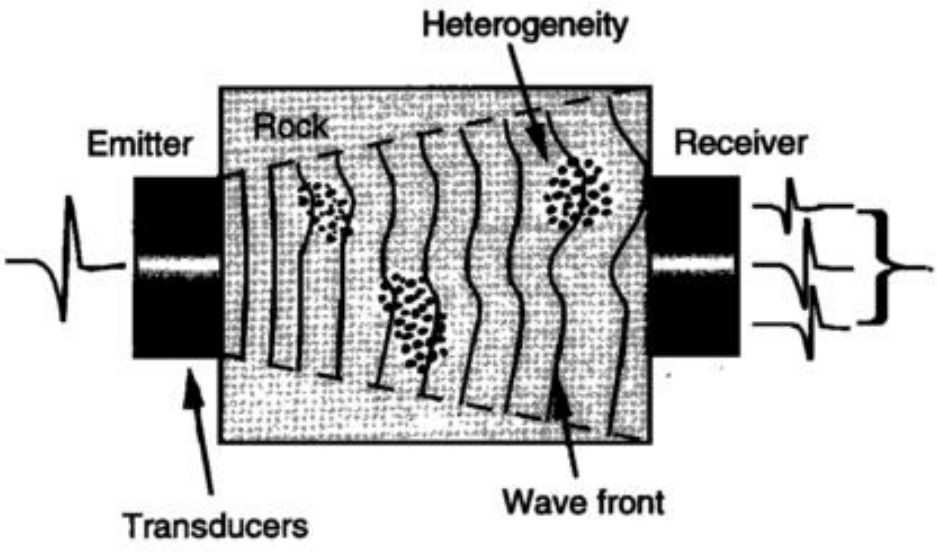

Figure 10. Representation of the fast path effect caused by heterogeneities of higher elastic modulus, which can cause deformations and acceleration of the wave front. Extracted from Cadoret and Marion (1995).

Another set of models, normally regarded as "local flow models" or "squirt models", consider variability in the rock stiffness at the pore scale, which causes microscopic fluid flow

within the rock. Therefore, a passing acoustic wave would generate local flow, which intensity depends on frequency and also on the size of pore throats (Cadoret and Marion, 1995; Mavko and Jizba, 1991). Thus, fluids could be moved between pores or micro-fractures by the passage of an acoustic wave, ultimately resulting in viscous losses and velocity dispersion (Biot, 1962; Cadoret and Marion, 1995; Mavko and Jizba, 1991; Mavko and Nolen-Hoeksema, 1994; Winkler and Murphy III, 1995).

Nevertheless, it has been shown that local flow mechanisms alone could not appropriately describe dissipation and attenuation measured at seismic frequencies (Carcione and Picotti, 2006; Diallo et al., 2003; Morgan et al., 2012; Müller et al., 2010; Pride et al., 2004). Pride et al. (Pride et al., 2004) demonstrated that measurements of attenuation and velocity could be explained by mesoscopic-scale heterogeneities, which are considered to be much larger than the grain size but smaller than the wavelength. Lithological variations or patches of different immiscible fluids could cause these mesoscopic variations, Here, the passage of an acoustic wave would have an effect similar to squirt, but this time the fluid flow would take place between these stiffer and compliant mesoscopic zones, which would have lower and higher pore fluid pressure, respectively (Pride et al., 2004). Figure 11, from Muller at al. (2010), illustrates the heterogeneity scale that is relevant for wave induce fluid flow (WIFF).

Considering the differences presented for the uniform and patchy saturation in terms of Vp versus fluid saturation, it is important to have in mind which frequency is being applied in an acoustic survey or laboratory experiment. Low frequency experiments, which wavelengths are much larger than the fluctuations in stiffness within the rock, using water imbibition process, tend to reproduce the Vp behavior predicted by the lower bound of the Gassmann's equation (uniform case using Reuss average). As it can be seen in Figure 12, this is exactly the case, as we see a good fit between the experimental data acquired by Murphy (Murphy, 1983) at 700 Hz in a

homogeneous and highly porous sandstone, submitted to a water imbibition cycle, and the prediction done using Gassmann's lower.

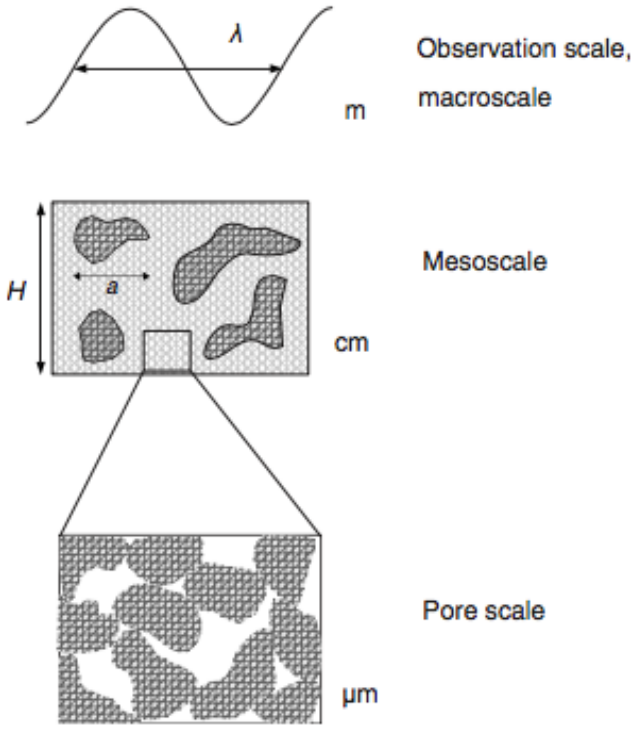

Figure 11. Different scale of heterogeneities that are of relevance for wave-induced flow to occur. Extracted from Müller et al. (2010).

Furthermore, as it is shown in Figure 13, it is possible to have differences in the behavior of Vp depending on whether the saturation was achieved through an imbibition or drainage cycle. For instance, as described in studies such as the ones done by Cadoret and Marion (1995); Cadoret et al (1998); Knight and Nolen-hoeksema (1990); Monsen and Johnstad (2005); Toms-Stewart et al. (2009), imbibition tends to produce a homogeneous fluid distribution, hence having the presence of gas inside virtually in all pores, condition that changes only at high water saturation levels. Therefore, until the achievement of high Sw, the increment in pore stiffness is

not enough to compensate for increase in pore density, culminating in the decrease of Vp. At high water saturations, pores start to get completely water filled and a jump in P-wave velocity is then observed. Consequently, until high water saturations are reached there are no heterogeneities larger than the critical length and Vp is well described by the Gassmann-Reuss low frequency bound. On the other hand, during the drainage process we have the pores being completely filled by water or air, as during the drainage cycle the pores have their water completely drained as they are accessed (Knight and Nolen-hoeksema, 1990). Therefore, measurements of acoustic velocity in drainage cycles, especially at high wave frequency, tend to follow a "patchy" behavior and produce higher velocities in comparison to the imbibition cycle. Figure 13 presents a Vp versus Sw plot that evidences this difference between the drainage and imbibition cycles, especially when water saturations are higher than 40%.

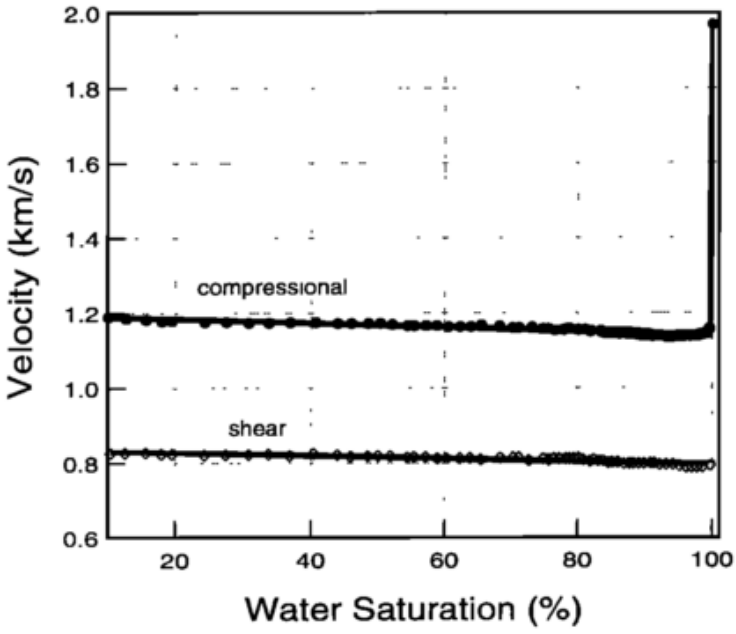

Figure 12. Compressional and shear velocity data for a Massilon sandstone (23% porosity and k=737 mD) as function of water saturation at wave frequency of 700 Hz and lower-bound predicted by Gassmann's equations. Extracted from Winkler and Murphy III (1995) *and after* Murphy (1983).

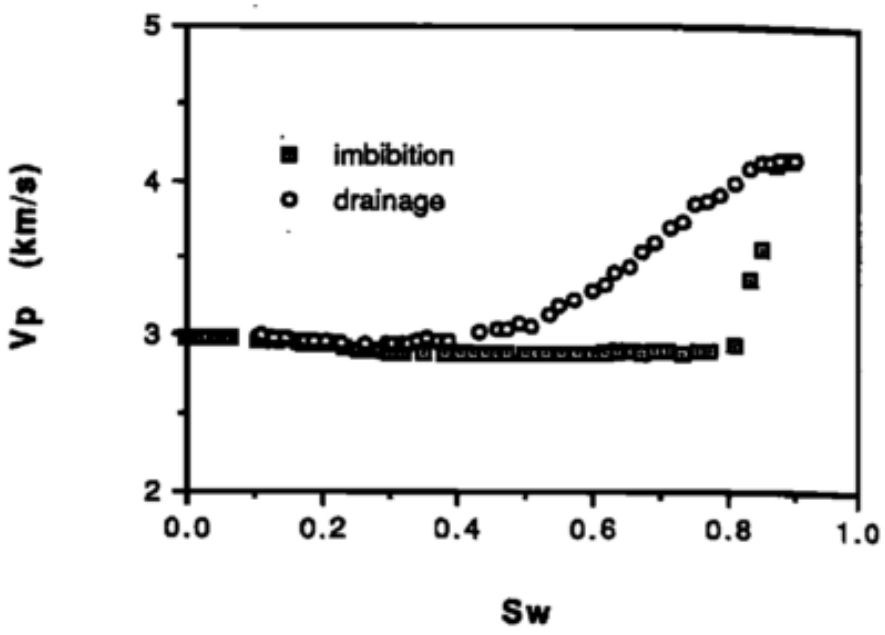

Figure 13. Compressional velocity versus water saturation during continuous imbibition/drainage experiment of a tight gas sandstone (5% porosity and k=0.001 mD) tested at 1 MHz. Produced by and extracted from Knight and Nolen-hoeksema (1990).

Moreover, higher frequencies result in the enlargement of the interval of saturation that presents the difference in Vp between drainage and imbibition, as higher frequencies incur in smaller critical lengths and therefore smaller saturation heterogeneities are sufficient to create a migration from "uniform" to "patchy" behavior. In Figure 14 this behavior can be noticed. Therefore, if for a test the ultrasonic frequency is held constant, for both imbibition and drainage processes, it can be that values of Vp will actually navigate between the patchy and uniform behavior, as pore size distribution also affects the distribution of liquid and gas inside the rock (Cadoret and Marion, 1995; Cadoret et al., 1993). Figure 15 below shows this tendency for velocity versus water saturation where experimental data in fact fluctuates between patchy and uniform bounds. Figure 15 presents data collected for different limestones submitted to a drainage process and tested at 500 kHz.

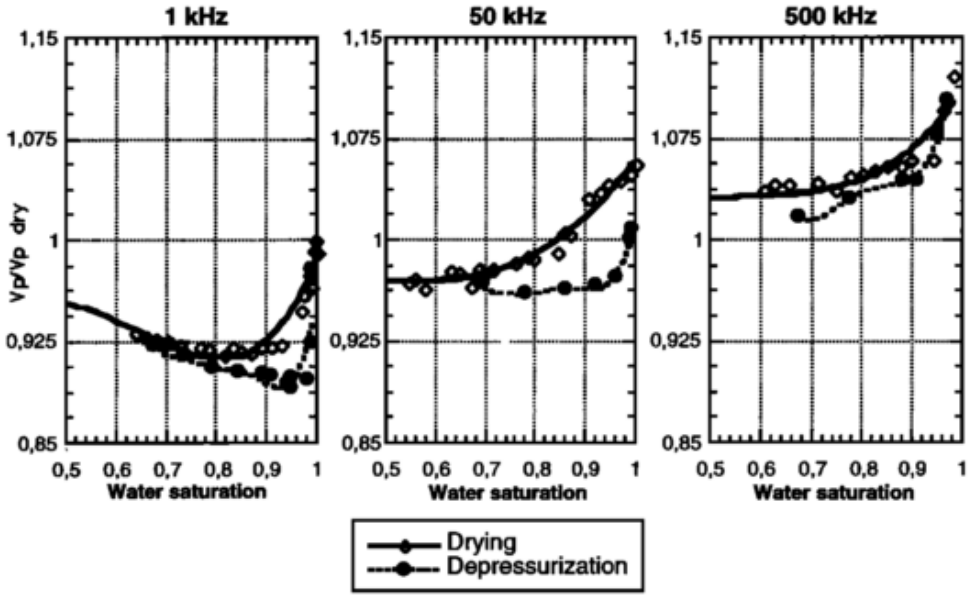

Figure 14. Normalized Vp over Vp-dry versus water saturation for drying and imbibition experiments in different frequency bands done by Cadoret and Marion 1995. Data was obtained for an Estaillades limestone (30% porosity and k=255 mD). Extracted from Cadoret and Marion (1995).

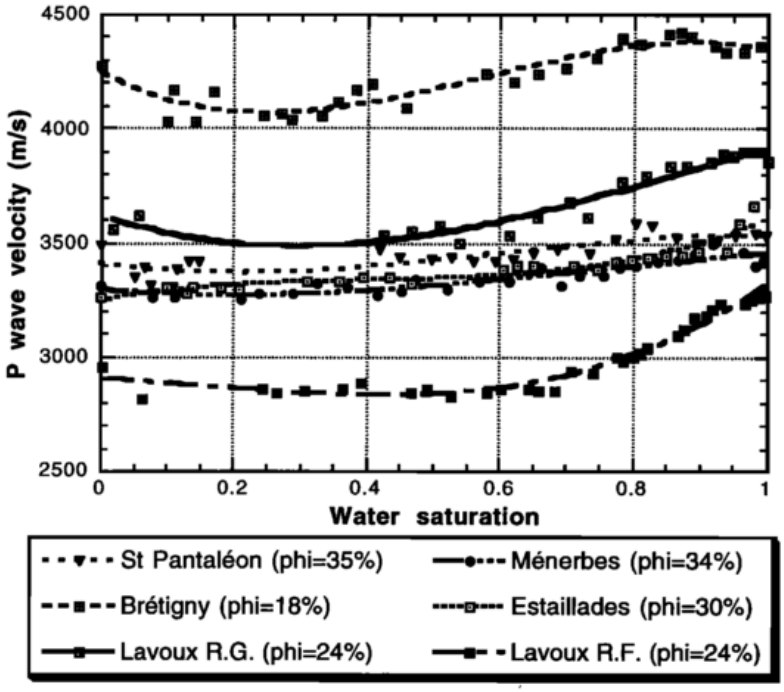

Figure 15. Vp versus Sw measured at 500 kHz on different limestones submitted to drying experiments. Extracted from Cadoret and Marion (1995).

As seen here and in the previous sections, the complexity of the effects of pore fluid on wave velocities and their dependence on porosity, pore size distribution and interaction with the rock matrix make the theoretical prediction of velocity versus saturation an example of one of the most challenging problems in rock physics (Schön, 2015).

2.4 Fluid substitution models

The complexity associated with rock-fluid systems is such that all the theories for these systems need to rely on some major assumptions in order to simplify mathematics and make predictions a practical task (Mavko et al., 2009; Schön, 2015; Wang, 2000). Even with the existence of many models in the literature, there is not a "silver-bullet" model that can precisely describe the effects of pore fluid type and distribution on acoustic parameters in a real underground environment. Nevertheless, one of the most relevant tasks in the rock physics analysis of wellbore logs, core samples and seismic data is the usage of acoustic velocities in rocks saturated with one fluid in order to predict those of rocks saturated with another fluid, analogously, estimating saturated-rock velocities from dry-rock velocities or the other way around (Mavko et al., 2009). This kind of task is defined in the literature as the "fluid substitution problem". Here, it is important to notice that most approaches for fluid substitution simulation rely on the estimation of velocities from its relation with the effective bulk moduli, shear moduli and density of the porous medium, usually using the formulas for Vp and Vs discussed in Section 2.2. Consequently, in this section the discussion is focused on different methods for the estimation of effective elastic modulus.

For instance, one of the most classical and commonly used models for predicting fluid saturation and distribution using acoustic wave velocity, or vice-versa, is the one based on the developments done by Gassmann in 1951 (Berryman and Milton, 1991; Berryman, 1999; Gassmann, 1951). Gassmann's model elegantly describes the saturated-rock effective bulk moduli from dry-rock moduli, estimating a stiffening of effective bulk modulus for the saturated rock. This model was originally derived for situations with a single saturating fluid, but partial saturation conditions can be analyzed by combining Gassmann's equation with methodologies to calculate an effective modulus for the mixture of fluids. There are some different methodologies for this purpose, nevertheless, there are two widely-used formulations that describe the lower and the upper bounds for the Gassmann's model (Berryman, 1999; Mavko and Mukerji, 1998). The lower bound for the effective fluid mixture bulk moduli was developed by Reuss (Reuss, 1929) and describes the ratio of the average stress to the average strain when there is homogeneous stress within all components. Therefore, this bound represents an **isostress** situation. On the other hand, the upper bound for the effective bulk moduli of a fluid mixture was developed by Voigt (Voigt, 1910) and describes the ratio of average stress to the average strain when there is homogeneous strain within all components. For this reason, it describes an **isostrain** situation. These two bounds proposed by Reuss and Voigt give a range of possible values for the effective bulk moduli inside the Gassmann's formulation and consequently, in practice, any outcome between those bounds is possible. Alternatively, Hashin-Shtrikman (HS) bounds, which incorporate the use of shear modulus in the prediction of bulk modulus, could be used for the upper and lower bound of Gassmann's equation (Gassiyev, 2008; Hashin and Shtrikman, 1963). Nevertheless, if we consider HS bounds only for the calculation of the effective fluid moduli used as input at Gassmann's, assuming both fluids to have zero resistance to shearing, which is a good assumption for most fluids not under high pressures, the Hashin-Shtrikman bounds collapse to the lower bound produced by Gassmann-Reuss. Important to notice that Gassmann's formulation did

not consider the existence of patches of fluids in the porous medium and was developed for low frequency waves, therefore its upper bound tend not to be a good representation of a true patchy behavior observed in underground reservoirs. Consequently, alternatives to Voigt fluid mixing rule are needed in order to better represent the patchy behavior observed in real systems. One common approach for this is the usage of empirical correlations, such as the one proposed by Brie (Brie et al., 1995). In the Figure 16, it is possible to visualize the differences between the values produced by the Gassmann bounds and the Brie fluid mixing rule. Also, Figure 16 shows that Brie's methodology can be used to produce any value between the upper and lower bounds of Gassmann by adjusting its coefficient "e".

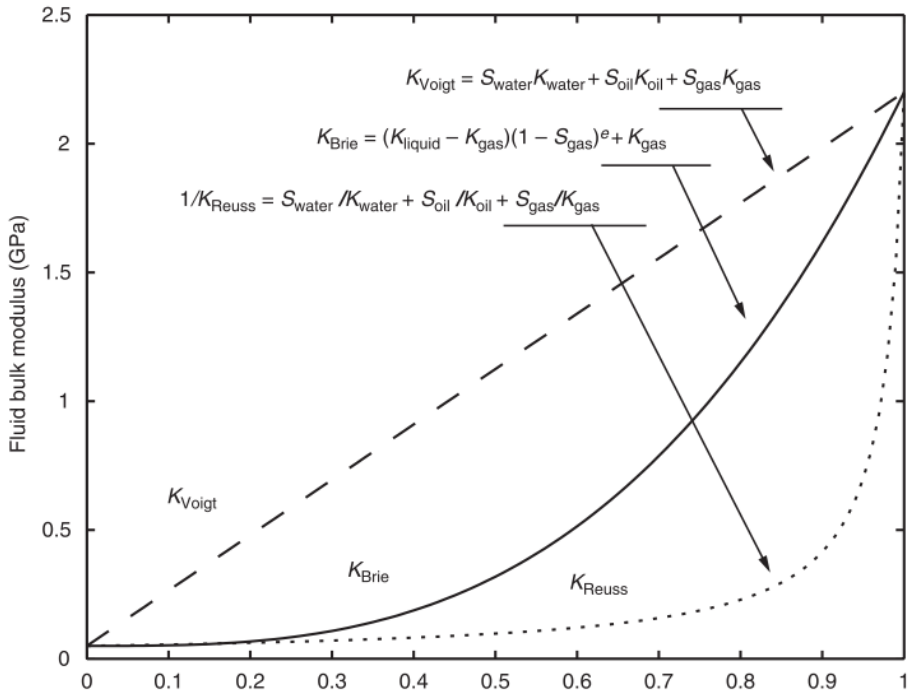

Figure 16. Illustrative comparison of different methods for calculating effective fluid bulk moduli proposed by Voigt, Reuss and Brie. Extracted from Mavko et al. (2009)

Alternatively, Dominique Paul Marion developed during his doctoral studies at Stanford University (Marion, 1990) a promising heuristic method that uses an average between the upper and lower theoretical bounds to describe how velocities and elastic moduli change during the substitution of fluids. For this reason, the method is also known as Bound Averaging Method (BAM), which in reality can be applied to any upper and lower bounds. However, Marion used Hashin-Shtrikman or Voigt-Reuss bounds for rocks saturated exclusively with one fluid (Marion and Nur, 1991; Marion, 1990), therefore, the application of this method for partial fluid saturation conditions is still lacking. Anyways, the idea behind BAM is that the fractional vertical position within bounds was a measure of the pore geometry and is independent of the pore-filling properties. This method was successfully applied for predicting water-saturated rock velocities from dry-rock velocities, predicting ice-filled rock velocities from water saturated velocities and hydrocarbon-filled rock velocities from dry-rock velocities (Marion and Nur, 1991; Marion et al., 1992; Marion, 1990; Mavko et al., 2009).

As an option to Gassmann's methodology, it has been shown in the literature that models based on Biot's theory of wave propagation (Biot, 1962, 1956a, 1956b) are a more appropriate option to describe patchy saturation conditions, especially those considering fluid patches in the mesoscopic scale and incorporating fluid migration between different patches due to pore pressure gradients. Therefore, mesoscopic-scale models tend to describe patchy saturations better than local and macro-scale models (Diallo et al., 2003; Morgan et al., 2012; Pride et al., 2004). In this context, the first models to merge these factors were developed by White (1975) and White et al. (1975) using approximations of the Biot theory. White's (1975) model was derived assuming spherical gas patches, or pockets, in a water saturated porous medium. Figure 17 below presents the mesoscopic fluid distribution idealized by this model. Dutta and Seriff (1979) solved the model proposed by White (1975) exactly using Biot theory and found a correction to the model, which was the mistakenly usage of rigidity (M) instead of bulk modulus (K) in the expressions

for calculate wave quality factor and extensional K. This correction improved and attested the effectiveness of the model. Furthermore, Carcione et al. 2003 used numerical-modeling experiments based on White's model and showed that attenuation and velocity dispersion could be explained by the effect of mesoscopic-scale heterogeneities and energy transfer between wave modes (Carcione et al., 2003). In the case of White et al. (1975) model, the derivation assumes periodic layers of different lithology or of different saturating fluids in the same host rock. Therefore, in other words, it considers a periodic layering of heterogeneities, as shown in the Figure 18. Furthermore, Carcione et al. (2006) used numerical simulations to indicate that mesoscopic loss could be the dominant attenuation mechanism at seismic frequencies, since the observed velocity dispersion (dependence to frequency) and attenuation could be related to mesoscopic variations of the rock and pore fluid (Carcione and Picotti, 2006). In fact, both of these models, regardless of their pioneering aspect, continue to be used in the present due to their relative mathematical simplicity and effectivity (Carcione and Picotti, 2006; Morgan et al., 2012). Moreover, these models have been shown to adequately capture the behavior of real patchy systems, as Dutta and Seriff (1979) pointed out that the geometry of the patches are not significant and, thus, the physics aspects of the models have relative validity for real patchy systems.

After the publication of these two models there was the proposition of further refinements of the mesoscopic loss theory, as for example the contributions done by Gelinsky and Shapiro (1997), Gurevich and Lopatnikov (1995), Gurevich et al. (1997), Johnson (2001), Müller and Gurevich (2005), Norris (1993), Pride et al. (2004), Shapiro and Muller (1999), Toms et al. (2007). For instance, Johnson (2001) developed a model generalizing the spherical White's model for patches of any arbitrary shape, requiring as input two additional geometrical parameters: the size of the patches and their surface area. In Gurevich et al. (1997) it was found that for a 1-dimensional finely layered system the compressional quality factor (Qp) was approximately given

by the harmonic average of the equivalent single Qp's. They considered Biot's loss (macroscale), scattering and mesoscopic loss. Müller and Gurevich (2005) performed numeral simulations for wave velocity and attenuation in a 1-dimensional random patchy saturation model, where heterogeneities are presented in the form of layers. In their case, they found a peak for attenuation at 80% Sw for the seismic frequency band.

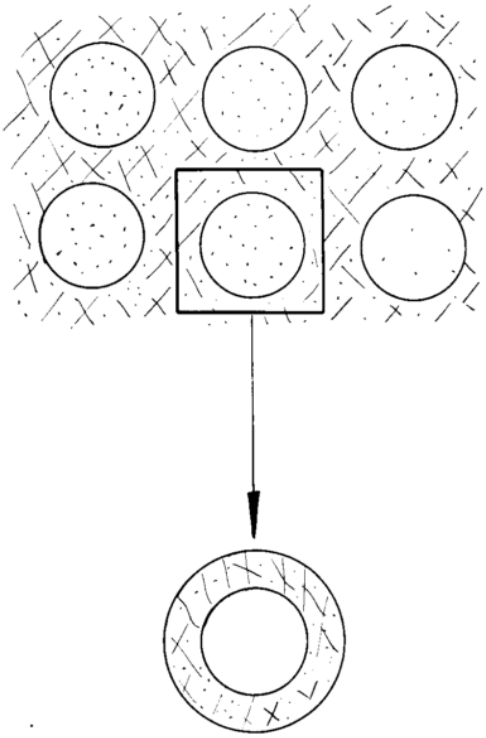

Figure 17. White's model considering the fluid distribution as spherical pockets saturated with gas intervening volume saturated with liquid. In the model, the volume considered in the calculations is the pair of concentric spheres shown in the lower part of the figure. Extracted from White (1975).

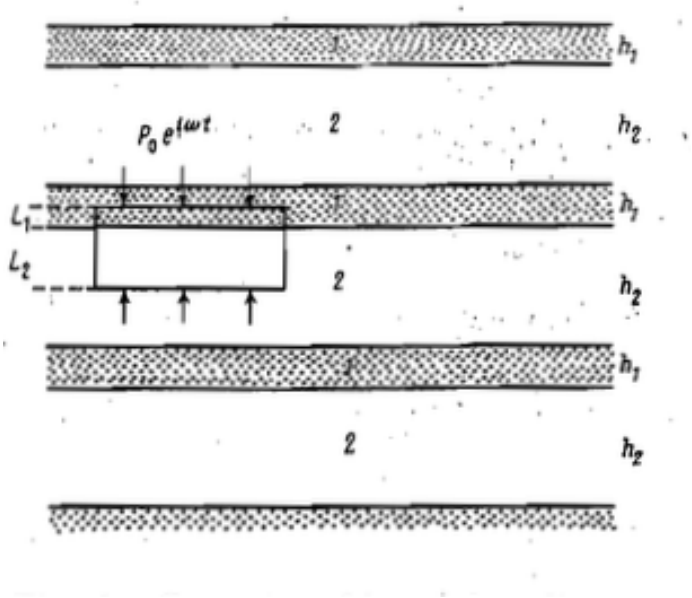

Figure 18. Distribution of the periodic saturated layered medium considered in the model of White et al. (1975). Extracted from White et al. (1975).

Toms et al. (2007) developed a 3-dimensional patchy saturation model assuming random distribution of patches in a 3D volume. In fact, their model is a generalization of the model developed by Müller and Gurevich (2005) for a 3-dimensional random distribution of fluid patches.

Besides the evidence available in the literature that point out the effectiveness of these more complex fluid substitution models, Gassmann's bounds still widely used in the industry for fluid substitution simulations. Moreover, all these models are commonly used to evaluate acoustic field data generated at conditions that do not fully satisfy some assumptions of the models (Best et al., 2004; Liu et al., 2002; Morgan et al., 2014, 2012; Vanneste et al., 2015). Therefore, there is still a need for experiments that can compare the performance of these models. In this work, special attention is given to the layered patchy saturation distribution assumed in the layered patchy model of White et al. (1975).

Chapter 3

Problem Statement

The aim of this work is to investigate the effectiveness of different theoretical and empirical patchy saturation models in predicting acoustic wave velocities for specific saturation distribution scenarios produced in laboratory. Therefore, different patchy and homogeneous fluid distributions were created for bench-scale experiments and the samples were tested using two ultrasonic wave frequencies (100 and 250 kHz). Gassmann-Voigt bound is widely used for the analysis of acoustic data generated at sonic frequencies, even if Gassmann's theory was developed for the analysis of low frequency seismic waves. It also represents a theoretical upper limit for velocities in patchy saturation conditions and, therefore, might not always be optimal to represent real field data. Empirical models, popularly the one proposed by Brie (1995), are commonly used to fit/describe velocity trends observed in acoustic surveys. Models based on Biot's theory, as the layered patchy model of White et al (1975) and the spherical patchy model of White (1975), are also widely used but are more mathematically complex and require more input parameters. Thus, this work presents a comparison between the predictions of these models mentioned here and the velocities measured experimentally for different patchy saturations.

Chapter 4

Methodology

The investigation process of this work was based on the implementation of experiments followed by experimental data processing, interpretation and discussion and also on efforts to elucidate which patchy model better predicts P-wave velocity for the saturation distributions evaluated in this work. In order to give an overview of the research process, the flow chart below (Figure 19) is presented.

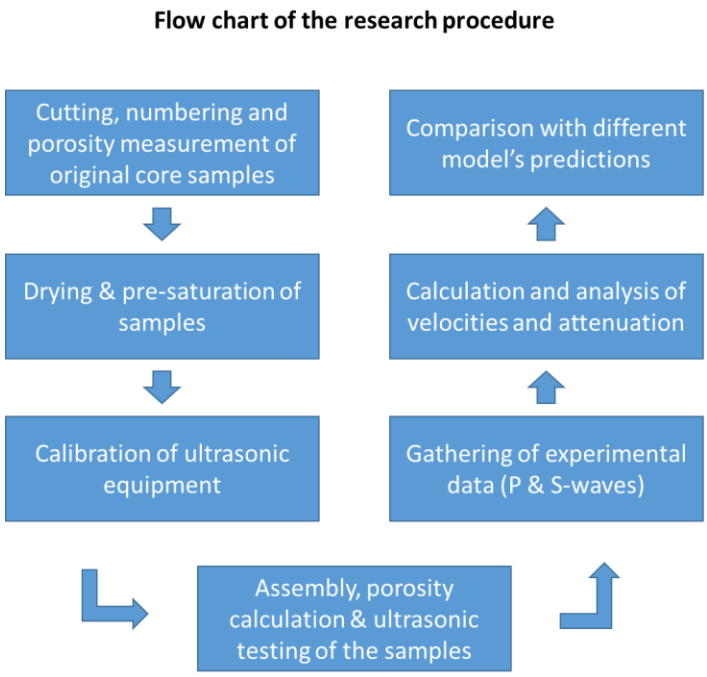

Figure 19. General flow chart of the research procedure.

4.1 Velocity Models

The different models investigate in this work were implemented in Matlab in order to check their effectiveness at predicting velocities for the patchy saturation conditions evaluated experimentally. The models analyzed are described in more detail in the next subchapters. For the implementation of White's (1975) spherical model, a Matlab script kindly provided by T. Mukerji through the Rock Physics Handbook (Mavko et al., 2009) was adapted.

For the models described in sections 4.1.1 and 4.1.2, the calculation of P-wave velocities for partially saturated conditions was done using Equation 1, described in section 2.2. Equation 1 requires as inputs the effective saturated rock bulk and shear moduli and density of the saturated rock. The effective saturated rock bulk modulus was given by Gassmann's equation using the methods of Voigt, Reuss and Brie to calculate the effective bulk modulus of the fluid mixture. Effective saturated rock shear modulus was considered to be equal to the one obtained for the dry samples from the ultrasonic measurements, as the saturating fluids used in this work (water and air) were considered to have no shear modulus. The density of the partially saturated rocks was calculated from the following expression:

$$\rho_{saturated\ rock} = \rho_{dry\ rock} + \phi(\rho_{fluid\ mixture} - \rho_{air})$$

$$\rho_{fluid\ mixture} = Sw * \rho_{water} + (1 - Sw) * \rho_{air}$$

Where:

$\rho_{saturated\ rock}$ = density of the saturated rock [kg/m^3]
$\rho_{dry\ rock}$ = density of the dry rock [kg/m^3]
ϕ= porosity of the rock [fraction]
$\rho_{fluid\ mixture}$ = density of the fluid mixture [Pa]

ρ_{air} = density of air [Kg/m^3]

ρ_{water} = density of water [Kg/m^3]

Sw = water saturation [fraction]

Therefore, the P-wave velocities obtained from the models described in sections 4.1.1 and 4.1.2 are different because the equations used to determine the effective bulk modulus of the fluid mixture were not the same. Hence, sections 4.1.1 and 4.1.2 focus on presenting these equations and their underlying assumptions. The models described in sections 4.1.3 to 4.1.4 have different methodologies to calculate P-wave velocity.

4.1.1 Gassmann's Model

As mentioned in the literature review, Gassmann's model elegantly describes the saturated-rock effective bulk moduli from dry-rock moduli, estimating a stiffening of effective bulk modulus for the saturated rock. The equation below shows this relationship.

$$\frac{K_{sat}}{K_0 - K_{sat}} = \frac{K_{dry}}{K_0 - K_{dry}} + \frac{K_{fl}}{\emptyset * (K_0 - K_{fl})}$$

$$\mu_{sat} = \mu_{dry}$$

Where:

K_{dry} = effective bulk modulus of the dry rock [Pa]

K_{sat} = effective bulk modulus of the saturated-rock [Pa]

K_0= effective bulk modulus of the mineral rock frame [Pa].

K_{fl} = effective bulk modulus of the porous fluid [Pa]

$\emptyset$ = estimated porosity for the investigated formation [ratio].

μ_{sat} = effective shear modulus of the saturated rock [Pa].

μ_{dry} = effective shear modulus of the dry rock [Pa].

It is important to notice that in the original formulation of Gassmann it is considered that the dry-rock status corresponds to a state where pore pressure is held constant, which can be achieved when the pore fluid is allowed to freely flow in or out of the porous medium or where the pore fluid itself has no bulk modulus. This dry-rock condition would only truly be achieved if there was no pore fluid, for example, by appropriately submitting the rock to a vacuum oven. In practical terms, the dry bulk moduli are taken from an air-filled sample submitted to standard pressure and temperature, as in this case the bulk modulus of the air is extremely small. Moreover, as already discussed in the chapter 2.3.2, extremely dry rock samples are not adequate as a reference, since a small absorption of moisture significantly reduces the frame moduli. Therefore, a better reference for dry-rock bulk moduli to be used in Gassmann's equation is the one measured at a slightly moist rock sample. In fact, this is adopted for any fluid substitution model. Additionally, classical Gassmann's formulation considers the rock to be homogeneous and isotropic and disregards the geometry of the pores or the distribution of fluids in the porous medium. Fluids are assumed to have no resistance to shearing and, therefore, the effective fluid shear modulus for the saturated and dry conditions are the same. Furthermore, in Gassmann's model there is no pore pressure gradient and so no relative motion between the fluids and the rock frame when acoustic waves passes thought the medium (Berryman, 1999; Dewar, 2001; Müller et al., 2010; Schön, 2015; Toms et al., 2006).

As a direct consequence of Gassmann's approach, partial saturation situations ask for a methodology describing the effective bulk moduli of the fluid mixture. As mentioned in the literature review, there are two methodologies that describe the upper and the lower bound of Gassmann's equation (Berryman, 1999; Mavko and Mukerji, 1998). The lower bound for the effective fluid mixture bulk moduli was developed by Reuss (Reuss, 1929) and is given by the equation below, which describes the ratio of the average stress to the average strain when there is homogeneous stress within all components. Therefore, this bound represents an **isostress** situation.

$$\frac{1}{K_{Reuss}} = \sum_{i=1}^{n} \frac{S_i}{K_i}$$

Where:

K_{Reuss} = effective bulk modulus described by Reuss [Pa]

S_i = saturation of the fluid "i" [ratio]

K_i= bulk modulus of the fluid "i" [Pa]

On the other hand, the upper bound for the effective bulk moduli of a fluid mixture was developed by Voigt (Voigt, 1910) and describes the ratio of average stress to the average strain when there is homogeneous strain within all components. For this reason, it describes an **isostrain** situation. This upper bound is given by the equation below.

$$K_{Voigt} = \sum_{i=1}^{n} K_i * S_i$$

Where:

K_{Voigt} = effective bulk modulus described by Voigt [Pa]

S_i = saturation of the fluid "i" [ratio]

K_i= bulk modulus of the fluid "i" [Pa]

These two bounds proposed by Reuss and Voigt give a range of possible values for the effective bulk moduli inside the Gassmann's formulation and consequently, in practice, any outcome between those bounds is possible. It is known from the literature that the lower bound of Gassmann's equation describes relatively well situations where the different fluid components are mixed at the finest scale, as stress heterogeneities in the porous medium caused by the fluid distribution are smaller than the Critical Length (Lc) and tend to be neutralized during the passage of an acoustic wave (Mavko et al., 2009; Schön, 2015; Winkler and Murphy III, 1995). On the other hand, the Voigt upper bound gives a theoretical upper limit for patchy fluid distributions, where saturation heterogeneities are larger than the critical length and have no time to equilibrate. Important to notice that Gassmann's formulation did not consider the existence of patches of fluids in the porous medium and was developed for low seismic frequency waves, therefore, its upper bound tend not to be a good representation of a true patchy behavior observed in underground reservoirs. Moreover, Gassmann considers that the rock is isotropic, all minerals composing the rock have the same shear and bulk moduli and that rock is completely saturated with a single fluid.

4.1.2 Brie's empirical fluid mixing equation

One of the most common approaches for describing velocity measurements between the upper and lower bound of Gassmann's models is the usage of empirical equations, which adjust

the velocity predictions to an observed experimental dataset through tuning parameters. In this framework, the method proposed by Brie (Brie et al., 1995) is a popular option and uses a cementation constant "e" to do this tuning task, which typically has values around 3. The expression developed by Brie to calculate the bulk moduli of a mixture of fluids is the one described below.

$$K_{Brie} = \left(K_{liquid} - K_{gas}\right) * \left(1 - S_{gas}\right)^{e} + K_{gas}$$

$$\frac{1}{K_{liquid}} = \sum_{i=1}^{n} \frac{S_{liquid_i}}{K_{liquid_i}}$$

Where:

K_{Brie} = effective bulk modulus of the fluid mixture described by Brie [Pa]
S_{gas} = saturation of the gas in the mixture [ratio]
K_{liquid}= effective bulk modulus of the liquid described by Reuss [Pa]
K_{liquid_i}= bulk modulus of the liquid "i" [Pa]
K_{gas}= bulk modulus of the gas [Pa]
e = empirical cementation constant [dimensionless]

Brie' method does not really have assumptions, but using such a purely empirical approach would incur some disadvantages, as predictions could greatly succumb to measurement error and also require data collection prior to the usage in the field for fluid substitution simulations.

4.1.3 White et al. (1975) layered patchy model

This section nearly reproduces the model developed by White et al. (1975) , corrected by Norris (1993), and also presented by Carcione and Picotti (2006), therefore, in order to have more details about this model, it is recommended to read these papers. This patchy model is based

on Biot's theory and considers a system with periodic layers of porous media saturated with fluids 1 and 2, gas and water, respectively, which have thickness d_l (l = 1, 2) and period d_1+d_2. These layers of heterogeneous saturation are considered to be much larger than the grains but much smaller than the wavelength.

Moreover, White's layered model assumes that the rock and its mineral are isotropic and that the porosity of the layered patches is uniform. The complex bulk modulus of a P-wave travelling perpendicular to the direction of periodic layering is given by:

$$E = \left[\frac{1}{E_0} + \frac{2(r_2 - r_1)^2}{i\omega(d_1 + d_2)(I_1 + I_2)}\right]^{-1}$$

where

$$\omega = f * 2\pi$$

is the angular frequency. Saturation of fluid "j" is given by

$$S_j = \frac{d_l}{d_1 + d_2}$$

$$E_0 = \left[\frac{S_1}{E_{G_1}} + \frac{S_2}{E_{G_2}}\right]^{-1}$$

Moreover, omitting the subscript j for clarity, we have for each medium

$$E_G = K_G + \frac{4}{3}\mu_m$$

K_G is the Gassmann modulus described below and μ_m is the dry-rock shear modulus.

$$K_G = K_m + \alpha^2 M$$

where

$$\alpha = 1 - \frac{K_m}{K_s}$$

and

$$M = \frac{K_s}{1 - \emptyset - K_m/K_s + \emptyset K_s/K_f}$$

where K_s is the solid-grain mineral bulk modulus, K_m is the dry-rock bulk modulus, K_f is the fluid bulk modulus. Moreover, we have that the ratio of fast P-wave fluid tension to total stress is

$$r = \frac{\alpha M}{E_G}$$

and impedance related to the slow P-wave is

$$I = \frac{\eta}{\kappa k} \coth(\frac{kd}{2})$$

The complex wavenumber of the slow P-wave is given by

$$k = \sqrt{\frac{i\omega\eta}{\kappa\, K_E}}$$

and effective modulus is described as

$$K_E = \frac{E_m M}{E_G}$$

where

$$E_m = K_m + \frac{4}{3}\,\mu_m$$

is the dry rock fast P-wave modulus. The average density is given by

$$\rho_{ave} = S_1\left[(1-\phi)\rho_s + \phi\rho_{fl1}\right] + S_2\left[(1-\phi)\rho_s + \phi\rho_{fl2}\right]$$

The complex velocity is defined as

$$v^2 = \frac{E}{\rho_{ave}}$$

the loss angle is given by

$$\theta = \tan^{-1}\left[\frac{Im(v^2)}{Re(v^2)}\right]$$

with Im and Re denoting the imaginary and real components, respectively. Finally, we obtain, in this order, the quality factor and P-wave velocity via

$$Q^{-1} = \tan\theta$$

$$Vp = \left(\frac{E}{\rho_{ave}}\right)^{0.5} / \cos\left(\frac{\theta}{2}\right)$$

4.1.4 White's (1975) spherical patchy model

This appendix nearly reproduces the model developed by White (1975), corrected by Dutta and Seriff (1979), and also presented by Carcione et al. (2003) and Mavko et al. (2009), therefore, in order to access more details about this model, one should refer to these papers. This model is based on Biot's theory and considers a system with periodic spherical gas pockets that are larger than the grains but much smaller than the wavelength. Moreover, White's spherical model assumes that the rock and its minerals are isotropic and that the porosity of the spherical patches is uniform.

This model considers spheres of porous medium with radius "a" saturated with gas and located in a cube of porous medium saturated with water. In order to simplify the calculations, White considers an outer sphere of radius "b" involving the inner gas pocket, where the volume of the outer sphere is equal to the original cube. Therefore, saturation of the inner fluid is given by:

$$S_1 = \frac{a^3}{b^3}$$

Where subscript j=1 refers for the inner region and subscript j=2 for the fluid in the outer shell. The complex bulk modulus for the partially saturated rock is given by:

$$K = \frac{K_\infty}{1 - K_\infty W} = K_r + iK_i$$

where

$$\omega = f * 2\pi$$

$$W = \frac{3a^3(R_1 - R_2)(-Q_1 + Q_2)}{b^3 i\omega(Z_1 + Z_2)}$$

$$R_1 = \frac{K_1 - K_{dry_1}}{1 - \frac{K_{dry_1}}{K_{0_1}}} * \frac{3K_2 + 4\mu_2}{K_2(3K_1 + 4\mu_2) + 4\mu_2(K_1 - K_2)S_1}$$

$$R_2 = \frac{K_2 - K_{dry_2}}{1 - K_{dry_2}/K_{0_2}} * \frac{3K_1 + 4\mu_1}{K_2(3K_1 + 4\mu_2) + 4\mu_2(K_1 - K_2)S_1}$$

$$Z_1 = \frac{\eta_1 a}{\kappa_1}\left[\frac{1 - e^{-2\alpha_1 a}}{(\alpha_1 a + 1) + (\alpha_1 a + 1)e^{-2\alpha_1 a}}\right]$$

$$Z_2 = -\frac{\eta_2 a}{\kappa_2}\left[\frac{(\alpha_2 b + 1) + (\alpha_2 b - 1)e^{2\alpha_2(b-a)}}{(\alpha_2 b + 1)(\alpha_2 a - 1) - (\alpha_2 b - 1)(\alpha_2 a + 1)e^{2\alpha_2(b-a)}}\right]$$

$$\alpha_j = \left(\frac{i\omega\eta_j}{\kappa K_{E_j}}\right)^{\frac{1}{2}}$$

$$K_{E_j} = \left[1 - \frac{K_{f_j}\left(1 - \frac{K_j}{K_{0_j}}\right)\left(1 - \frac{K_{dry_j}}{K_{0_j}}\right)}{\phi K_j\left(1 - \frac{K_{f_j}}{K_{0_j}}\right)}\right] K_{A_j}$$

$$K_{A_j} = \left(\frac{\phi}{K_{f_j}} + \frac{1 - \phi}{K_{0_j}} - \frac{K_{dry_j}}{{K_{0_j}}^2}\right)^{-1}$$

$$Q_j = \frac{(1 - K_{dry_j}/K_{0_j})K_{A_j}}{K_j}$$

Here, K_j and μ_j are the saturated bulk and shear moduli, respectively, of region j calculated from Gassmann's equations using the bulk and shear moduli for the dry rock and the bulk moduli of the fluid in the region j (K_{f_j}). η and K_f are the fluid viscosity and bulk modulus, respectively. ϕ is the porosity, κ is permeability, K_0 is the bulk modulus of the solid mineral grains. Assuming dry-frame properties are the same in both regions, at the high-frequency limit, when there is no fluid flow between the regions 1 and 2, the bulk modulus is given as

$$K_{\infty_{(no-flow)}} = \frac{K_2(3K_1 + 4\mu_2) + 4\mu_2(K_1 - K_2)S_1}{(3K_1 + 4\mu_2) - 3(K_1 - K_2)S_1}$$

In the low-frequency, where fluid pressure is constant and uniform throughout the porous medium, the bulk modulus is given by Gassmann's equation using Reuss average for fluid modulus and, therefore, is described as

$$K_{(low-frequency)} = \frac{K_2\left(K_1 - K_{dry}\right) + S_1 K_{dry}(K_2 - K_1)}{\left(K_1 - K_{dry}\right) + S_1(K_2 - K_1)}$$

The average density is given by

$$\rho_{ave} = S_1\left[(1 - \phi)\rho_s + \phi\rho_{fl1}\right] + S_2\left[(1 - \phi)\rho_s + \phi\rho_{fl2}\right]$$

The complex velocity is defined as

$$v^2 = \frac{K}{\rho_{ave}}$$

and the loss angle is given by

$$\theta = \tan^{-1}\left[\frac{Im(v^2)}{Re(v^2)}\right]$$

with “Im” and “Re” denoting the imaginary and real components, respectively. Finally, we obtain, in this order, the quality factor and P-wave velocity via

$$Q^{-1} = \tan\theta$$

$$Vp = \left(\frac{K}{\rho_{ave}}\right)^{0.5} / \cos\left(\frac{\theta}{2}\right)$$

4.1.5 Average Vp

The applicability of an average P-wave velocity based on a methodology used in seismology was noticed during the realization of the experiments. It was seen that knowing the water saturation of the sample and P-wave velocity for the dry and fully water saturated conditions, it was possible to predict with accuracy the velocity for intermediate layered patchy saturations. The calculation of this average P-wave velocity is based on the time necessary for the acoustic wave to travel through the wet and dry sections of the sample and is given by the equations below.

$$Sw = \frac{Hw}{Ht}$$

$$Vp_{average} = \frac{Ht}{\frac{H_{wet}}{Vp_{wet}} + \frac{H_{dry}}{Vp_{dry}}}$$

$$Vp_{average}{}^{-1} = \frac{\frac{H_{wet}}{Vp_{wet}} + \frac{H_{dry}}{Vp_{dry}}}{Ht}$$

$$Vp_{average}{}^{-1} = \frac{Sw}{Vp_{wet}} + \frac{(1 - Sw)}{Vp_{dry}}$$

$$Vp_{average}^{-1} = \left[Sw * Vp_{wet}{}^{-1}\right] + \left[(1 - Sw) * Vp_{dry}{}^{-1}\right]$$

$$Vp_{average} = \frac{1}{\frac{Sw}{Vp_{wet}} + \frac{(1 - Sw)}{Vp_{dry}}}$$

Where:

Sw = water saturation [fraction].

Hw= Summation of the heights of the fully water saturated sections [meters].

Ht= Total height of layered saturated sample [meters].

Vp_{dry}= P-wave velocity measured experimentally for the dry condition [meter/second].

Vp_{wet}= P-wave velocity measured experimentally for the fully water saturated condition [meter/second].

$Vp_{average}$= P-wave velocity inferred from an averaged wave slowness [meter/second].

These calculations assume that all sections are either totally dry (air saturated) or fully water saturated, therefore, the knowledge about fluid saturation is sufficient to calculate the average Vp, dispensing the need to know the thickness of the layers. Hence, the average Vp is calculated from the time taken by the acoustic wave to travel through all the wet and all dry

sections of the sample. This average P-wave velocity is similar to the Reuss average, but using velocities instead of moduli. Moreover, as mentioned previously, this average velocity is based on concepts used in seismology, where wavelength is much smaller than the size of the heterogeneities (Aki and Richards, 2009).

4.2 Core Samples

In this work, the rock used throughout the experiments was Berea Sandstone provided by the company Cleveland Quarries, based in Vermilion, Ohio. The core samples were supplied in the cylindrical format and had a uniform diameter of approximately 2 inches and a length of around 6 inches, as illustrated in Figure 20.

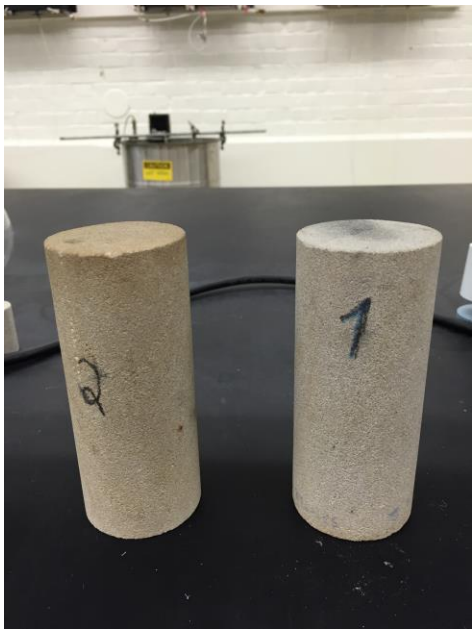

Figure 20. Example of a Berea sandstone "core sample" used in the experiments.

The samples were free of fractures and considered to be homogeneous and isotropic. The permeability reported by Cleveland Quarries for the samples was 300 milidarcy (mD), which was assumed to be true for all core samples. The composition of the rocks was assumed to follow the information provided by the supplier, which is presented in the Table 2. Nevertheless, as the rocks were dominated by silica, we assumed that the mineral frame had a bulk modulus of 37 GPa and shear modulus of 44 GPa.

Table 2. Composition of the Berea Sandstone as reported by the supplier.

Silica	SiO_2	93.13%
Alumina	AI_2O_3	3.86%
Ferric Oxide	Fe_2O_3	.11%
Ferrous Oxide	FeO	.54%
Magnesium Oxide	MgO	.25%
Calcium Oxide	CaO	.10%

As previously mentioned in the Objectives section, the ultimate goal of this work was to investigate the wave velocity response to different saturation distributions, especially patchy saturations. In order to achieve different patchy saturations, different samples were assembled using pieces of rock of know saturation; therefore, it was possible to create sharp and well-defined saturation distribution patterns.

For the sake of this work, **core samples** are defined as the original rock samples extracted from the mine, which were later cut for the purpose of this work. Also, we define the terms **"pieces of rock / rock pieces"**, or simply **"pieces"**, as the pieces of rock that were cut down from the original core sample. Therefore, **samples** are defined as any combination of **pieces of rock** that are set between ultrasonic transducers and submitted to an ultrasonic test. For example, Figure 21 shows three different samples, each made from 5 pieces of rock. The process of cutting, drying and pre-saturating the pieces of rock, as well as the stacking of the pieces in order to form samples of different saturation distributions, is described in the following sections.

Figure 21. Difference between "sample" and "piece of rock". In this figure we see three different "samples" that were made of 5 "pieces of rock" each, or simply "pieces".

4.3 Preparation of core samples

4.3.1 Cutting, numbering and porosity measurement

After receiving the samples, the same were numbered according to the order of reception, thus, creating a chronological numbering system. When the samples were cut into smaller pieces using a rotating diamond saw, each piece received a number corresponding to a sublevel of the original sample number. For example, if core sample 1 was cut into 2 smaller parts, there would be the pieces 1.1 and 1.2. Figure 22 below illustrates this cutting and numbering procedure.

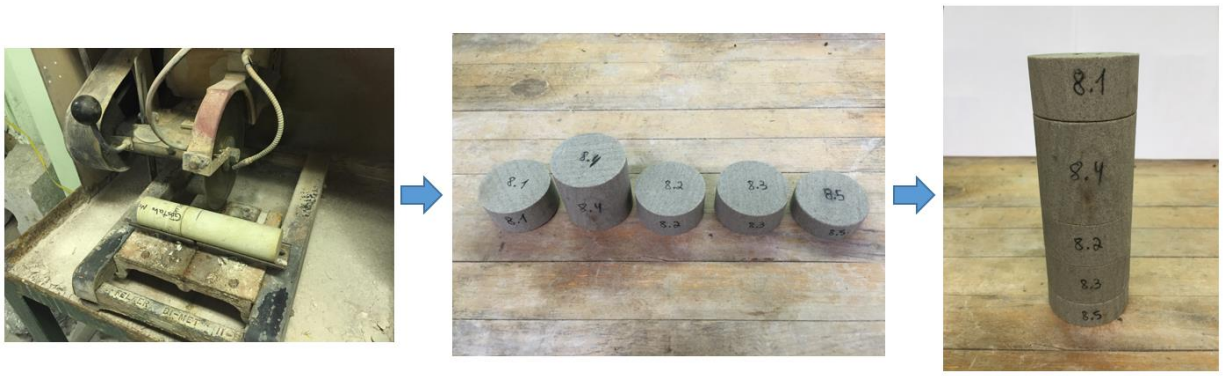

Figure 22. Process of cutting the core samples and numbering the pieces of rock.

The porosity was expected to be between 13% and 23% as reported by the vendor, nevertheless, in order to get precise porosity data, mercury intrusion porosimetry tests were performed at the Materials Characterization Laboratory (MCL) of the Pennsylvania State University (Penn State) for each of the core samples used in this study. This kind of test gets information on porosity by applying pressure to samples immersed in mercury and tracking pressure response in order to determine porosity, pore volume, average pore size, pore size distribution and pore area. The machine used at MCL, a Micromeritics AutoPore V Model 9620, can reach pressures of 60,000 psi, test samples with dimensions smaller than 1 inch and measure pore sizes between 0.003 and 360 microns. The porosity values obtained for the different core samples are presented in Table 3. Except for the porosity value of Sample 2, which is understood to have been caused by an error in the measurement or by measuring a highly cemented part of the core sample, the porosity values are pretty close to each other and also within the expectations set by the supplier of the rocks. The average pore diameter presents some variation within the samples, nevertheless, they have the same order of magnitude and are not significantly far from each other. This information is also shown in Table 3.

Table 3. Porosity values obtained for the different core samples from the mercury intrusion porosimetry tests.

Core Sample Number	Porosity (%)	Average Pore Diameter (μm)	Core Sample Number	Porosity (%)	Average Pore Diameter (μm)
Core Sample 1	22.928	0.449	Core Sample 5	21.102	0.505
Core Sample 2	6.256	0.237	Core Sample 6	20.655	1.170
Core Sample 3	21.169	0.537	Core Sample 7	21.152	0.912
Core Sample 4	21.310	0.589	Core Sample 8	19.952	1.091

4.3.2 Drying and Pre-saturation procedure

Prior to the drying and pre-saturation of the pieces of rock, the same had their dimensions measured with a caliper or a high precision ruler. Afterwards all the pieces were submitted to the drying process in order to get an approximate 100% gas saturation situation. This process was done even for the pieces that would later be submitted to the pre-saturation process. For this step, I used a conventional electrical oven, which had no mechanism to increased convection, such as fans. The samples were left inside the oven for at least 6 hours at 60º Celsius in order to secure appropriate drying. Right after the pieces were removed from the oven, the same were weighed on a high precision scale in order to avoid the absorption of moisture, thus, making it possible to get the weight of the rock at the truly dry condition. These values of weight, combined with the values of porosity, were later used as reference for the calculation of the water saturation of the samples by checking the difference of weight between the dry and the wet conditions. The process of drying was always repeated before starting a new imbibition cycle.

For the pre-saturation (imbibition) of the samples with water, it was chosen to implement the Barnes experiment procedure, since it was relatively easy to execute and expected to achieve the water saturation (Sw) levels designed for this work. Indeed, it was possible to reach Sw values as high as 96%. A 100% water saturation condition was not achieved possibly because the pre-saturation process did use water at high pressure. The first step in this pre-saturation procedure was to determine the weight of the rock at dry conditions, as described above. Afterwards, the dry samples were put inside a dry Erlenmeyer and submitted to vacuum for at least 15 minutes or until the achievement of a sufficiently low pressure inside the glass compartment. A vacuum pump and a pressure gauge connected to the pump were used in order to assure that a satisfying vacuum condition was obtained. After this condition was achieved, the vacuum pump was turned off and a slowly introduction of water inside the Erlenmeyer was implemented using a burette until the pieces of rock were completely immersed in water. The pieces were left immersed in water and under vacuum for approximate 30 minutes so an equilibrium condition could be obtained and the piece of rock would have achieved the highest water saturation possible. Finally, the vacuum condition was removed and the pieces of rock left for extra 15 minutes in the water. Afterwards, they had their excess water gently removed with a paper towel and had their weight measured. Figures 23 and 24 show in more detail the pre-saturation setup itself. As the experiments were carried out at room temperature, approximately at 20^{o} Celsius, and atmospheric pressure, we considered in all the calculations of this work that the viscosity, density and bulk moduli of water and air are equal to the ones described in the literature for standard conditions. These parameters are presented in Table 4.

Table 4. Fluids properties used in this work.

Fluid	Viscosity (Pa.sec)	Density (kg./m3)	Bulk moduli (GPa)
Water	0.003	1000	2.20
Air	0.001695	1.291	0.000101

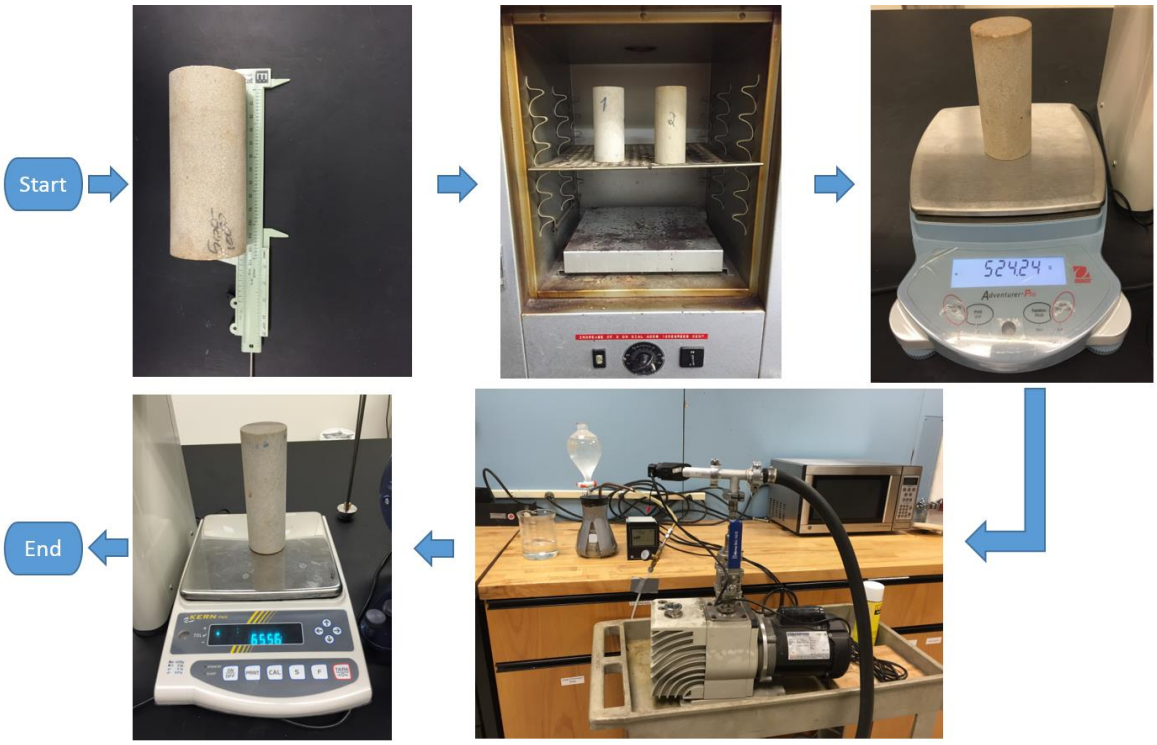

Figure 23. Overview of the drying and Barnes experiment process executed in order to pre-saturate samples with water.

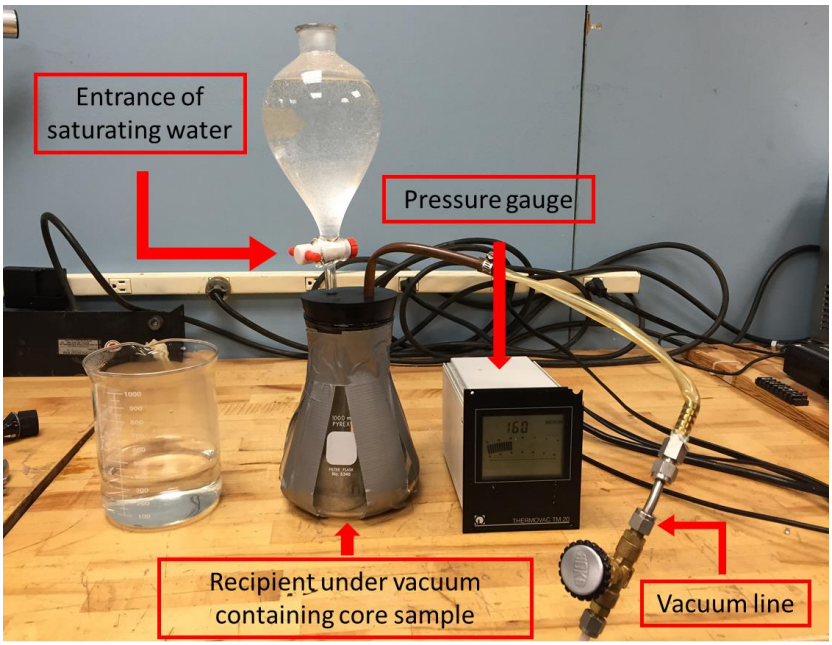

Figure 24. Barnes experiment setup shown in more detail.

In order to achieve pre-determined saturation levels lower than the ones obtained with the pre-saturation process, the rock pieces were drained on a laboratory bench at open-air condition, therefore, under atmospheric pressure and room temperature and humidity, after being submitted to the imbibition cycle. Figure 25 below, we have water saturation versus time for three different sizes of rock pieces submitted to this open-air drainage cycle on a laboratory bench. The curves contained in Figure 25 were used to predict, control and achieve pre-determined saturation levels for each sample. In addition, the drawings of the rock pieces in Figure 25 are in scale and represent the lengths of 2'', 1'' and 1 centimeter.

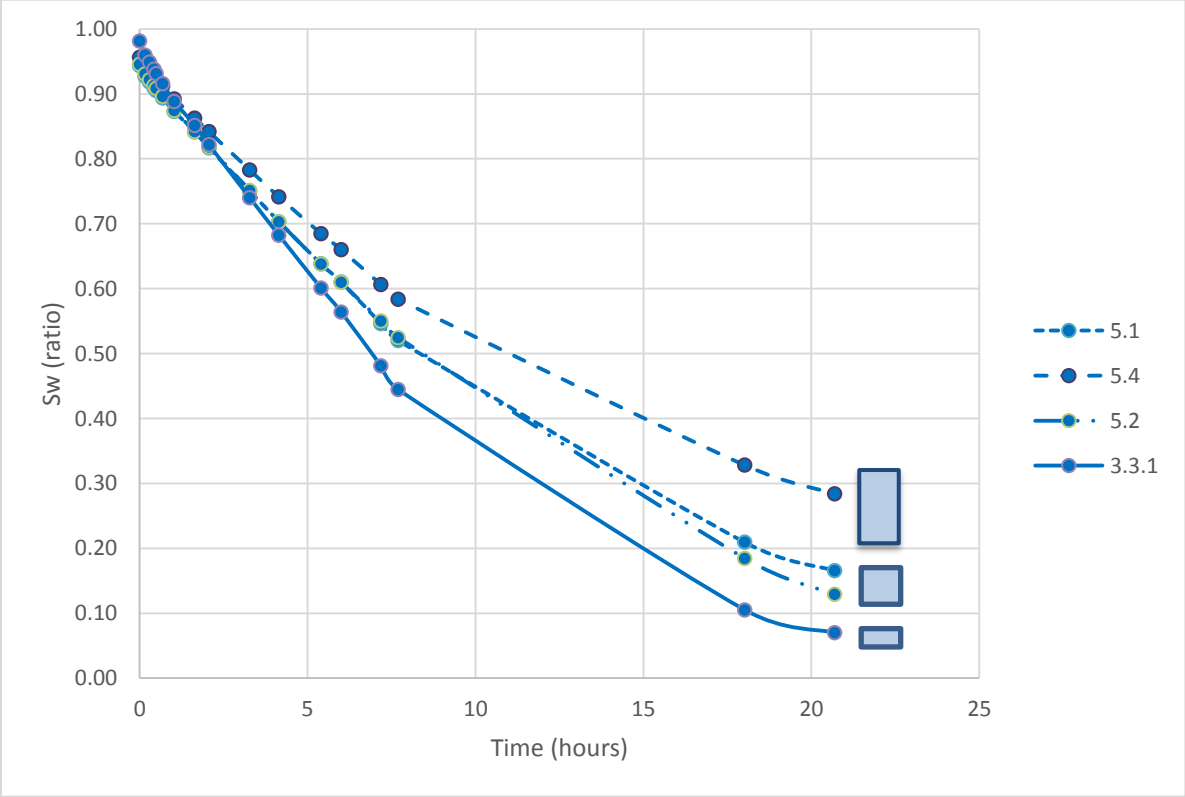

Figure 25. Water saturation versus time for rock pieces of different scales, showing the influence of size on the velocity of draining at room temperature and pressure. These curves were used to control and achieve pre-determined saturation goals for the samples.

From the interpretation of Figure 25, it is possible to observe that there is a relationship between the size of a piece of rock and the speed of the drainage process at room temperature and pressure. Figure 25 indicates that the larger the volume of the rock, the slower the process of drainage. This behavior was expected, as it is intuitive to imagine that a sample with smaller volume offers shorter paths to be travelled by a molecule of water willing to escape from the inner most parts of the rock. Therefore, reducing the time taken by the molecules to travel from inside to outside of the porous. Besides the fact that different amounts of time were required to achieve the same saturation level for different rock pieces, it is considered that the fluid distribution within the rocks was the same, as all core samples had very similar porosities and pore size distribution.

4.3.3 Assembly of samples

After all the pieces of rock were dried and/or pre-saturated, the different samples were put together by stacking the pieces as convenient to form the different saturation distributions that were object of this work. Therefore, by stacking pieces of different or equal water saturation it was possible to form precise and well described uniform and layered patchy saturation distributions. It is important to notice that by the time the samples were submitted to the ultrasonic tests, the different pieces of rock were stacked with a layer of coupling between them in order to enable the wave to properly propagate and reduce these horizontal discontinuities. The different samples tested in this work are presented in Figure 27. Figure 26 shows an example of one of these samples.

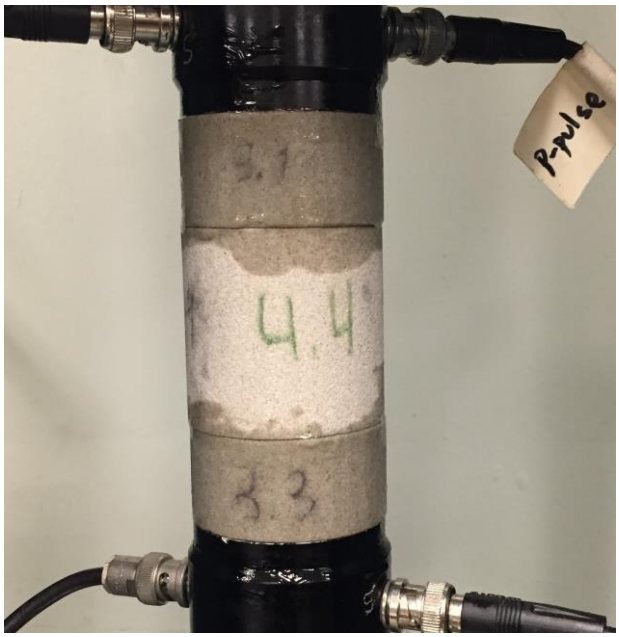

Figure 26. Example of a sample tested in the study.

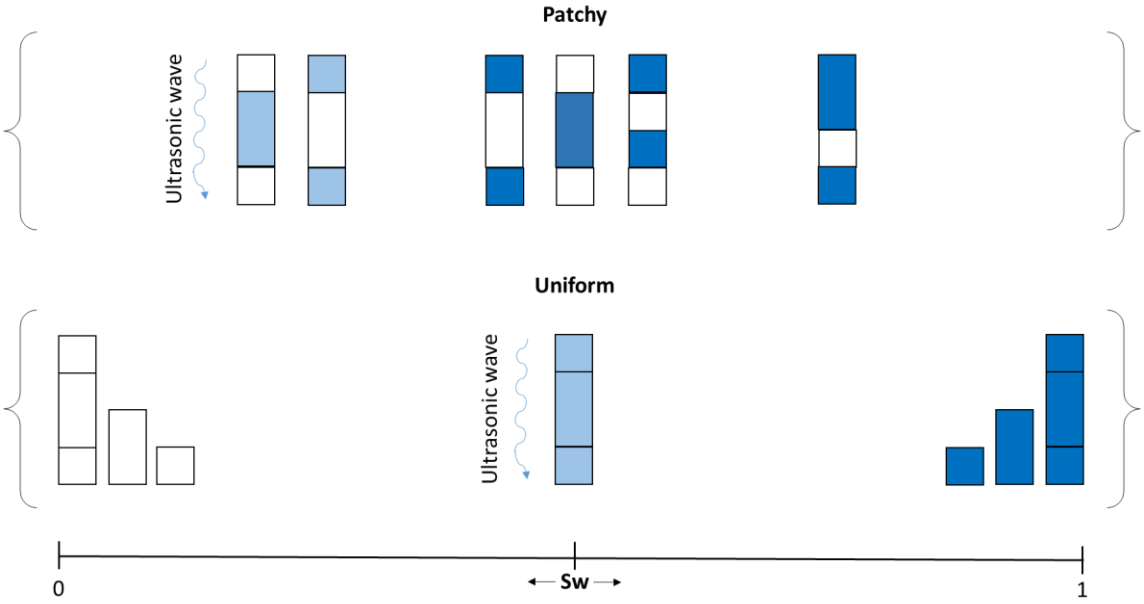

Figure 27. Overview of the different samples used to investigate different fluid distribution conditions. White colored parts represent fully gas saturated zones, dark blue parts are fully water saturated zones and light blue represents partially water saturated zones. The upper part of the figure presents the samples that were designed and expected to behave as patchy saturated. The lower part indicates the samples expected to behave as uniformly saturated.

4.3.4 Porosity and saturation calculation

As it can be seen from Figure 26, the samples were not always composed by pieces of rock originating from the same core sample; therefore, the pieces sometimes had different porosity values. Hence, the correct average porosity value for the samples needed to be calculated using the volume and the porosity of each pieces as inputs. Since all the pieces of rock had the same diameter, the formula used to calculate the average porosity was based on the height and porosity of the pieces, as described in the equation that follows below.

$$\emptyset_{sample} = \sum_{i}^{n} \frac{h_i * \emptyset_i}{\sum_{i=1}^{n} h_i}$$

Where:

$\emptyset_{sample}$ = average porosity of the sample.

$\emptyset_i$ = porosity of the piece of rock "i".

h_i = height of the piece of rock "i".

For the determination of the saturation of the sample, first it was necessary to calculate the saturation of each piece of rock using the difference between their weight at the dry and saturated condition, as shown in the formula below.

$$Sw_{piece} = \frac{(W_{water\ wet} - W_{dry})}{\rho * Vol * \emptyset}$$

Where:

Sw_{piece} = water saturation of the piece of rock [ratio].

W_{dry} = weight of the piece of rock at the dry condition [grams].

$W_{water\ wet}$ = weight of the piece of rock at the water wet condition [grams].

ρ = density of the water [grams/cm^3].

Vol = volume of the piece of rock [cm^3].

$\emptyset$ = porosity of the piece of rock.

Afterwards, the same procedure was implemented for the calculation of the average water saturation of the sample. Here, the only difference was the usage of the height of each piece to define the contribution of each piece for the average saturation. This "height averaged saturation" was possible because the pieces had the same diameter and, therefore, the height is the parameter controlling the difference of volume between the pieces. The following equation describes this calculation.

$$Sw_{sample} = \sum_{i}^{n} \left\{ \frac{(W_{water\ wet,i} - W_{dry,i})}{\rho * Vol_i * \emptyset_i} * \frac{h_i}{\sum_i^n h_i} \right\}$$

Where:

Sw_{sample} = average water saturation of the sample [ratio].

$W_{dry,i}$ = weight of the piece of rock "i" at the dry condition [grams].

$W_{water\ wet,i}$ = weight of the piece of rock "i" at the water-wet condition [grams].

ρ = density of the water [grams/cm^3].

Vol_i = volume of the piece of rock "i" [cm^3].

$\emptyset_i$ = porosity of the piece of rock "i".

h_i = height of the piece of rock "i" [cm].

4.4 Ultrasonic testing

4.4.1 Equipment and Environment specifications

The ultrasonic equipment used in this study was located at Penn State's Civil Infrastructure Testing and Evaluation Laboratory (CITEL). The testing room was acclimatized, maintained at around 24º C (75º F) and 20% humidity. Moreover, the same was equipped with a self-leveling desk available for testing the samples.

The ultrasonic tester could be used with different transducers of variable frequencies and wave polarizations. In the case of this study, the frequency used for Compressional and Shear waves was 100 kHz and 250 kHz and the polarization of the S-wave was normal to the surface of the transducer transmitting the wave. Piezoelectric transducers branded as "Videoscan" and supplied by Olympus Corporation were used in this work for both P an S waves. The sampling rate was set as 50 MHz and the wave recording time was 300 microseconds.

4.4.2 Preparation and testing of the sample

Prior to testing any sample, it was necessary to calibrate the equipment in order to accurately detect the time that it takes for the waves to travel between the casings of the transducers generating and receiving the pulse. This specific travel time was defined as Face-to-Face Arrival Time (FTFT) and was obtained experimentally at the beginning of each testing cycle, for both compressional and shear waves, by identifying the first positive peak in the wave signal. Knowing the FTFT was important for the later calculation of the velocities of the P-wave and S-wave for the different samples, as it was necessary to discount the FTFT from the

measured arrival time, as stated in the formula below. Figure 28 shows the setup for determining the FTFT by putting the transducers face to face to each other and performing the ultrasonic test with the appropriate coupling between the transducers.

$$AT = AT_{measured} - FTFT$$

Where:

AT = corrected wave arrival time [seconds].

$AT_{measured}$ = wave arrival time measured when testing the samples [seconds].

$FTFT$ = Face-to-Face Arrival Time determined from the calibration procedure [seconds].

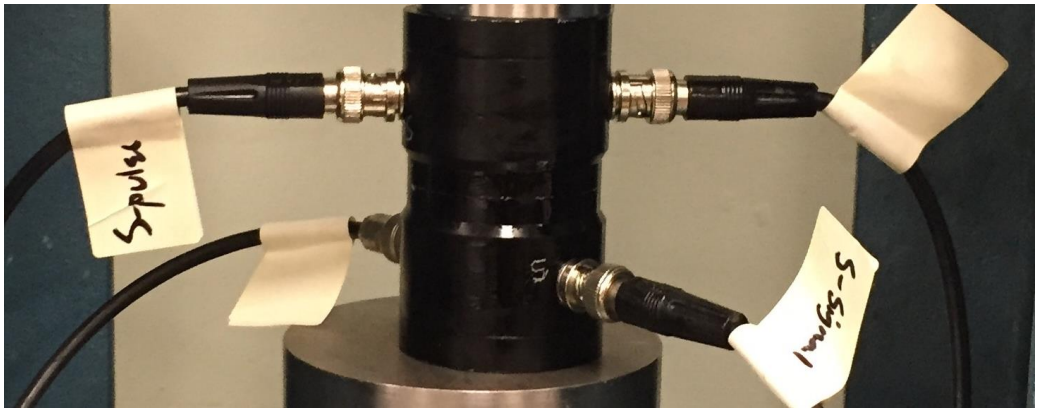

Figure 28. Procedure of calibration of the ultrasonic equipment in order to obtain the face-to-face arrival times for both P-wave and S-wave.

Moreover, prior to testing the samples, the same had all their contact surfaces between rock pieces and rock piece/transducer coupled with an appropriate coupling gel, chosen depending on the kind of ultrasonic wave tested. For shear wave testing the couplant of choice was molasses, due to its viscosity characteristics. For compressional waves, the couplant was a synthetic gel developed specifically for ultrasonic testing, branded as “Sonix” and provided by Echo Ultrasonics LLC.

After finishing the coupling, the samples were held tied between the transducers by the application of hand-pressure on the top transducer. It is important to notice that before performing the ultrasonic test it was also checked if the alignment between the transducers and rock pieces was as perfect as possible. In the next step, it was necessary to adjust the gain of the ultrasonic signal, for each different sample, in order to guarantee an adequate wave propagation and signal recording. Finally, the ultrasonic wave was measured and recorded three different times for each sample, as by doing so it was possible to check for repeatability and have the possibility to calculate the error between measurements. Figure 29 presents some samples ready to be tested for compressional and shear waves.

Figure 29. Transducers used to transmit and receive the compressional waves (P-waves) and the shear waves (S-waves) through the samples.

4.4.3 Ultrasonic Data processing

The ultrasonic equipment did not have a built-in software specifically oriented for the purpose of this work, instead, it was operated by using the software LabView. This software was

also responsible for gathering the raw data. Scripts developed for Matlab were used to import, process the raw data and determine the arrival times for the waves. Finally, Microsoft Office Excel was used to perform the calculation of velocities, densities and porosities. The velocities, for both compressional and shear waves, were calculated from the basic equation below.

$$Wave\ velocity = \frac{h_{total}}{AT}$$

Where:

h_{total} = total height of the sample [meters].

AT = Wave Arrival Time [seconds].

As can be seen from the previous equation, the only difference in the calculation of the shear wave velocity (Vs) and compressional wave velocity (Vp) was the arrival time. As a result of this, determining the correct arrival time is clearly a critical step in this study. Therefore, the procedure for identification of the time of arrival was a combination of automatic and manual picking. In order words, from an automatic pre-selection of the first wave peak, it was done a manual evaluation of the peaks that represented the true wave arrival time and that did not symbolize noise in the measurement. Figure 30 shows the schematic for picking the first peak for a P-wave and, therefore, calculate the velocities. In Figure 31, we see the same for a S-wave. Observe that in Figure 31 the arrival time was calculated from a peak different from the first peak, as the first peak was interpreted as representing a conversion of the S-wave to a P-wave. In fact, this first peak would produce an arrival time equivalent to the one measured for the P-wave in the same sample.

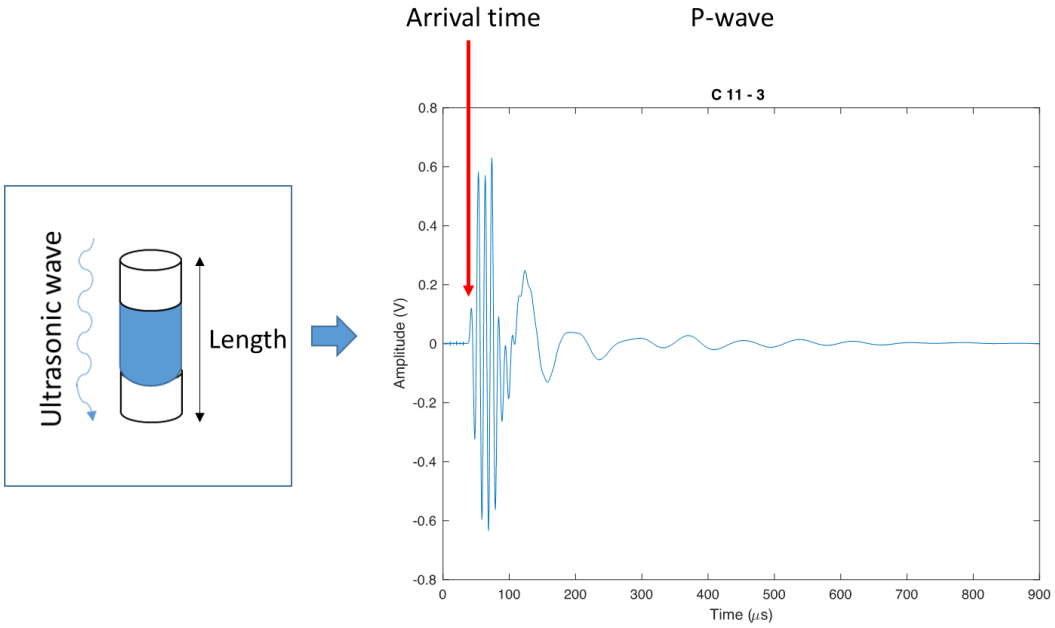

Figure 30. Example of the process of picking the arrival time for the P-wave.

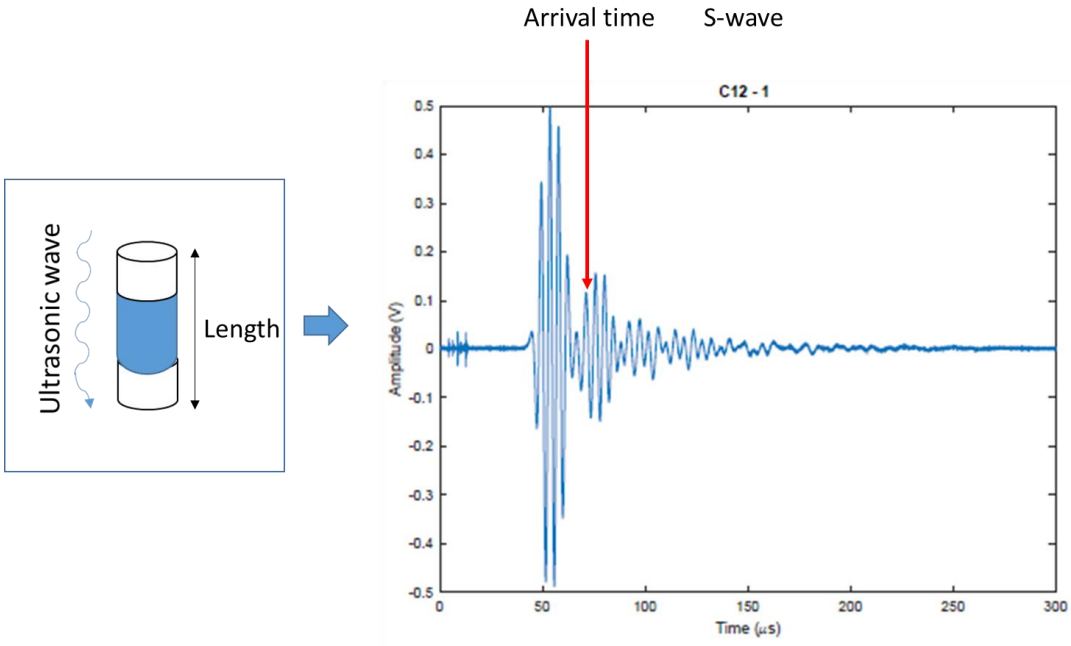

Figure 31. Example of the process of picking the arrival time for the S-wave.

Chapter 5

Results

This chapter presents the different results gathered from the ultrasonic experiments and predictions from the different models. A more thorough discussion of the results is presented in the discussion section. Figure 32 presents in scale the different sample sizes (4", 2" and 1" long) and the various configurations that were tested in this work, as well as the nomenclature adopted for them. In total, there were 13 samples of various fluid distributions. The range of water saturations covered by these samples was approximately from 0% to 96%. Moreover, the different fluid distributions allowed the modeling of water and air as the fluid saturating the fluid patches. For example, sample C-4 has air as the fluid patch and sample C-5 has water as the fluid patch.

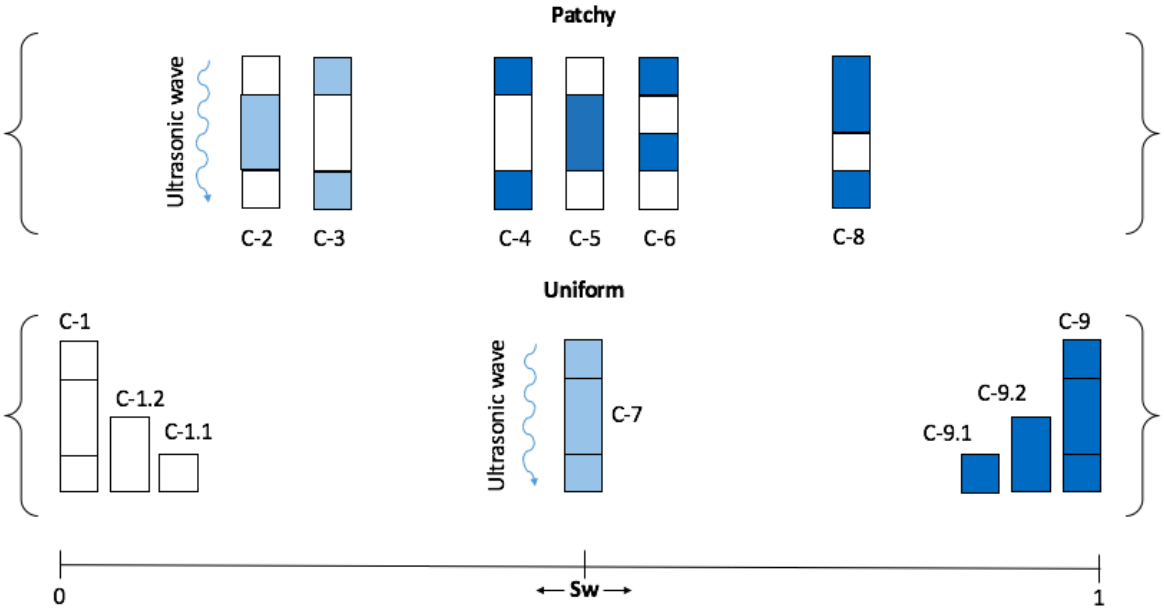

Figure 32. Nomenclature adopted for all the different samples submitted to ultrasonic testing. The upper part of the figure presents the samples that were designed and expected to behave as patchy saturated. The lower part indicates the samples expected to behave as uniformly saturated.

Table 5 and Table 6 present water saturation and ultrasonic results obtained for the samples tested at the wave frequency of 250 kHz and 100 kHz, respectively. Each sample was tested three times in order to identify and avoid outliers; nevertheless, in the Tables 5 and 6 we present only the average and standard deviation of these sets of P-wave velocity measurements. Appendix B shows more thoroughly the data for all individual samples. Figures 33 to 38 present both the average experimental P-wave velocities and their standard deviation. Nonetheless, the standard deviations graphically appear smaller than the points representing the averages for most samples.

Table 5. Water saturation, average wave velocity and its standard deviation for the samples tested at 250 kHz and 100 kHz.

Wave frequency: 250 kHz			
Sample Characteristics		**Average velocity (m/s)**	**Velocity standard deviation (m/s)**
Sample	**Sw (%)**	**P-wave**	**P-wave**
C-1.1	0%	2240.80	4.54
C-1.2	0%	2342.88	2.51
C-1	2%	2247.83	1.49
C-4	47%	2387.39	1.71
C-5	49%	2440.80	2.37
C-9.1	93%	2599.75	8.04
C-9.2	95%	2678.20	1.60
C-9	94%	2638.47	4.83
Sample	**Sw (%)**	**S-wave**	**S-wave**
C-1	2%	1510.80	1.66

Table 6. Water saturation, average wave velocity and its standard deviation for the samples tested at 100 kHz.

Wave frequency: 100 kHz			
Sample Characteristics		**Average velocity (m/s)**	**Velocity standard deviation (m/s)**
Sample	**Sw (%)**	**P-wave**	**P-wave**
C-1	0%	2217.21	6.48
C-2	37%	2084.66	9.77
C-3	38%	2139.90	1.35
C-4	49%	2426.17	3.68
C-5	49%	2468.43	13.80
C-6	49%	2482.11	3.01
C-7	72%	2028.46	1.65
C-8	73%	2577.94	3.95
C-9	95%	2741.26	2.23
Sample	**Sw (%)**	**S-wave**	**S-wave**
C-1	0%	1507.73	1.66

Figures 33 to 38 present the experimental results for Vp versus Sw for the different sample configurations against the predictions made by the Gassmann-Voigt-Reuss bounds, Brie's mixing rule, White's layered model and White's spherical model, respectively. Important to notice that data points in red represent the samples expected to behave accordingly to the Gassmann-Voigt bound (patchy saturation) and the data points in blue represent those anticipated to follow the Gassmann-Reuss bound (uniform saturation). Moreover, we did simulations using the White's models considering different patch saturating fluids (water or air) and different patch sizes, therefore, Figure 34, 35, 37 and 38 have multiple curves that represent these different inputs. Figure 33 to 35 represent the results for the samples tested at 100 kHz and Figure 36 to 38 represent the results for the samples tested at 250 kHz. Moreover, for the calculation of the bulk and shear modulus at the dry condition we used the Vp and Vs (in Tables 5 & 6) measured for the sample C-1 at 100 and 250 kHz; these moduli were used as input for all the models.

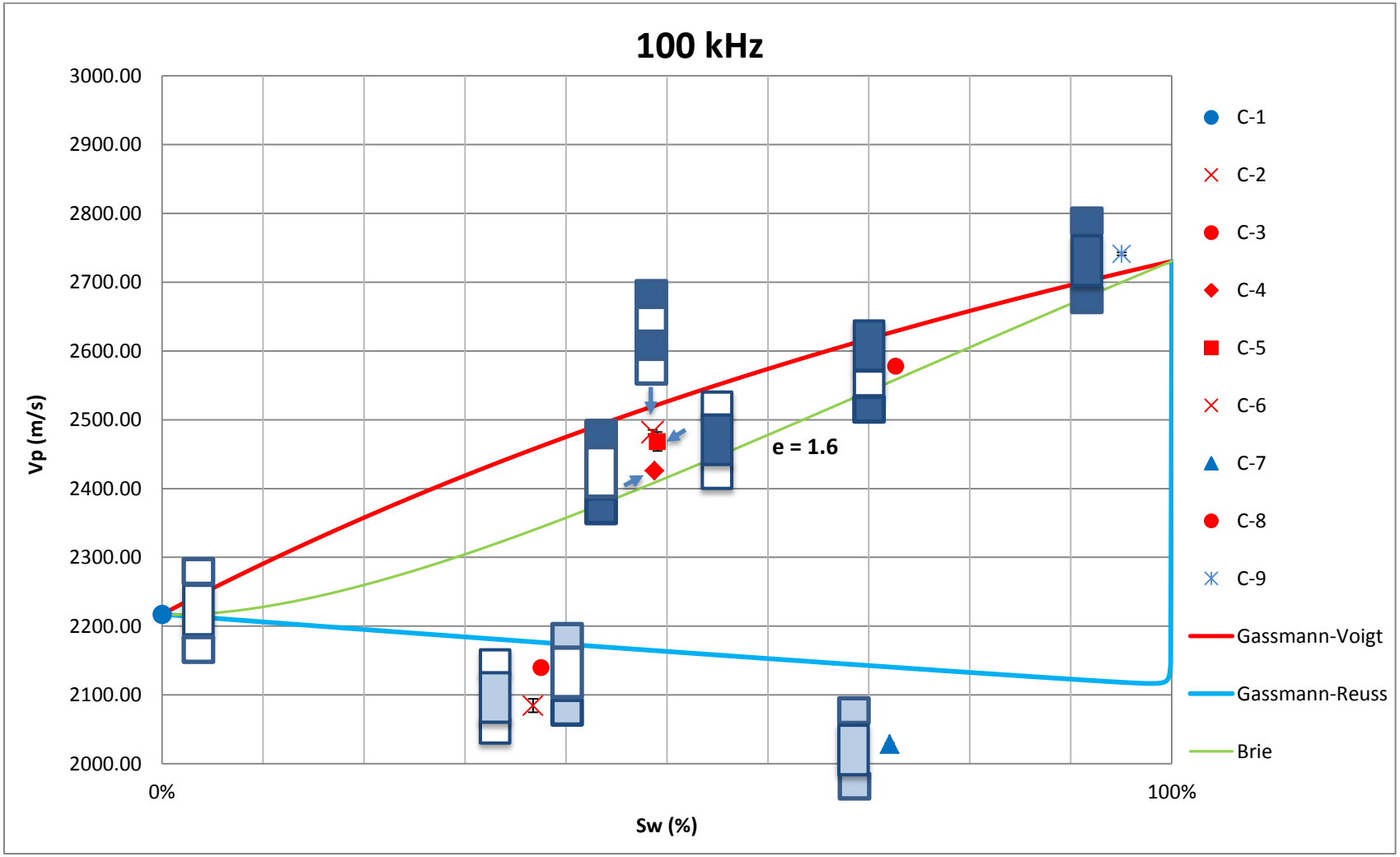

Figure 33. Experimental results for Vp versus Sw for wave frequency of 100 kHz and plotted against the predictions of Gassmann-Voigt-Reuss bounds and Brie's fluid mixing method using constant "e" equal to 1.6. The figures on plot in the format of blue and white blocks represent the different samples and their fluid distribution, which are draw in scale.

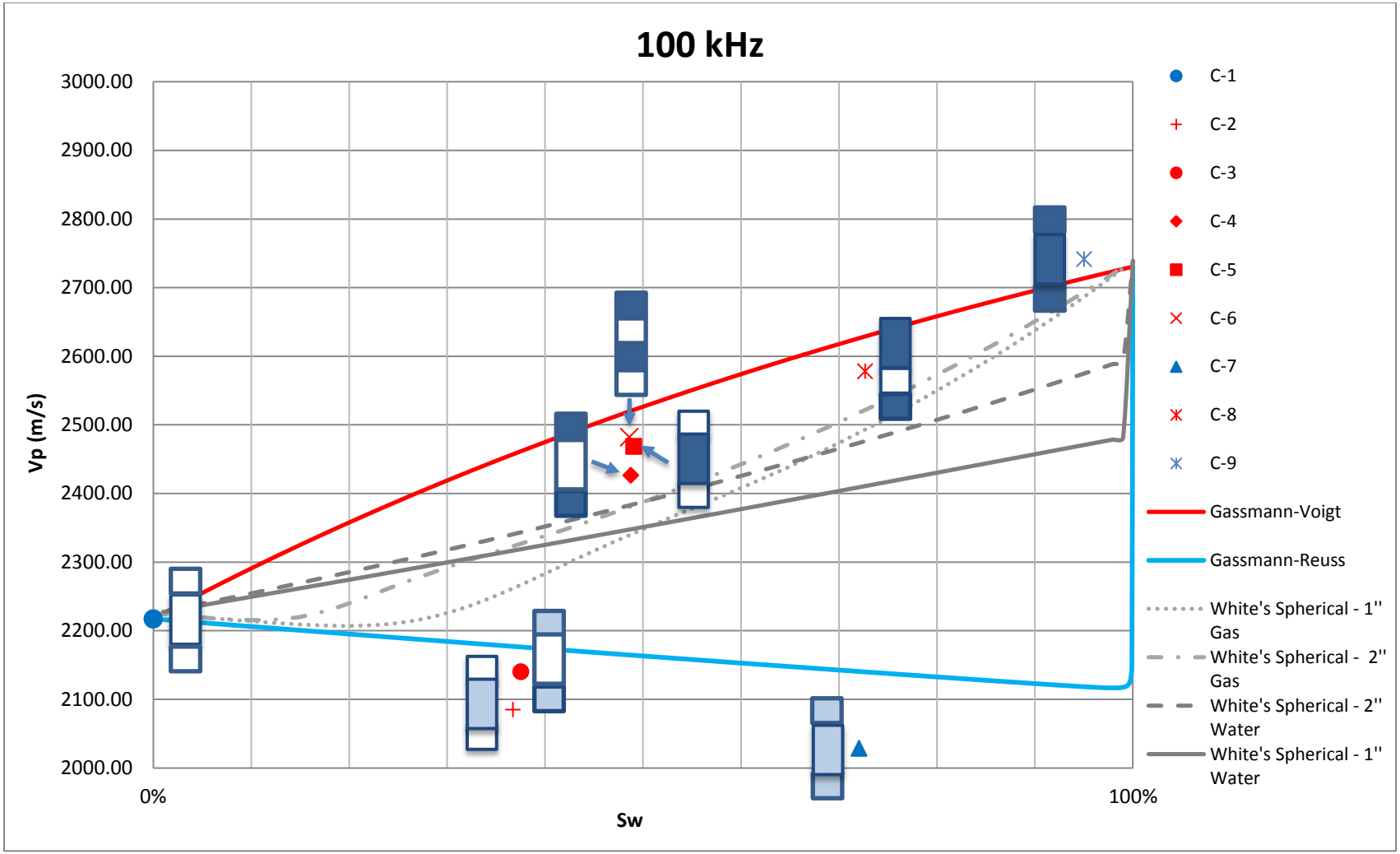

Figure 34. Experimental results for Vp versus Sw for 100 kHz and plotted against the predictions of Gassmann-Voigt-Reuss bounds and White's model for periodic concentric spherical patches. The figures on plot in the format of blue and white blocks represent the different samples and their fluid distribution, which are draw in scale.

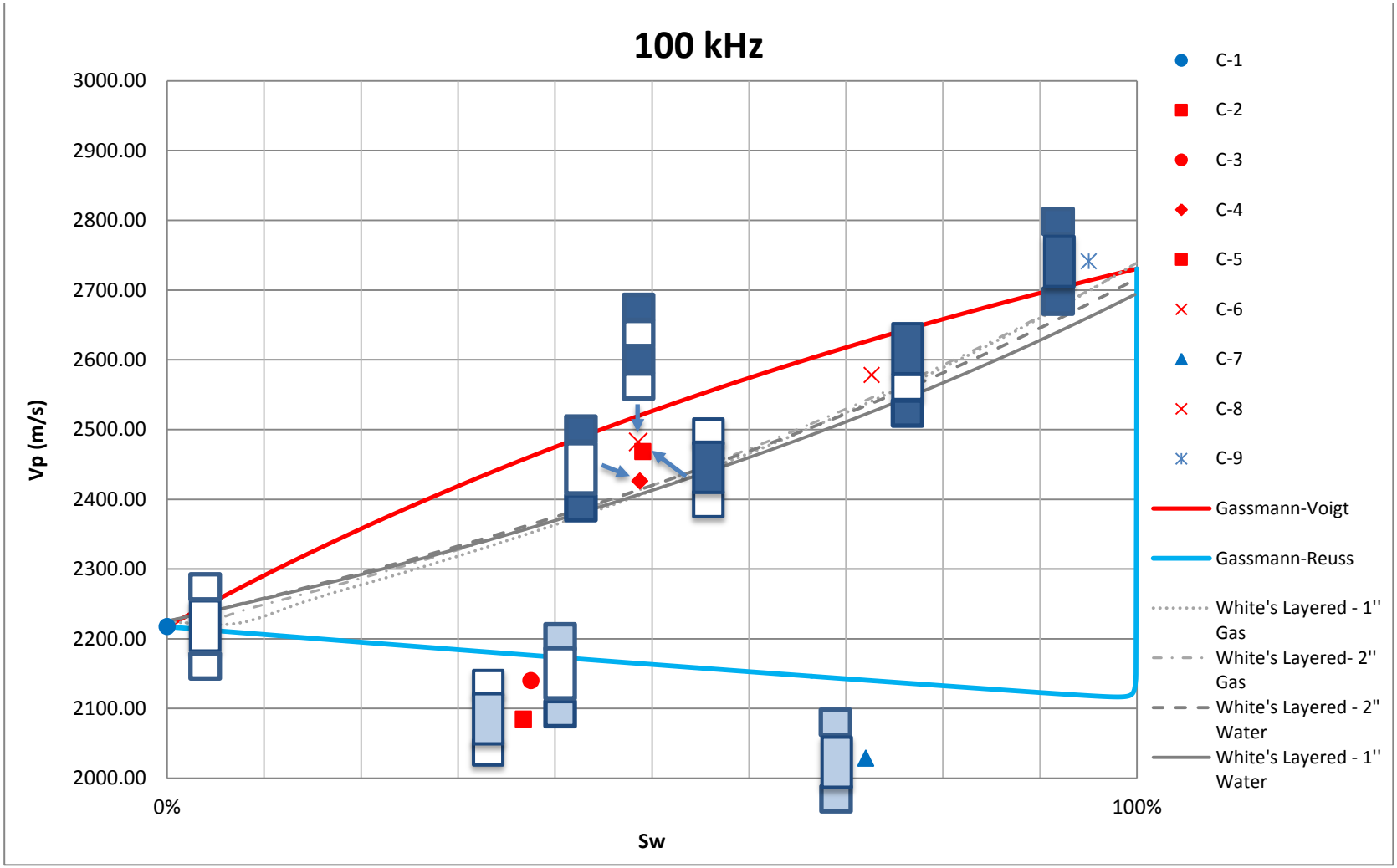

Figure 35. Experimental results for Vp versus Sw for 100 kHz and plotted against the predictions of Gassmann-Voigt-Reuss bounds and White et al. model for periodic layered patch. The figures on plot in the format of blue and white blocks represent the different samples and their fluid distribution, which are draw in scale.

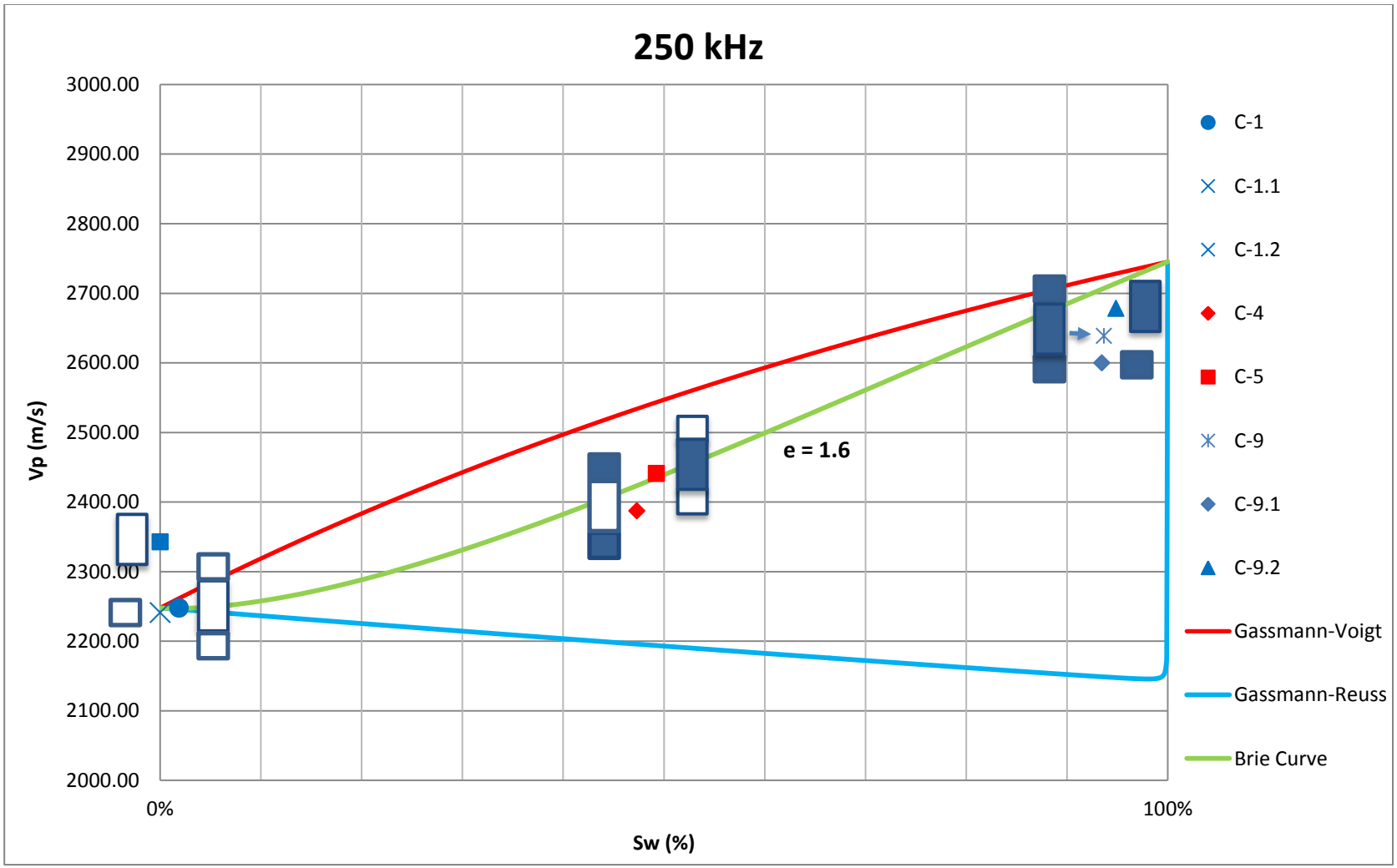

Figure 36. Experimental results for Vp versus Sw for 250 kHz and plotted against the predictions of Gassmann-Voigt-Reuss bounds and Brie's fluid mixing method using constant "e" equal to 1.6. The figures on plot in the format of blue and white blocks represent the different samples and their fluid distribution, which are draw in scale.

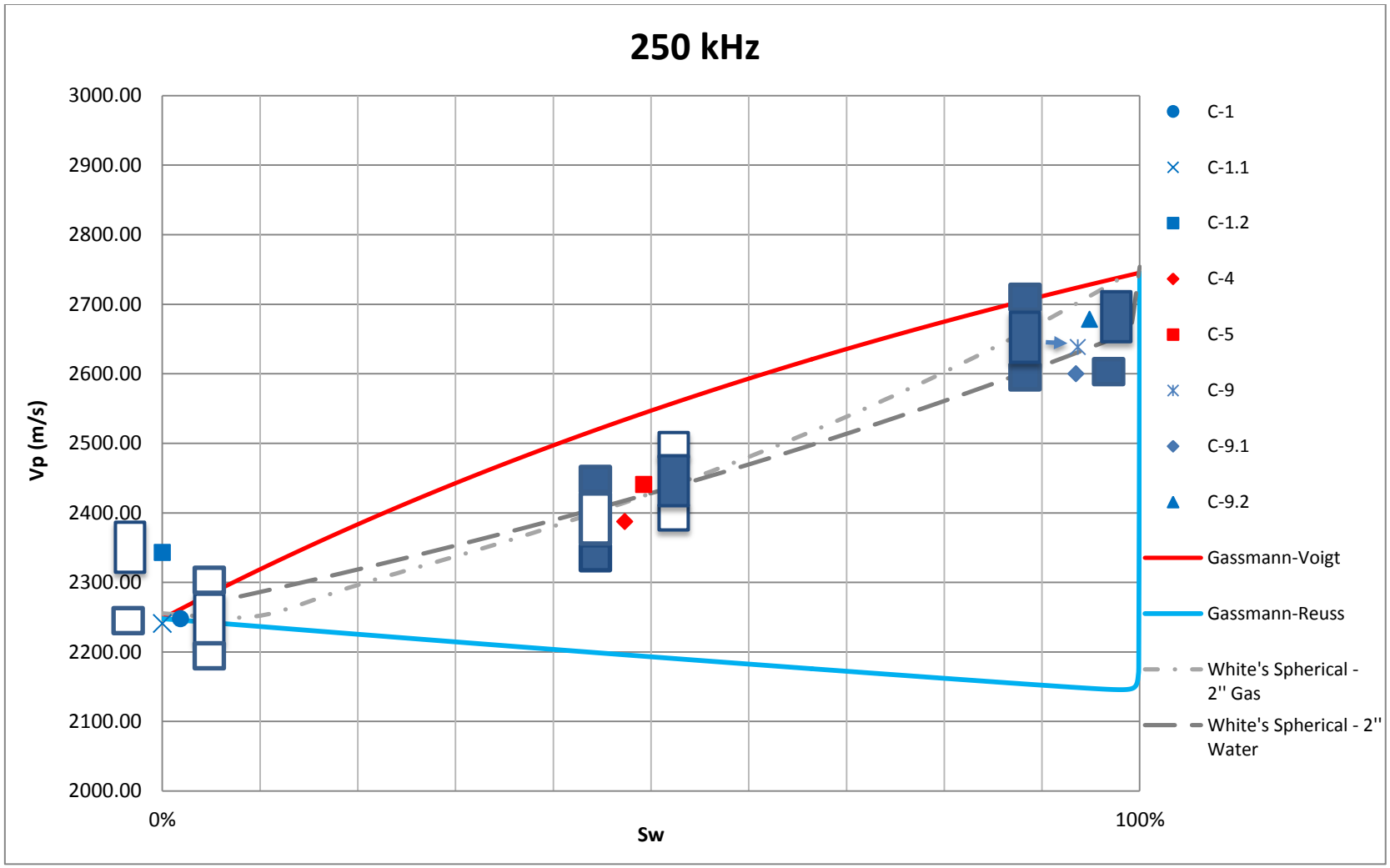

Figure 37. Experimental results for Vp versus Sw for 250 kHz and plotted against the predictions of Gassmann-Voigt-Reuss bounds and White's model for periodic concentric spherical patches. The figures on plot in the format of blue and white blocks represent the different samples and their fluid distribution, which are draw in scale.

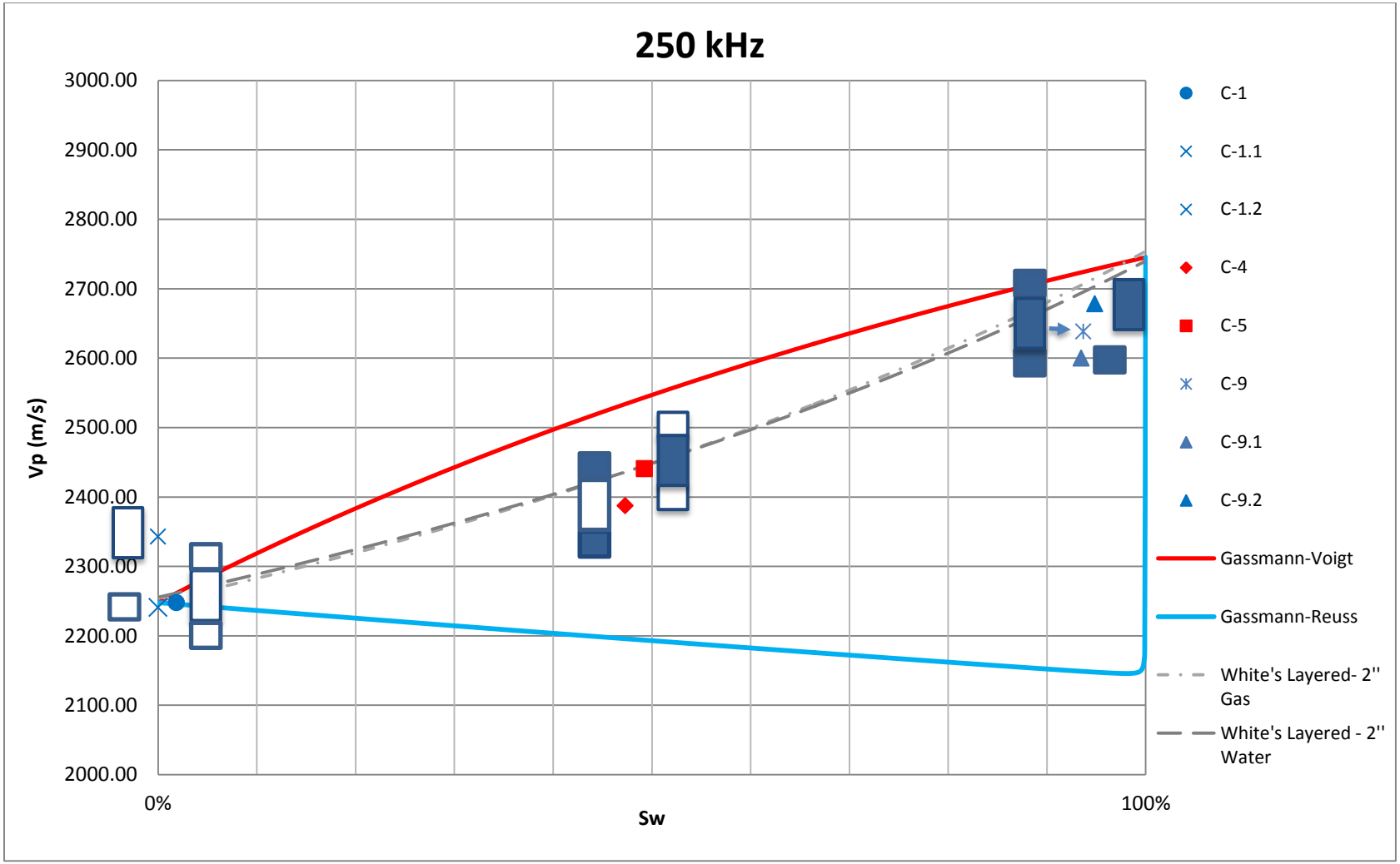

Figure 38. Experimental results for Vp versus Sw for 250 kHz and plotted against the predictions of Gassmann-Voigt-Reuss bounds and White et al. model for periodic layered patch. The figures on plot in the format of blue and white blocks represent the different samples and their fluid distribution, which are draw in scale.

Chapter 6

Discussion

As seen in Figure 32, there are 3 sizes of sample that were tested in this study, all having a cylindrical shape, the same diameter but different lengths. The three different lengths were 1, 2 and 4 inches. We tested these different sample lengths in order to assure that no surface wave was being measured instead of acoustic waves traveling through the body of the samples, which would lead to the measurement of very high speed P-waves and therefore would lead to huge errors during the interpretation and discussion of the data. Additionally, in order to double check that it is was not the case, we tested these three different sample lengths at both dry and fully water saturated conditions. If the results were similar and consistent between them, it was an indication that no surface wave was being measured. In fact, Figures 36 to 38 indicate that this is actually the case, as the different sample sizes produced consistent and similar P-wave velocities. Nevertheless, an exception was observed for the sample C-1.2, tested at 250 kHz, which presented values consistently higher than those observed for the samples C-1 and C-1.1, even if they had similar water saturations. As all samples had the same diameter and the velocities measured for the samples C-1 and C-1.1 were almost the same, the anomalously high Vp observed for the sample C-1.2 seems not to be justified by its length, but probably by an extremely dry C-1.2 sample. Such dry condition is known from the literature to produce significantly higher velocities when compared to samples at slightly "moist conditions" (Cadoret et al., 1993; Mavko et al., 2009; Murphy III, 1984, 1982). In fact, it was observed in the literature that the absorption of moisture could lead to velocity drops in the order of 4% (Cadoret et al., 1993), which is similar to what is observed when comparing the velocities of samples C-1, C-1.1

and C-1.2. Besides the fact that Table 5 indicates the same water saturation condition (0% Sw) for samples C-1.1 and C-1.2, it is likely that the absorption of moisture in C-1.1 produced such a small difference in terms of weight that the method used to measure water saturation was not able to identify any difference between these samples. In addition, the differences in Vp observed in Figures 36 to 38 between samples C-9, C-9.1 and C-9.2 seem to be caused by the different values of water saturation, as velocity is very sensitive to changes of saturation at that range of Sw.

Figure 32 shows that in this study we focused on three saturation levels, which were dry, partially saturated and fully water saturated. The reasons for testing the dry and fully water saturated conditions was to calibrate the fluid substitution models and at the same time attest if the velocities were within the Gassmann-Voigt-Reuss bounds, as at these saturation conditions one expects the bounds to be matched. Moreover, the uniformly saturated samples, represented by samples C-1, C-1.1, C-1.2, C-7, C-9, C-9.1, C-9.2, were expected to present a velocity behavior similar to the Gassmann-Reuss bound, as they do not present saturation heterogeneities larger than their Critical Length. In fact, for any given sample and for both wave frequencies (100 and 250 kHz), the Critical Length was always in the order of few millimeters. For example, for an ultrasonic test performed at 100 kHz in a rock with permeability of 300 mD and which fluid patches are saturated with air (bulk modulus of 0.000101 GPa, density of 1.291 kg/m^3, viscosity of 0.001695 Pa.sec.) the Lc would be equal to 0.013 millimeters (Lc equation presented in section 2.3.2). On the other hand, the patchy saturated samples, which therefore had saturation heterogeneities larger than the Critical Length, represented by samples C-2, C-3, C-4, C-5, C-6 and C-8, were aimed to test the predictions made by the patchy models and by the Gassmann-Voigt bound. In summary, Figure 32 presents both the samples expected to present a velocity behavior close to what Gassmann-Voigt bound and the patchy models predict (patchy saturation) as well as those expected to follow the Gassmann-Reuss bound (uniform saturation).

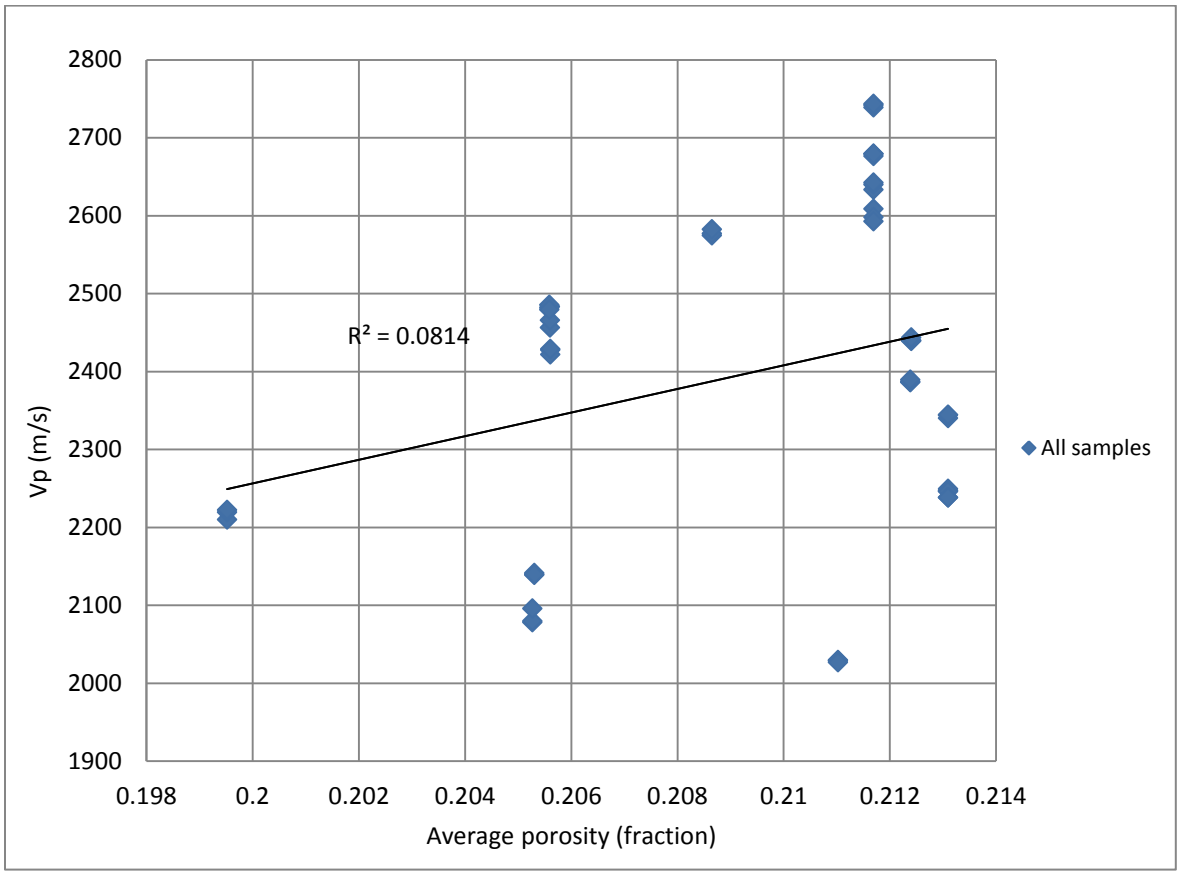

Figure 39. Vp versus average porosity for all samples investigated at 100 kHz and/or 250 kHz, demonstrating no correlation between these variables.

In order to verify whether the variations in the experimentally measured acoustic velocities were correlated to the fluctuations in the average porosity of the samples, Figure 39 was produced. In this figure, we present the compressional velocities measured at 100 kHz and 250 kHz versus the average porosity calculated for all samples. As seen in this plot, the R-squared correlation factor is equal to 0.08144 and, therefore, there is no correlation between these variables in this study. Moreover, the difference between the lowest and highest value of porosity is in the order of 6.7% and between the lowest and highest P-wave velocity this difference in porosity is around 35.4%. Hence, porosity is not driving the variations observed in terms of acoustic velocity. Furthermore, the difference in porosity value for the samples presenting the

highest and lowest P-wave velocity is of only 0.02%. Likewise, as it can be seen in the Appendix A, the pore size distribution of the core samples is very similar to each other. These results about porosity are important to be emphasized, as it is known from the literature that porosity changes can generate strong variations in wave speed. In fact, well logging techniques based on acoustic waves were initially used by the industry to estimate the porosity of the formations (Dewan, 1983).

The experimentally measured ultrasonic P-wave velocities and their standard deviation are reported in Tables 5 and 6 and are also presented in Figures 33 to 38 in conjunction with the Gassmann-Voigt-Reuss bounds, the velocity predictions made by the Brie mixing rule as well as by the different White's model. Figures 33 to 35 represent the experimental data and results obtained from the models for a wave frequency of 100 kHz. Figures 36 to 38 reflect the experimental and modeling results obtained for 250 kHz. Figure 33 and 36 present the empirical Brie's velocity versus water saturation curve using a cementation coefficient of 1.6 just in order to illustrate that it is possible to adequately fit the experimental data using this method. Therefore, an attempt to choose the optimal cementation coefficient for the experimental data using, for instance, an iterative algorithm, was not made in this study, as it is clear that by doing so it would always be possible to fit any experimental data point with accuracy. Brie's method is purely empirical, does not have assumptions, and can be an interesting approach when experimental data is vastly available, as the impact of possible measurement errors would be reduced and tend not to severely affect the predictions of the method. Nevertheless, the availability of prior and accurate experimental data is essential for the appropriate usage of this method in the field.

Figures 34 and 37 contains the experimental results, the Gassmann-Voigt-Reuss bounds, the velocity versus water saturation curves produced by the White's spherical model using different patch sizes and different assumptions of fluid saturating the patches (air or water). In Figure 34, we have four different velocity versus Sw curves, which represent two different patch

sizes (1 or 2 inches) and two different fluids in the patch (water or air). In Figure 37, we have two curves that represent a single patch size (2 inches) but two different fluids saturating the patch (water or air). Hence, Figures 34 and 37 consider all the patchy saturations created in laboratory for this work, which were:

- 2-inches patch saturated with water (Samples 2 and 5);
- 1-inch patch saturated with water (Sample 6);
- 2-inches patch saturated with air (Samples 3 and 4);
- 1-inch patch saturated with air (Samples 6 and 8).

By simply analyzing these two figures, it is not straightforward to infer about the performance of the White's layered model for predicting the velocity for the patchy saturated samples at different saturations. Nevertheless, it seems that at the frequency of 250 kHz the estimates of this model are closer to the experimentally observed velocities. However, at 250 kHz there were less patchy saturated samples being evaluated than at 100 kHz, in specific the samples 2 and 3. The same is also the case in Figures 35 and 38, where the White's layered model seems to better describe the velocity of patchy saturated samples at 250 kHz than at 100 kHz. Nonetheless, it is still difficult to analyze the discrepancies in performance by simply visualizing Figure 35 and Figure 38. Even more challenging is the task of visually inferring from these figures which of the Biot's based models achieves better results for the patchy fluid distributions recreated in laboratory. Therefore, without the usage of another analytical tool it is impractical to assess if patchy saturation conditions are better described by the Gassmann-Voigt bound, White's spherical or layered model. Therefore, further comparison between experimental and model generated data is required in order to shed light on the performance of these models. In order to do that, Table 7 and Figure 40 were created and are presented below.

Table 7. Difference in fraction between the compressional wave velocities predicted using Brie, White's layered and White's spherical model and the velocities measured experimentally.

	Compressional Velocity (m/sec)				Error (%)		
Sw (%)	**Gassmann -Voigt**	**White's (Spherical)**	**White's (Layers)**	**Experimental**	**Gassmann-Voigt vs. Experimental [%]**	**White's (Spherical) vs. Experimental [%]**	**White's (Layers) vs. Experimental [%]**
100 kHz - 1'' Gas patch							
49%	2521.51	2341.83	2407.34	2481.70	2%	-6%	-3%
49%	2521.51	2341.83	2407.34	2485.29	1%	-6%	-3%
49%	2521.51	2341.83	2407.34	2479.32	2%	-6%	-3%
73%	2630.22	2495.56	2542.98	2574.50	2%	-3%	-1%
73%	2630.22	2495.56	2542.98	2577.08	2%	-3%	-1%
73%	2630.22	2495.56	2542.98	2582.25	2%	-3%	-2%
100 kHz - 2'' Gas patch							
38%	2464.12	2329.01	2362.70	2141.38	15%	9%	10%
38%	2464.12	2329.01	2362.70	2138.72	15%	9%	10%
38%	2464.12	2329.01	2362.70	2139.60	15%	9%	10%
49%	2521.51	2382.22	2414.88	2427.69	4%	-2%	-1%
49%	2521.51	2382.22	2414.88	2421.97	4%	-2%	0%
49%	2521.51	2382.22	2414.88	2428.84	4%	-2%	-1%
100 kHz - 1'' Water patch							
49%	2521.51	2348.42	2408.37	2481.70	2%	-5%	-3%
49%	2521.51	2348.42	2408.37	2485.29	1%	-6%	-3%
49%	2521.51	2348.42	2408.37	2479.32	2%	-5%	-3%
100 kHz - 2'' Water patch							
37%	2458.63	2341.53	2362.17	2078.21	18%	13%	14%
37%	2458.63	2341.53	2362.17	2079.88	18%	13%	14%
37%	2458.63	2341.53	2362.17	2095.90	17%	12%	13%
49%	2521.51	2384.15	2415.65	2456.25	3%	-3%	-2%
49%	2521.51	2384.15	2415.65	2465.63	2%	-3%	-2%
49%	2521.51	2384.15	2415.65	2483.41	2%	-4%	-3%
250 kHz - 2'' Gas patch							
47%	2511.46	2413.42	2434.15	2387.01	5%	1%	2%
47%	2511.46	2413.42	2434.15	2385.90	5%	1%	2%
47%	2511.46	2413.42	2434.15	2389.25	5%	1%	2%
250 kHz - 2'' Water patch							
49%	2521.51	2401.00	2444.31	2438.90	3%	-2%	0%
49%	2521.51	2401.00	2444.31	2440.04	3%	-2%	0%
49%	2521.51	2401.00	2444.31	2443.46	3%	-2%	0%

Table 7 shows the P-wave velocities measured experimentally for the patchy samples as well as the velocities obtained from the Gassmann-Voigt, White's spherical model, White's layered model and the difference between these velocities. The difference between the experimental results and the predictions of the models was calculated accordingly to the equation that follows below. Figure 39 shows in the form of boxplots all the errors reported in Table 7.

$$Error\ (\%) = \left(\frac{Vp_{model} - Vp_{experiment}}{Vp_{experiment}}\right) * 100\%$$

Where:

$Error\ (\%)$ = error of the P-wave velocity predicted by the model in relation to experimentally measured velocities [%].

Vp_{model}= P-wave velocity predicted by the model [meter/second].

$Vp_{experiment}$= P-wave velocity measured experimentally [meter/second].

Table 7 details the error between the velocities predicted by the patchy models and the experimental measurements for both frequencies of 100 kHz and 250 kHz and, therefore, enables a global comparison of the error distribution for the different models. The results of Table 7, specifically the error distribution for each model, are presented in Figure 40 through boxplots. These boxplots are composed of the following elements:

- Blue boxes, which represent the interquartile range;
- Black lines, representing the error values between the 0.3^{th} and 25^{th} percentiles and the 75^{th} and 99.7^{th} percentiles;
- Red cross points, indicating data points below the 0.3^{th} percentile or above the 99.7^{th} percentile, also simply known as outliers.

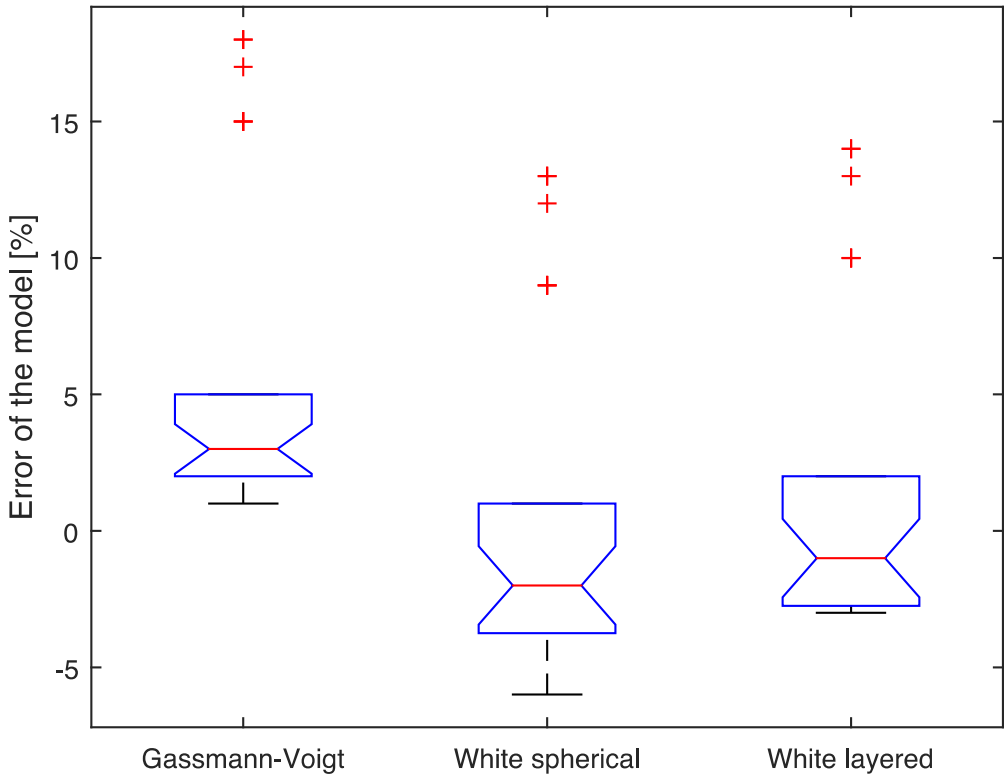

Figure 40. Boxplots of the deviation between the experimental data and the patchy models. The boxplots consider all the samples expected to behave as patchy saturated.

Figure 40 offers a better visualization tool that enables the comparison of the performance of the different patchy models. As it is possible to see, the Gassmann-Voigt bound presents the highest median error within the patchy models, which is positive and therefore shows a tendency for super estimating velocities. On the other hand, it presents the narrowest interquartile range, which only includes positive errors. In the case of the White's spherical model, the median error is negative and lower than for Gassmann's upper bound. Nevertheless, its shows an interquartile range that is significantly larger than Gassmann-Voigt's and which encompasses both positive and negative errors, besides an apparent predominance of negative values. Yet, White's layered model presents an even lower median error, which is negative and significantly closer to zero. The interquartile range is comparable to White's spherical model,

therefore, larger than for Gassmann-Voigt bound, and contains errors relatively well distributed between positive and negative errors. Besides the different error distributions, these models share a common point, which is the fact of having the same outliers. In this case, the outliers are related to the P-wave velocities predicted for Samples 2 and 3, which presented errors around or higher than 10% and thus were poorly described by all models. In fact, those samples seem to be well described by Gassmann's lower bound, or by the uniform saturation behavior. These samples have air present in some extent in all sections of the sample and, therefore, air and water might be mixed at scales smaller than Lc throughout the sample. Hence, there might be no high stiffness regions in the samples, making the distribution of stresses within the pore volume to be closer to a uniform situation. Therefore, the distributions of stresses would result in a saturated-rock bulk modulus that is dictated by the softer saturating fluid, as assumed in the analogy done by Reuss in relation to a system in series where the "conductivity", or the stiffness in this case, is mostly controlled by the least conductive component. Additionally, the layered and spherical patchy models of White consider only two types of regions to describe the distribution of fluids, which are completely wet or completely dry. This assumption is at the heart of these models and is used, for example, for the calculation of water saturation, which results in highly erroneous Sw estimations for the case of Samples 2 and 3.

Thus, it is possible to notice that for the experimental conditions of this study the spherical and layered models proposed by White perform better than the Gassmann's equation using the Voigt mixing rule. As mentioned previously in this work, Gassmann's relation is known to work best for very low frequency seismic data and high permeability rocks (Mavko et al., 2009; Schön, 2015), as at this conditions any wave induced pore pressure gradient would have enough time to flow and equilibrate throughout the medium, enabling an isostress condition within the pore space to be reached. Therefore, Gassmann is expected to perform less accurately as frequencies increase toward the ultrasonic bandwidth, as in our study. Gassmann's theory also

assumes that the rock has macroscopically homogeneous and isotropic mineral bulk moduli and pore space, where all pores are interconnected, implying that wavelength is much larger than the grain, pore size and other heterogeneities. Moreover, it assumes that the pores are filled with a single non-viscous/frictionless pore fluid, which does not interact with the rock frame. It also considers that the rock-fluid system itself is closed and that there is no relative movement between the rock frame and the saturating fluid when the rock is accelerated by a passing acoustic wave. These assumptions are important simplifications for many real rock-fluid systems and especially for our experimental set-up, as the wave frequency implemented here was many times higher than low frequency seismic waves.

On the other hand, the physical assumptions behind White's models, which are based on the Biot's theory of acoustic wave propagation in fluid saturated porous medium (Biot, 1962, 1956a, 1956b), are more realistic. Biot proposes a model that is more in accordance to our experimental set-up because it accounts for the viscosity of the fluids, assuming that the fluid is compressible and may flow/move relatively to the rock frame, causing viscous wave attenuation. Therefore, Biot considers viscous/inertial effects caused by the passage of an acoustic wave through a fluid saturated porous medium, which is important for patchy saturated samples tested at ultrasonic frequency. As discussed in the literature review, in the case of Biot's theory, velocity is also wave frequency dependent. For Biot's high frequency limit, the rock is intensively shaken/accelerated, resulting in the fluid lagging behind and moving completely decoupled from the rock frame. At this limit there is not enough time for pore pressures to equilibrate through fluid flow and the rock is at the "unrelaxed" state. Conversely, at the low frequency limit, the viscous skin is larger than average pore size and, therefore, fluid and rock frame are essentially moving in harmony, together. Additionally, at low frequency there is enough time for fluid to flow and dissipate pore pressure gradients, reaching an isostress condition and giving the velocity predictions also provided by the Gassmann's lower bound. Furthermore, Biot's theory considers

the porous rock frame to be homogeneous and isotropic, having uniform porosity, bulk modulus, shear modulus, density and permeability, therefore implying that the relative movement between fluid and rock frame is controlled by the rock's permeability (Darcy's law) and occurs globally in the porous medium. As Gassmann, Biot considers the presence of only a single fluid saturating the rock. This theory also assumes that the acoustic wavelength is much larger than the pore size, grains or other heterogeneities. White's spherical and layered models received important corrections from Dutta and Seriff (1979) and Norris (1993), respectively, were the first to expand Biot's theory to the case of mesoscopic distribution of fluids, which are considered as fluid heterogeneities much larger than the pore scale but much smaller than the passing wavelength. Both White's models calculate a frequency-dependent complex P-wave modulus by considering the ratio of the imposed pressure amplitude to the related fractional volume change, including fluid flow from the patches to the surroundings.

Table 8. Wavelengths measured for the different samples and wave frequencies.

Sample Characteristics	**Experimental velocity (m/s)**	**Wavelength (mm)**
Sample	**P-wave**	**P-wave**
Wave frequency: 250 kHz		
C-1.1	2240.80	9.0
C-1.2	2342.88	9.4
C-1	2247.83	9.0
C-4	2387.39	9.5
C-5	2440.80	9.8
C-9.1	2599.75	10.4
C-9.2	2678.20	10.7
C-9	2638.47	10.6
Wave frequency: 100 kHz		
C-1	2217.21	22.2
C-2	2084.66	20.8
C-3	2139.90	21.4
C-4	2426.17	24.3
C-5	2468.43	24.7
C-6	2482.11	24.8
C-7	2028.46	20.3
C-8	2577.94	25.8
C-9	2741.26	27.4

The assumptions behind the Biot's theory and the patchy models of White are reasonably acceptable for the experiments performed in this study, with exception to the assumption regarding the wavelength scale. For our experiments the saturation heterogeneities were always much larger than the pore scale and critical relaxation length (Lc), but were approximately equal to the wavelength or slightly larger than it. The wavelength is given by the ratio of wave velocity to wave frequency and, therefore, using the data from Tables 5 and 6 we calculated that in this work the range of wavelengths was approximately between 9 mm (0.4 inch) to 28 mm (1.1 inches), as demonstrated in Table 8 above. As the size of the patches was about 25.4 mm (1 inch) or 50.8 mm (2 inches), the acoustic experiments were performed within a grey zone, where wavelength and patch size are not exactly the same but have the same order of magnitude.

Furthermore, as mentioned in the methodology (section 4.1.5), during the analysis of the experimental data, it was observed that for the cases studied in this work, it was possible to estimate the P-wave velocity for any partial saturation based on an average velocity, named previously in this work as "Average Vp", calculated on the base of concepts borrowed from seismology. This method only requires as inputs the velocities measured at the dry and wet conditions. In fact, only the velocity at the dry condition would be sufficient, as Gassmann's could be used to estimate the wet condition velocity. The average velocity is calculated considering that the heterogeneities are much larger than the wavelength (Aki and Richards, 2009), meaning that the acoustic response of the medium to a passing wave is given by the individual contribution of each section of the medium, without interactions between them. In addition, it assumes that the heterogeneities are presented as layers; therefore, this method might not work as well for other geometries. Instead of presenting two plots containing the experimental data versus the velocity curves obtained from this method, we present Figure 41 in order to illustrate the behavior of its curves. Figure 41 has an example of Vp versus water saturation curve

in conjunction with the Gassmann-Voigt-Reuss bounds. The velocities used as inputs for the calculation of this average Vp curve were the ones observed for samples C-1 and C-9 at 100 kHz. Notice that the average Vp curve crosses the Gassmann-Voigt bound at high saturation values, as the velocity measured from sample C-9 was slightly higher than the one predicted by Gassmann-Voigt. Moreover, sample C-9 was at 95% water saturation. Nevertheless, this could be avoided by using Gassmann's equation and the velocity at the dry condition to infer the velocity at 100% water saturation.

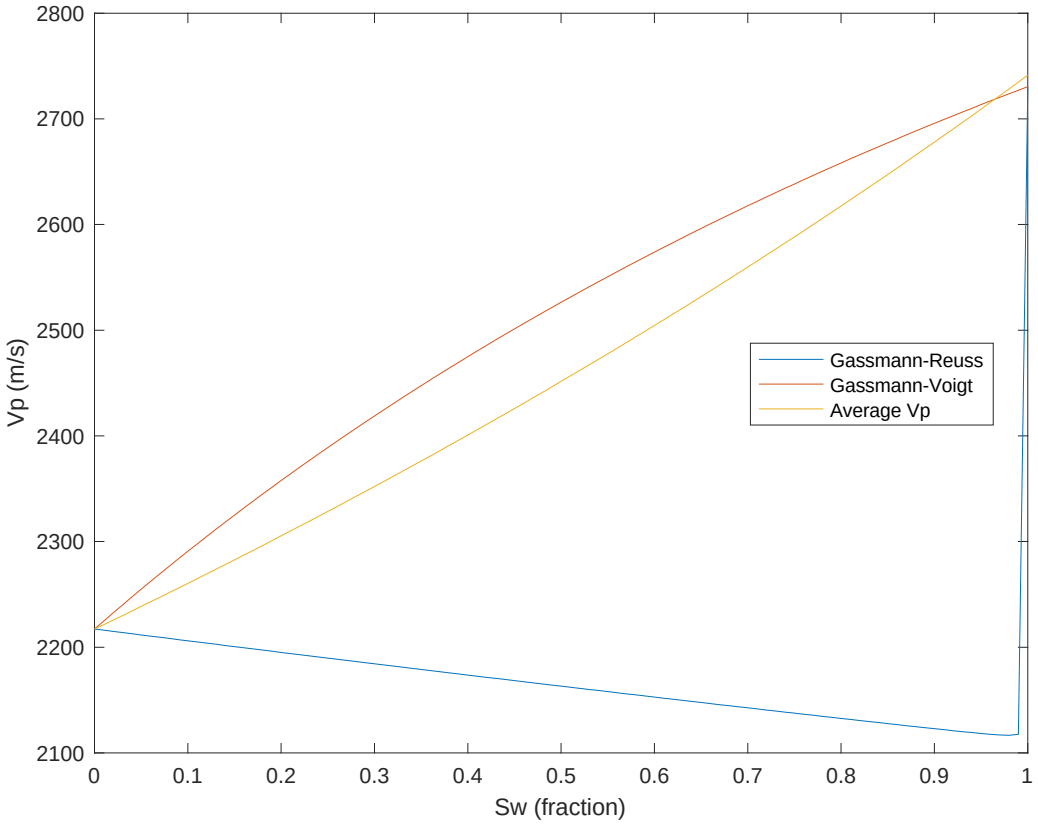

Figure 41. Example of average Vp versus water saturation and compared to the Gassmann-Voigt-Reuss bounds.

Table 9. Input data for the average P-wave velocity and a comparison with the P-wave velocity measured experimentally. This table considers all samples expected to behave as patchy saturated.

	Sample Characteristics		Velocities		Error (%)
Sw (%)	**Vp wet (m/s)**	**Vp dry (m/s)**	**Average Vp (m/s)**	**Experimental Vp (m/s)**	**Average Vp vs. Experimental Vp (%)**
100 kHz - 1'' Gas patch					
49%	2741.26	2217.21	2444.295263	2481.70	-2%
49%	2741.26	2217.21	2444.295263	2485.29	-2%
49%	2741.26	2217.21	2444.295263	2479.32	-1%
73%	2741.26	2217.21	2574.948948	2574.50	0%
73%	2741.26	2217.21	2574.948948	2577.08	0%
73%	2741.26	2217.21	2574.948948	2582.25	0%
100 kHz - 2'' Gas patch					
38%	2741.26	2217.21	2388.577179	2141.38	12%
38%	2741.26	2217.21	2388.577179	2138.72	12%
38%	2741.26	2217.21	2388.577179	2139.60	12%
49%	2741.26	2217.21	2445.123124	2427.69	1%
49%	2741.26	2217.21	2445.123124	2421.97	1%
49%	2741.26	2217.21	2445.123124	2428.84	1%
100 kHz - 1'' Water patch					
49%	2741.26	2217.21	2444.295263	2481.70	-2%
49%	2741.26	2217.21	2444.295263	2485.29	-2%
49%	2741.26	2217.21	2444.295263	2479.32	-1%
100 kHz - 2'' Water patch					
37%	2741.26	2217.21	2384.701564	2078.21	15%
37%	2741.26	2217.21	2384.701564	2079.88	15%
37%	2741.26	2217.21	2384.701564	2095.90	14%
49%	2741.26	2217.21	2446.662717	2456.25	0%
49%	2741.26	2217.21	2446.662717	2465.63	-1%
49%	2741.26	2217.21	2446.662717	2483.41	-1%
250 kHz - 2'' Gas patch					
47%	2638.47	2247.83	2417.144494	2387.01	1%
47%	2638.47	2247.83	2417.144494	2385.90	1%
47%	2638.47	2247.83	2417.144494	2389.25	1%
250 kHz - 2'' Water patch					
49%	2638.47	2247.83	2424.606575	2438.90	-1%
49%	2638.47	2247.83	2424.606575	2440.04	-1%
49%	2638.47	2247.83	2424.606575	2443.46	-1%

Table 9 presents the input data, predictions and errors associated with the Average Vp methodology. The velocities measured for samples C-1 and C-9, at both 100 and 250 kHz, were used as the references of velocities for the dry and fully water saturated conditions, respectively. Figure 42 shows in the form of boxplots the errors associated with the average Vp in conjunction with the errors presented in Figure 40 for the other models.

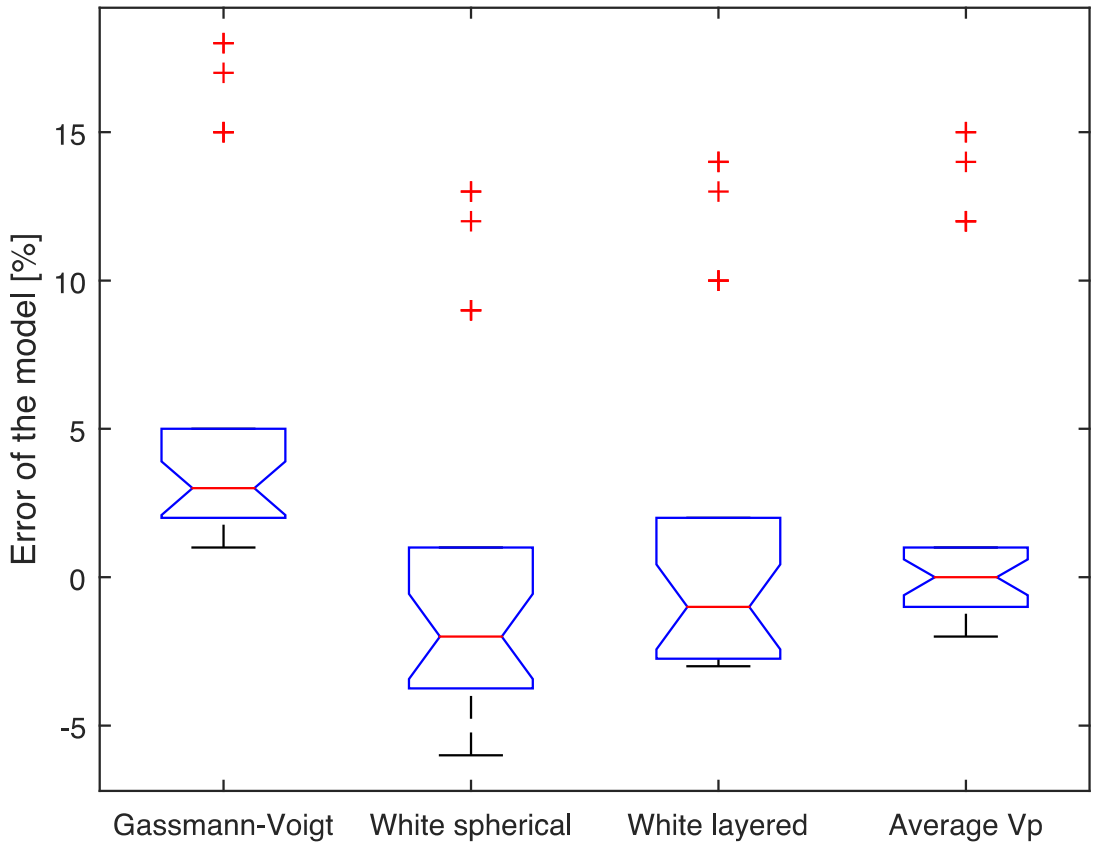

Figure 42. Boxplots of the difference between the experimental P-wave velocities and the predictions of the patchy models and of the average Vp. The boxplots consider all the samples expected to behave as patchy saturated.

As Figure 42 shows, this average Vp performs better than Gassmann-Voigt, White's spherical and layered models, as the median error is close to zero and the interquartile range is narrower and uniformly distributed around the median. It also indicates that the geometry of the fluid distribution can be important, as the layered models presented the better results. This contradicts the findings of Dutta and Seriff (1979). Figure 41 shows that the curves for this average Vp versus water saturation have a behavior similar to the predictions made by White et al. for layered patchy saturations. The average velocity method is simpler to implement, as it does not require specific information about the sample other than the velocities at the dry and wet conditions. For instance, Gassmann requires Vp and Vs at dry condition, data on rock porosity and information about the density, bulk moduli and shear moduli of the rock frame and fluids. White's models require the same inputs as Gassmann's and also information on wave frequency, rock permeability, viscosity of the fluids and dimension of the patches. Density and moduli of fluids and rock frame are relatively easy and accurate to infer from the literature, but permeability, porosity and dimension of the fluid patches are sample-specific and thus require experimental investigation. Considering all the discussions made in this chapter and giving special attention to the performance of the models in terms of error distribution, we could suggest the following ranking for the effectiveness of the models in matching the experimental data of this study:

1st: Average Vp;

2nd: White's layered model;

3rd: White's spherical model;

4th: Gassmann-Voigt bound.

Chapter 7

Conclusions

The experimental methodology applied in this work was able to reproduce layered patchy saturation conditions that could be tested at the ultrasonic frequency, thus enabling the analysis of the performance of different patchy models at predicting the relationship between acoustic wave velocity, water saturation and saturation distribution. The analysis and comparison of the outputs of the models with the experimental data indicates that Biot's theory seems to be a better theoretical base for modeling patchy saturations, as White (1975) spherical model (-2% median error) and White et al. (1975) layered model (-1% median error) performed better than Gassmann's upper bound (3% median error). A velocity estimation method based on concepts borrowed from seismology, which averages the velocities obtained experimentally at dry and wet conditions, was also investigated. This method was demonstrated to be very effective at predicting velocities for the partial saturation conditions of this work (0% median error), even if its derivation assumes wavelengths much smaller than the heterogeneities of the medium. Nevertheless, all models showed satisfactory performance, as they showed satisfactory agreement with the laboratory data, even if some underlying assumptions of the models were not fully satisfied by the experimental conditions, especially regarding the ratio of patch size to wavelength. In this work, there were patch sizes slightly smaller or equal to the wavelength scale; the patchy models assume wavelengths much larger than the patch size. Moreover, the patchy samples that had layers partially water saturated (Samples C-2 and C-3), performed similarly to the predictions made with Gassmann-Reuss lower bound, indicating that, at this conditions, we might have the fluids mixed at a scale smaller than the critical relaxation length and, therefore, the distribution of pore pressures results in a system where the changes in stiffness are dictated predominantly by the least rigid fluid. From the results and discussions, we conclude that fluid

substitution simulations could profit from the usage of more complex patchy models, such as those proposed by White (1975) and White et al (1975), as they use concepts that are more realistic and could give more insights about the pore fluid distribution. Moreover, their predictions seem to be more accurate than the Gassmann's upper bound.

Chapter 8

Future Prospects

Besides the conclusions of this work, it would be important to consolidate them by performing additional experiments for different patchy and uniform saturations. Furthermore, the experimental methodology of this work could be enhanced and include more parameters, such as confining and pore fluid pressure. It would also be interesting to use this improved experimental setup to investigate the performance of these models at other wave frequencies, such as the ones used in chirp seismic surveys. Based on future experimental data, combined with the observations reported here, it could be possible to suggest refinements to empirical or theoretical models for different configurations of patchy saturation. Finally, this and following works might contribute for the reduction of uncertainty in fluid substitution simulations and interpretation of seismic field data and well logs.

References

Adler, P.M., 1992. Porous media: geometry and transports, Butterworth-Heinemann series in chemical engineering. Butterworth-Heinemann, Boston.

Aki, K., Richards, P.G., 2009. Quantitative seismology. University Science Books, Mill Valley, CA.

Arcone, S. a., 2002. Stratigraphic profiling with ground-penetrating radar in permafrost: A review of possible analogs for Mars. J. Geophys. Res. 107, 1–14. doi:10.1029/2002JE001906

Bahadori, A., Zeidani, K., 2012. Predicting scale formation in wasterwater disposal wells of crude-oil desalting plants. Pet. Coal 54, 143–148.

Benson, S., Cook, P., 2005. IPCC Special Report on Carbon dioxie Capture and Storage. IPCC chapter 5, 196–276.

Benson, S.M., 1980. Carbon Dioxide Capture and Storage in Underground Geologic Formations, in: Benson, S.M. (Ed.), The 10-50 Solution: Technologies and Policies for a Low-Carbon Future. The Pew Center on Global Climate Change and the National Commission on Energy Policy, Berkeley, pp. 1–19.

Berryman, J.G., 1999. Origin of Gassmann's equations. Geophysics 64, 1627. doi:10.1190/1.1444667

Berryman, J.G., Milton, G.W., 1991. Exact results for generalized Gassmann's equation in composite porous media with two constituents. Geophysics 56, 1950–1960. doi:10.1017/CBO9781107415324.004

Best, A.I., 1992. The prediction of the reservoir properties of sedimentary rocks from seismic measurements. The University Whiteknights Reading.

Best, A.I., Tuffin, M.D.J., Dix, J.K., Bull, J.M., 2004. Tidal height and frequency dependence of acoustic velocity and attenuation in shallow gassy marine sediments. J. Geophys. Res. B Solid Earth 109, 1–17. doi:10.1029/2003JB002748

Bhandari, A., Surampalli, R.Y., Champagne, P., Ong, S.K., Tyagi, R.D., Lo, I.M.C., 2007. Remediation Technologies for Soils and Groundwater, American Society of Civil Engineers (ASCE). American Society of Civil Engineers (ASCE).

Biot, M. a, 1962. Mechanics of Deformation and Acoustic Propagation in Porous Media. J. Appl. Physiscs 33, 1482–1498. doi:10.1063/1.1728759

Biot, M.A., 1956a. Theory of Propagation of Elastic Waves in a Fluid-Saturated Porous Solid. I. Low-Frequency Range. J. Acoust. Soc. Am. 28, 168. doi:10.1121/1.1908239

Biot, M.A., 1956b. Theory of Propagation of Elastic Waves in a Fluid-Saturated Porous Solid. II. Higher Frequency Range. J. Acoust. Soc. Am. 28, 179–191.

Bond, C.E., Gibbs, A.D., Shipton, Z.K., Jones, S., 2007. What do you think this is? "Conceptual uncertainty" In geoscience interpretation. GSA Today 17, 4–10. doi:10.1130/GSAT01711A.1

Brie, a, Pampuri, F., Marsala, A., Meazza, O., 1995. Shear sonic interpretation in gas-bearing sands. SPE Annu. Tech. Conf. Exhib. 701–710. doi:10.2118/30595-MS

Cadoret, T., Marion, D., 1995. Influence of frequency and fluid distribution on elastic wave velocities in partially saturated limestones. J. Geophys. Res. 100, 9789–9803. doi:0148-0227/95/95 JB-00757505.00

Cadoret, T., Mavko, G., Zinszner, B., 1998. Fluid distribution effect on sonic attenuation in partially saturated limestones. Geophysics 63, 154. doi:10.1190/1.1444308

Cadoret, T., Poirier, J.-P., Zinszner, B., 1993. Effet de la saturation eau-gaz sur les propriétés acoustiques des roches. Etude aux fréquences sonores et ultrasonores. University of Paris, VII.

Carcione, J.M., Helle, H.B., Pham, N.H., 2003. White's model for wave propagation in partially saturated rocks: Comparison with poroelastic numerical experiments. Geophysics 68, 1389. doi:10.1190/1.1598132

Carcione, J.M., Picotti, S., 2006. P-wave seismic attenuation by slow-wave diffusion: Effects of inhomogeneous rock properties. Geophysics 71, O1–O8. doi:10.1190/1.2194512

Caspari, E., Müller, T.M., Gurevich, B., 2011. Time-lapse sonic logs reveal patchy CO2 saturation in-situ. Geophys. Res. Lett. 38, 18–21. doi:10.1029/2011GL046959

Cheeke, J.D.N., 2012. Fundamentals and Applications of Ultrasonic Waves, Second Edi. ed. CRC Press - Taylor & Francis Group, Boca Raton, FL.

Clark, V. a, Tittmann, B.R., Spencer, T.W., 1980. Effect of volatiles on attenuation and velocity in sedimentary rocks. J. Geophys. Res. 85, 5190–5198. doi:10.1029/JB085iB10p05190

Darcy, H., 1856. Les fontaines publiques de la ville de Dijon: Exposition et application des principes a suivre et des formules a employer dans les questions de distribution d'eau; ouvrage terminé par un appendice relatif aux fournitures d'eau de plusieurs villes au filt. Libraire des Corps imperiaux des ponts et chaussées et des mines, Victor Dalmont, Paris.

Deb, P.K., 2014. An Introduction to Mine Hydrogeology, First Edit. ed. Springer Science+Business Media, New York. doi:10.1007/978-3-319-02988-7

Dewan, J.T., 1983. Essentials of modern open-hole log interpretation. PennWell Books, Tulsa, Oklahoma.

Dewar, J., 2001. Rock Physics for the rest of us - An informal discussion. CSEG Rec. 42–49.

Diallo, M.S., Prasad, M., Appel, E., 2003. Comparison between experimental results and theoretical predictions for P-wave velocity and attenuation at ultrasonic frequency. Wave Motion 37, 1–16. doi:10.1016/S0165-2125(02)00018-5

Domenico, S.N., 1976. Effect of Brine-Gas Mixture on Velocity in an Unconsolidated Sand Reservoir. Geophysics 41, 882. doi:10.1190/1.1440670

Dutta, N., Seriff, A., 1979. On White's model of attenuation in rocks with partial gas saturation. Geophysics. doi:10.1190/1.1440940

Ertekin, T., Abou-Kassem, J.H., King, G.R., 2001. Basic applied reservoir simulation, 1st ed. Society of Petroleum Engineers, Richardson, Tex.

Fallis, A.., 2013. Petroleum Geoscience: From Sedimentary Environments to Rock Physics, Journal of Chemical Information and Modeling. doi:10.1017/CBO9781107415324.004

Fanchi, J.R., 2006. Principles of Applied Reservoir Simulation, 3rd ed. Gulf Professional Pub, Boston.

Gadallah, M.R., Fisher, R., 2013. Exploration Geophysics, Journal of Chemical Information and Modeling. doi:10.1017/CBO9781107415324.004

Gassiyev, A., 2008. Mixing Models and Frame Moduli Bounds In Complex Lithologies. University of Houston.

Gassmann, F., 1951. Über die elastizität poröser medien. Vierteljahrsschrift der Naturforschenden Gesellschaft Zürich 1–23.

Gelinsky, S., Shapiro, S.A., 1997. Dynamic-equivalent medium approach for thinly layered saturated sediments. Geophys. J. Int. 128, F1–F4. doi:10.1111/j.1365-246X.1997.tb04086.x

Gurevich, B., Lopatnikov, S.L., 1995. Velocity and Attenuation of Elastic-Waves in Finely Layered Porous Rocks. Geophys. J. Int. 121, 933–947. doi:10.1111/j.1365-246X.1995.tb06449.x

Gurevich, B., Zyrianov, V.B., Lopatnikov, S.L., 1997. Seismic attenuation in finely layered porous rocks: Effect of fluid flow and scattering. Geophysics 62, 319–324.

Han, D., Nur, A., Morgan, D., 1986. Effects of porosity and clay content on wave velocities in sandstones. Geophysics 51, 14.

Hartley, K.B., 1981. Factors Affecting Sandstone Acoustic Compressional Velocities and an Examination of Empirical Correlations between Velocities and Porosities. SPWLA Twenty-Second Annu. Logging Symp. doi:10.1017/CBO9781107415324.004

Hashin, Z., Shtrikman, S., 1963. A variational approach to the theory of the elastic behaviour of multiphase materials. J. Mech. Phys. Solids 11, 127–140. doi:10.1016/0022-5096(63)90060-7

Johnson, D.L., 2001. Theory of frequency dependent acoustics in patchy-saturated porous media. J. Acoust. Soc. Am. 110, 682. doi:10.1121/1.1381021

Karpyn, Z.T., Piri, M., Singh, G., 2010. Experimental investigation of trapped oil clusters in a water-wet bead pack using X-ray microtomography. Water Resour. Res. 46, 1–25. doi:10.1029/2008WR007539

King, M.S., 2009. Recent developments in seismic rock physics. Int. J. Rock Mech. Min. Sci. 46, 1341–1348. doi:10.1016/j.ijrmms.2009.04.008

King, M.S., 1966. Wave velocities in rocks as a function of changes in overburden pressure and pore fluid saturants. Geophysics 31, 50–73.

Klinkenberg, L.J., 1941. The Permeabiliity Of Porous Media To Liquids And Gases. API Drill. Prod. Pract. 200–2013. doi:10.5510/OGP20120200114

Knight, R., Nolen-hoeksema, R., 1990. A Laboratory Study of the Dependence of Elastic Wave Velocities on Pore Scale Fluid Distribution. Geophys. Res. Lett.

17, 1529–1532.

Le Ravalec, M., Guéguen, Y., Chelidze, T., 1996. Elastic wave velocities in partially saturated rocks: Saturation hysteresis. J. Geophys. Res. 101, 837. doi:10.1029/95JB02879

Lebedev, M., Toms-Stewart, J., Clennell, B., Pervukhina, M., Shulakova, V., Paterson, L., Müller, T.M., Gurevich, B., Wenzlau, F., 2009. Direct laboratory observation of patchy saturation and its effects on ultrasonic velocities. Lead. Edge 28, 24. doi:10.1190/1.3064142

Lehr, J.H., 2002. Handbook of Complex Environmental Remediation Problems. McGraw-Hill, New York.

Lei, X., Xue, Z., 2009. Ultrasonic velocity and attenuation during CO2 injection into water-saturated porous sandstone: Measurements using difference seismic tomography. Phys. Earth Planet. Inter. 176, 224–234. doi:10.1016/j.pepi.2009.06.001

Liu, Z., Rector, J., Nihei, K., Tomutsa, L., Myer, L., Nakagawa, S., 2002. Extensional wave attenuation and velocity in partially-saturated sand in the sonic frequency range. doi:10.1190/1.1816479

Marion, D., Nur, A., 1991. Pore-filling material and its effect on velocity in rocks. Geophysics 56, 225–230.

Marion, D., Nur, A., Yin, H., Han, D., 1992. Compressional velocity and porosity in sand-clay mixtures. Geophysics 57, 554–563. doi:10.1190/1.1443269

Marion, D.P., 1990. Acoustical, Mechanical, And Transport Properties Of

Sediments And Granular Materials. Stanford Rockphysics Boreh. Geophys. Proj. Stanford University.

Mavko, G., Jizba, D., 1991. Estimating grain-scale fluid effect on velocity dispersion in rocks. Geophysics 56, 1940–1949.

Mavko, G., Mukerji, T., 1998. Bounds on low-frequency seismic velocities in partially saturated rocks. Geophysics. doi:10.1190/1.1444402

Mavko, G., Mukerji, T., Dovorkin, J., 2009. The Rock Physics Handbook - Tools for Seismic Analysis of Porous Media, 2nd ed. Cambridge University Press, New York. doi:10.1017/CBO9780511626753

Mavko, G., Nolen-Hoeksema, R., 1994. Estimating seismic velocities at ultrasonic frequencies in partially saturated rocks. Geophysics 59, 252. doi:10.1190/1.1443587

Monsen, K., Johnstad, S.E., 2005. Improved understanding of velocity – saturation relationships using 4D computer-tomography acoustic measurements. Geophys. Prospect. 53, 173–181.

Morgan, E., Vanneste, M., Vardy, M., 2014. Characterization of the Slope-destabilizing Effects of Gas-charged Sediment via Seismic Surveys, in: 2014 Offshore Technology Conference. Offshore Technology Conference, Houston, p. 11.

Morgan, E.C., Vanneste, M., Lecomte, I., Baise, L.G., Longva, O., McAdoo, B., 2012. Estimation of free gas saturation from seismic reflection surveys by the genetic algorithm inversion of a P-wave attenuation model. Geophysics 77, R175. doi:10.1190/geo2011-0291.1

Mukerji, T., Mavko, G., Mujica, D., Lucet, N., 1995. Scale-dependent seismic velocity in heterogeneous media. Geophysics 60, 1222–1233.

Müller, T., Gurevich, B., 2005. One-dimensional random patchy saturation model for velocity and attenuation in porous rocks. SEG Tech. Progr. Expand. Abstr. 2005 69, 1747–1750. doi:doi:10.1190/1.2148037

Müller, T.M., Gurevich, B., Lebedev, M., 2010. Seismic wave attenuation and dispersion resulting from wave-induced flow in porous rocks — A review. Geophysics 75, 75A147. doi:10.1190/1.3463417

Murphy III, W.F., 1984. Acoustic measures of partial gas saturation in tight sandstones. J Geophys Res 89 , 11549–11559. doi:10.1029/JB089iB13p11549

Murphy III, W.F., 1982. Effects of microstructure and pore fluids on the acoustic properties of granular sedimentary materials. Stanford University.

Murphy III, W.F., Winkler, K.W., Kleinberg, R.L., 1984. Frame modulus reduction in sedimentary rocks: the effect of adsorption on grain contacts. Geophys. Res. Lett. 1, 805–808. doi:10.1029/GL011i009p00805

Murphy, W.M., 1983. Effects of partial water saturation on attenuation in Massillon sandstone and Vycor porous glass. J. Acoust. Soc. Am. 71, 1458–1486.

Nace, R.L., 1971. Scientific framework of world water balance, International Hydrological Decade. UNESCO, Paris.

Naftz, D.L., Davis, J.A., 1999. Deep Aquifer Remediation Tools (DARTs): A new technology for ground-water remediation. USGS Fact Sheet 156-99.

Norris, A.N., 1993. Low-frequency dispersion and attenuation in partially saturated rocks. J. Acoust. Soc. Am. 94, 359–370.

Pehme, P.E., 2009. Groundwater Geophysics: A Tool for Hydrogeology, Second Edi. ed, Environmental and Engineering Geoscience. Springer-Verlag berling Heidelberg, Berlin. doi:10.2113/gseegeosci.17.1.96

Pride, S.R., Berryman, J.G., Harris, J.M., 2004. Seismic attenuation due to wave-induced flow. J. Geophys. Res. 109, 1–19. doi:10.1029/2003JB002639

Raymer, L.L., Hunt, E.R., Gardner, J.S., 1980. An Improved Sonic Transit Time-to-Porosity Transform. SPWLA Annu. Logging Symp. 1–13.

Reuss, A., 1929. Berechnung der Fließgrenze von Mischkristallen auf Grund der Plastizitätsbedingung für Einkristalle. ZAMM - Zeitschrift für Angew. Math. und Mech. 9, 49–58. doi:10.1002/zamm.19290090104

Rodriguez, L., Vives, L., Gomez, A., 2013. Conceptual and numerical modeling approach of the Guarani Aquifer System. Hydrol. Earth Syst. Sci. 17, 295–314. doi:10.5194/hess-17-295-2013

Røgen, B., Fabricius, I.L., Japsen, P., Høier, C., Mavko, G., Pedersen, J.M., 2005. Ultrasonic velocities of North Sea chalk samples: Influence of porosity fluid content and texture. Geophys. Prospect. 53, 481–496. doi:10.1111/j.1365-2478.2005.00485.x

Rossing, T.D., Schroeder, M.R., Hartmann, W.M., Fletcher, N.H., Dunn, F., Campbell, D.M., 2012. Springer Handbook of Acoustics, Rossing. Springer Science+Business Media, New York. doi:10.1007/s13398-014-0173-7.2

Schön, J.H., 2015. Physical Properties of Rocks: Fundamentals and Principles of Petrophysics (2nd edition). Dev. Pet. Sci. 65, 499. doi:10.1017/CBO9781107415324.004

Shaffer, G., 2010. Long-term effectiveness and consequences of carbon dioxide sequestration. Nat. Geosci. 3, 464–467. doi:10.1038/ngeo896

Shapiro, S. a, Muller, T.M., 1999. Seismic signatures of permeability in heterogeneous porous media. Geophysics 64, 99–103.

Shean, D.E., Marchant, D.R., 2010. Seismic and GPR surveys of Mullins Glacier, mcmurdo dry valleys, Antarctica: Ice thickness, internal structure and implications for surface ridge formation. J. Glaciol. 56, 48–64. doi:10.3189/002214310791190901

Takahashi, A.T., Mourão, M.A.A., 2012. Sistema Aquífero Guarani nos Estados de São Paulo, Mato Grosso do Sul e Paraná - Bacia Sedimentar do Paraná. Relatório Diagnóstico - RIMAS - CPRM 15.

Toms-Stewart, J., Mueller, T.M., Gurevich, B., Paterson, L., 2009. Statistical characterization of gas-patch distributions in partially saturated rocks. Geophysics 74, WA51–WA64. doi:10.1190/1.3073007

Toms, J., M, T.M., Gurevich, B., 2007. Seismic attenuation in porous rocks with random patchy saturation 2. Geophys. Prospect. 55, 671–678.

Toms, J., Mu, T.M., Ciz, R., Gurevich, B., 2006. Comparative review of theoretical models for elastic wave attenuation and dispersion in partially saturated rocks. Soil Dyn. Earthq. Eng. 26, 548–565. doi:10.1016/j.soildyn.2006.01.008

Tutuncu, A.N., Sharma, M.M., 1992. The influence of fluids on grain contact stiffness and frame moduli in sedimentary rocks. Geophysics 57, 1571–1582. doi:10.1190/1.1443225

Vanneste, M., Forsberg, C.F., Knudsen, S., Kvalstad, T.J., L 'heureux, J.-S., Lunne, T., Vardy, M.E., Chand, S., Longva, O., Morgan, E., Kopf, A., Mörz, T., Steiner, A., Brendryen, J., Haflidason, H., 2015. Integration of very-high-resolution seismic and CPTU data from a coastal area affected by shallow landsliding – the Finneidfjord natural laboratory. Int. Cent. Geohazards.

Voigt, W., 1910. Lehrbuch der Kristallphysik. B.G. Teubner, Leipzig.

Wang, Z., 2000. The Gassmann equation revisited: comparing laboratory data with Gassmann's predictions, in: Wang, Z., Nur, A. (Eds.), Seismic and Acoustic Velocities in Reservoir Rocks: Recent Developments. SEG, pp. 1–23.

Wang, Z., Nur, A., 1988. Effect of temperature on wave velocities in sands and sandstones with heavy hydrocarbons. SPE Reserv. Eng. 154–168. doi:10.2118/15646-PA

White, J.E., 1975. Computed Seismic Speeds and Attenuation in Rocks With Partial Gas Saturation. Geophysics 40, 224–232. doi:10.1190/1.1440520

White, J.E., Mikhaylova, N.G., Lyakhovitskiy, F.M., 1975. Low-frequency seismic waves in fluid-saturated layered rocks. Earth Phys. 44–52.

Winkler, K.W., Murphy III, W.F., 1995. Acoustic Velocity and Attenuation in Porous Rocks, in: Ahrens, T.J. (Ed.), Rock Physics and Phase Relations: A Handbook of Physical Constants. American Geophysical Union, pp. 20–34. doi:10.1029/RF003p0020

Wyllie, M.R.J., Gregory, A.R., Gardner, G.H.F., 1958. An Experimental Investigation of Factors Affecting Elastic Wave Velocities in Porous Media. Geophysics 459–493.

Appendix A

Porosity measurements

We present here the pore size distribution and porosity for each core sample used in this study and measured from mercury porosimetry test.

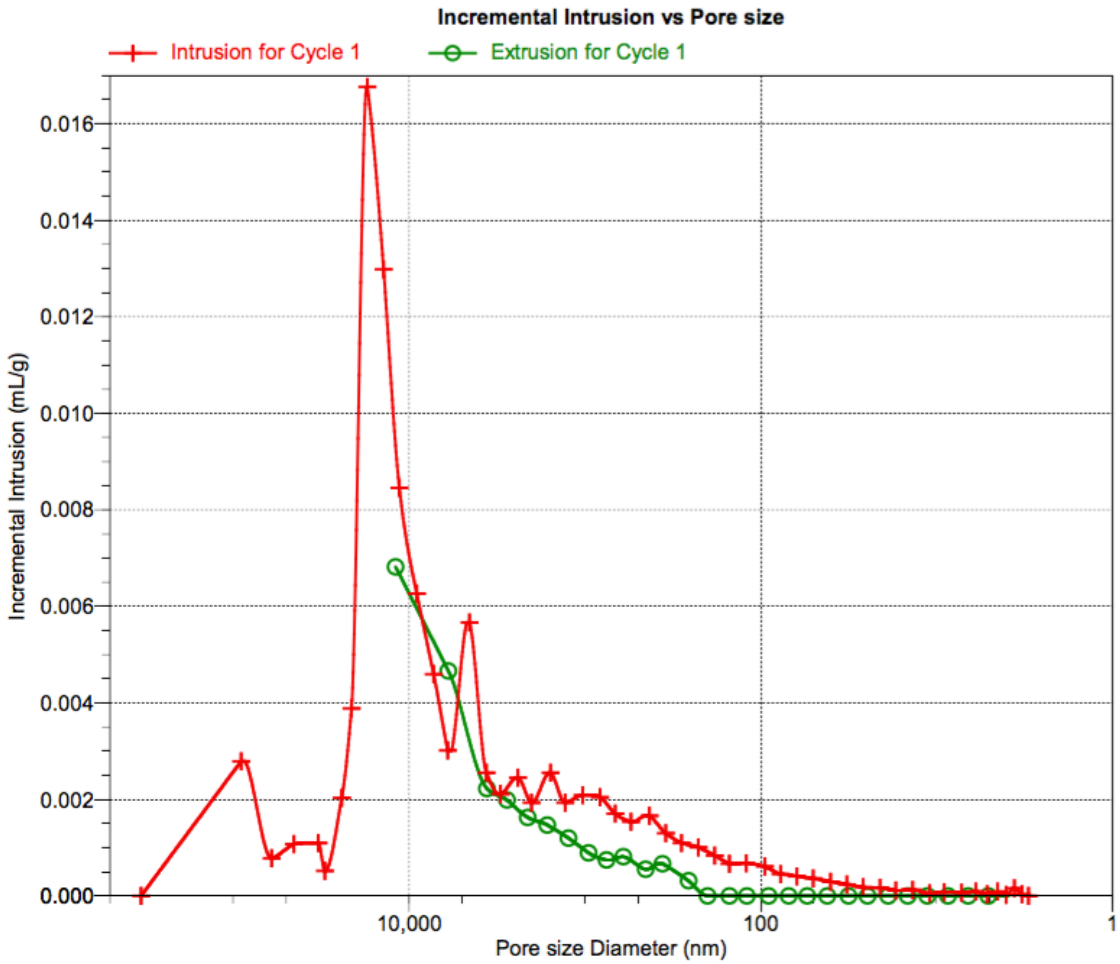

Figure 43. Pore size distribution for core sample 1.

Table 10. Porosity and average pore diameter for core sample 1.

Core Sample Number	Porosity (%)	Average Pore Diameter (µm)
Core Sample 1	22.9279	0.44872

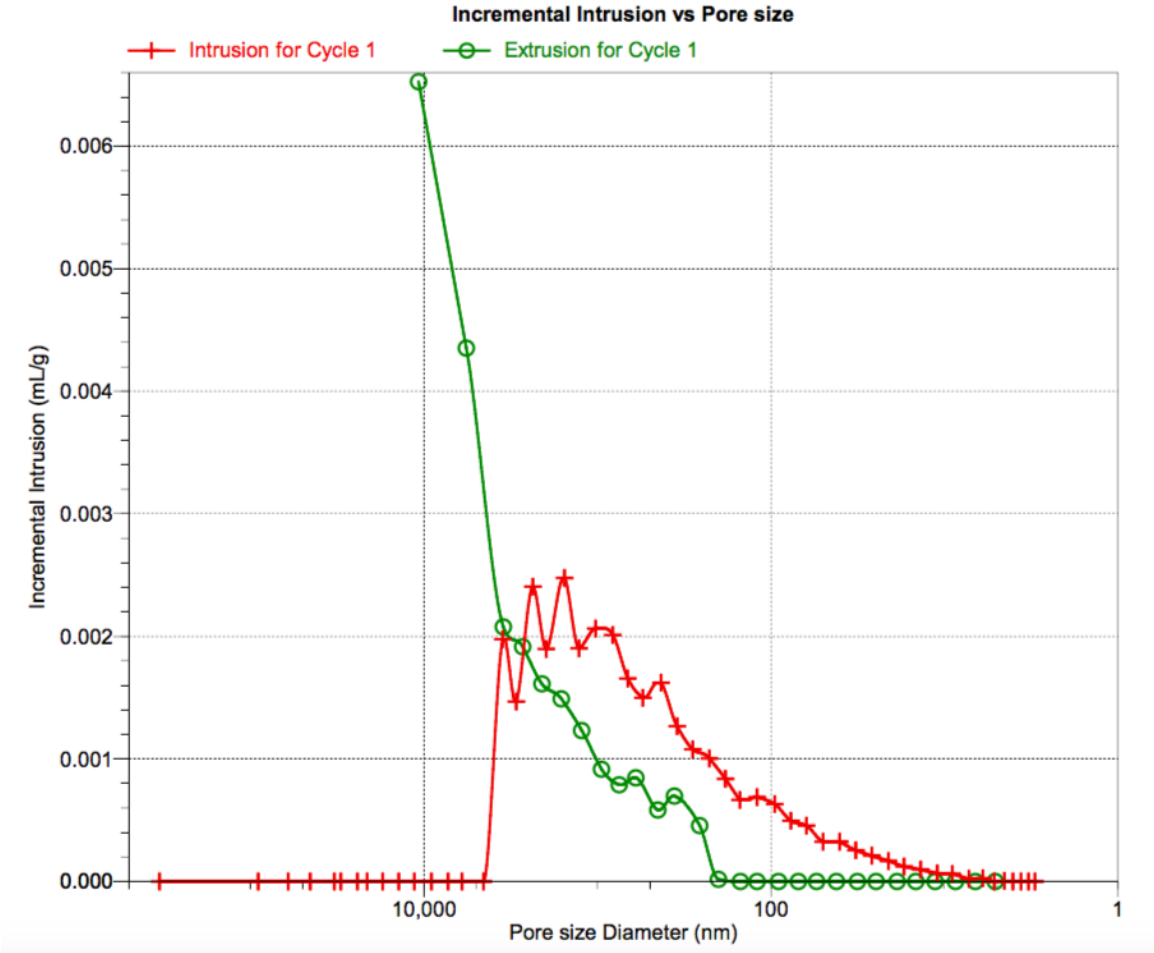

Figure 44. Pore size distribution for core sample 2.

Table 11. Porosity and average pore diameter for core sample 2.

Core Sample Number	Porosity (%)	Average Pore Diameter (µm)
Core Sample 2	6.2562	0.23727

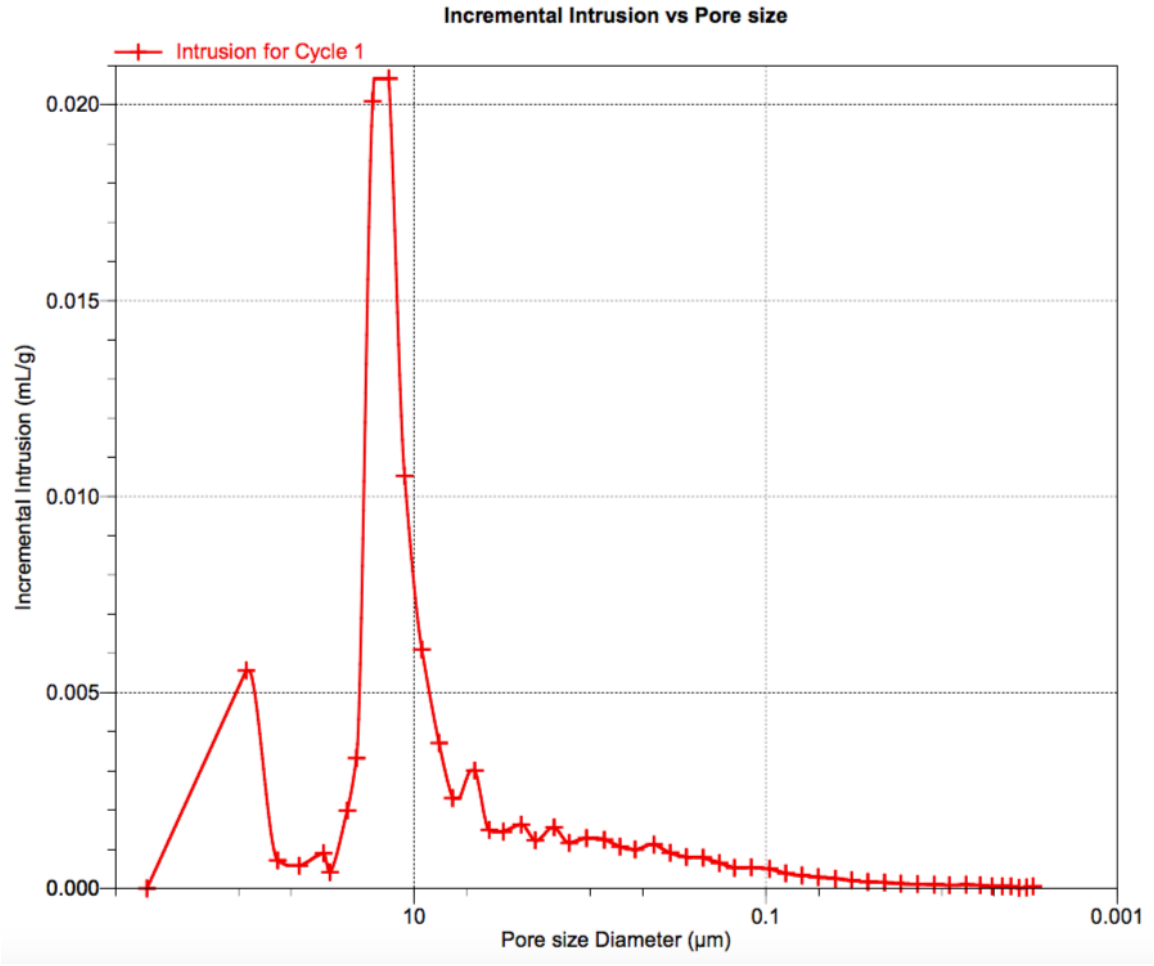

Figure 45. Pore size distribution for core sample 3.

Table 12. Porosity and average pore diameter for core sample 3.

Core Sample Number	Porosity (%)	Average Pore Diameter (µm)
Core Sample 3	21.1693	0.53690

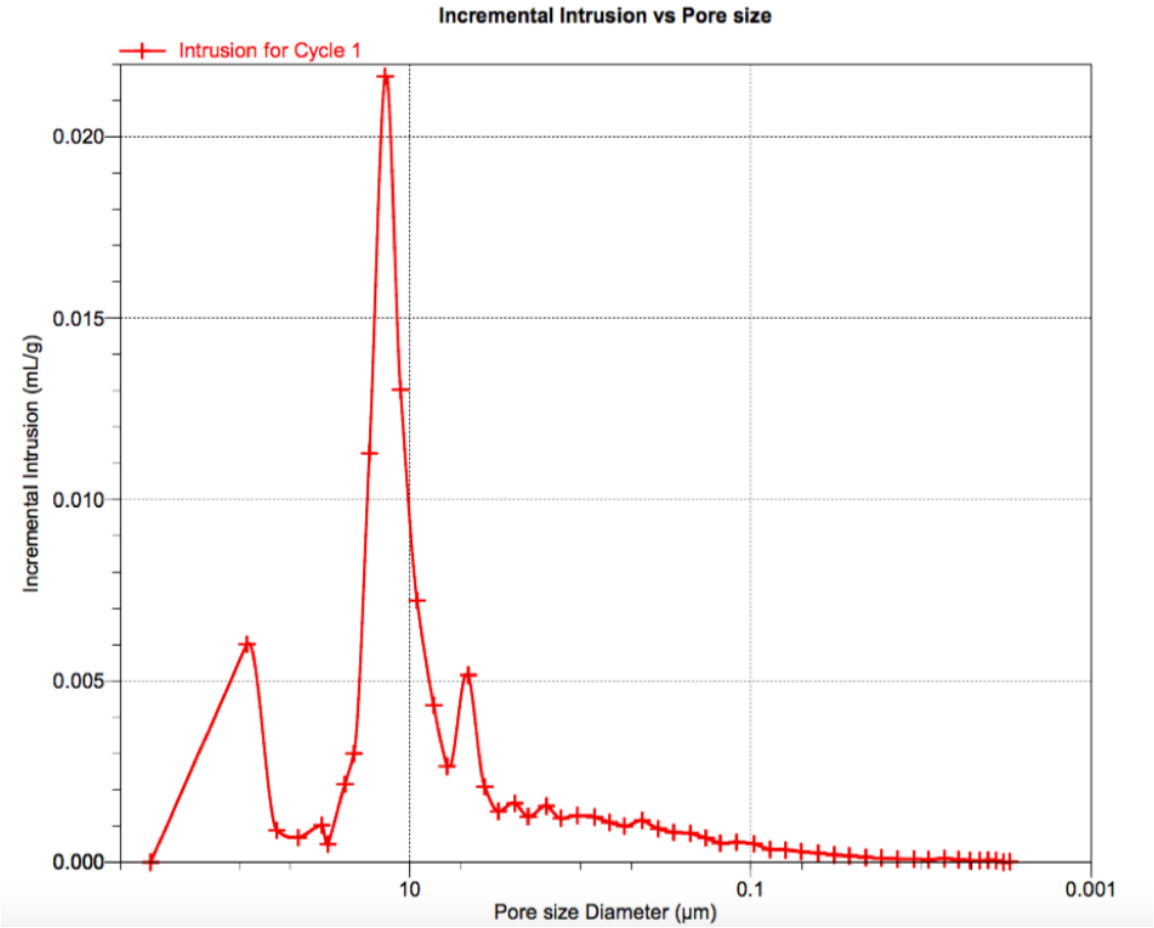

Figure 46. Pore size distribution for core sample 4.

Table 13. Porosity and average pore diameter for core sample 4.

Core Sample Number	Porosity (%)	Average Pore Diameter (µm)
Core Sample 4	21.3098	0.58859

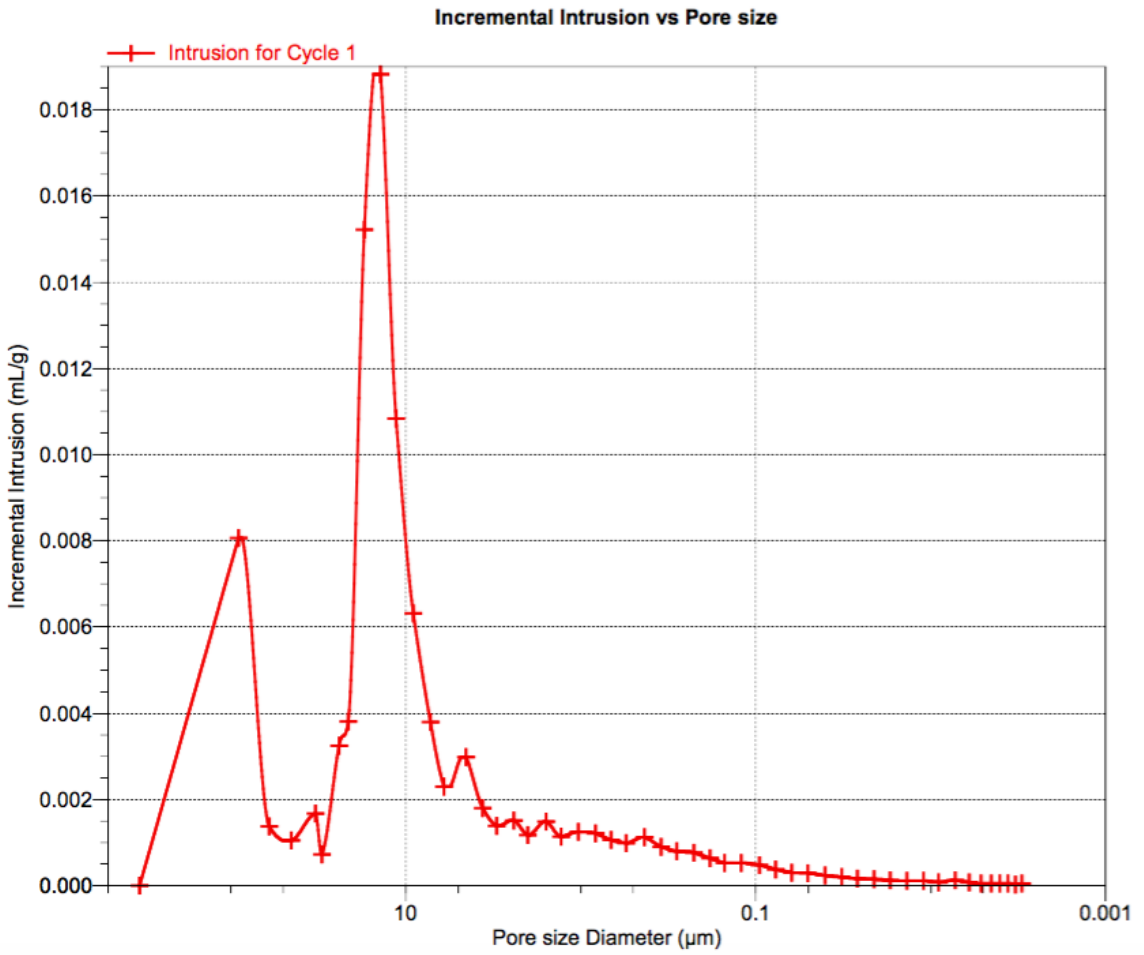

Figure 47. Pore size distribution for core sample 5.

Table 14. Porosity and average pore diameter for core sample 5.

Core Sample Number	Porosity (%)	Average Pore Diameter (µm)
Core Sample 5	21.1023	0.50553

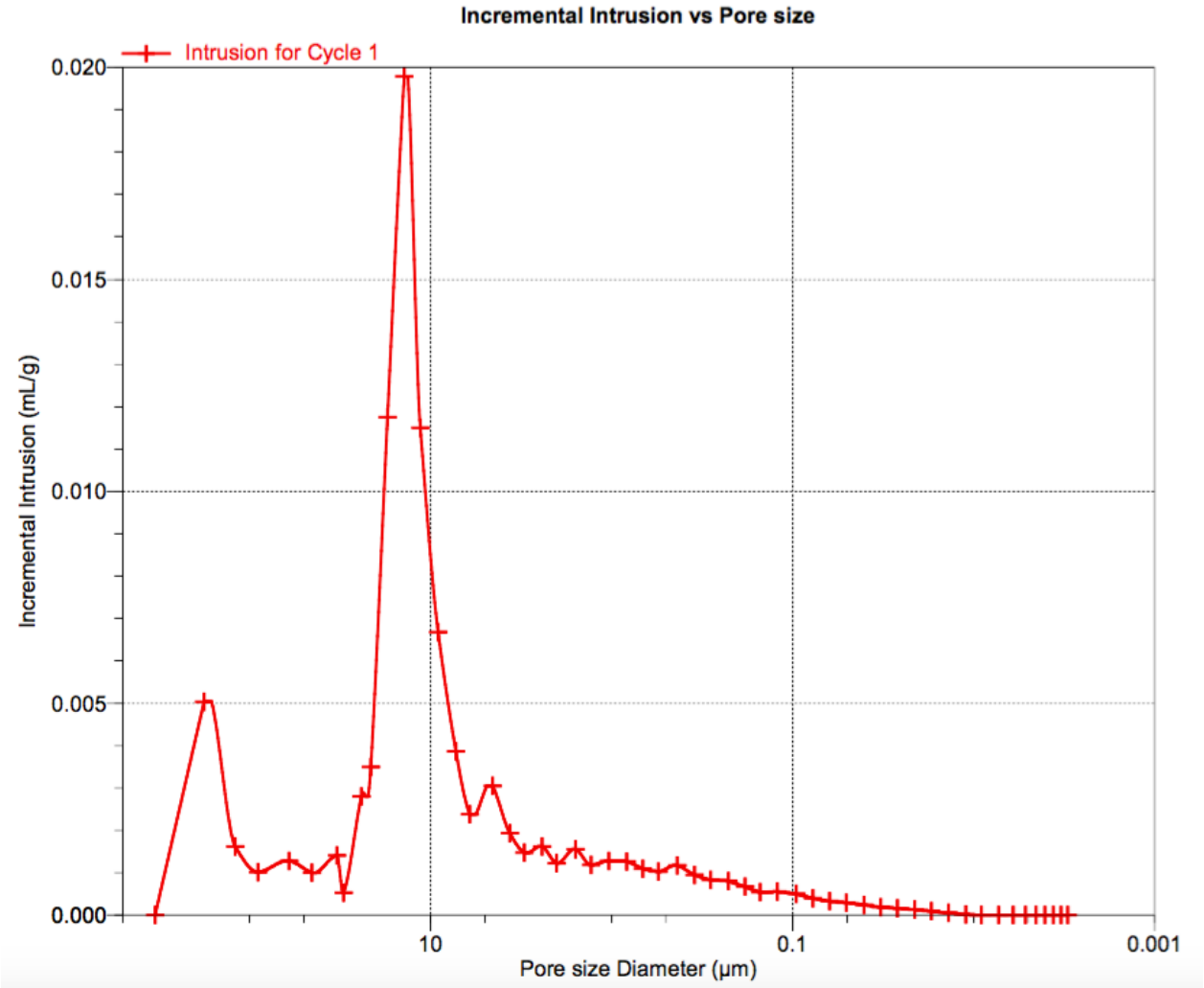

Figure 48. Pore size distribution for core sample 6.

Table 15. Porosity and average pore diameter for core sample 6.

Core Sample Number	Porosity (%)	Average Pore Diameter (µm)
Core Sample 6	20.6546	1.16982

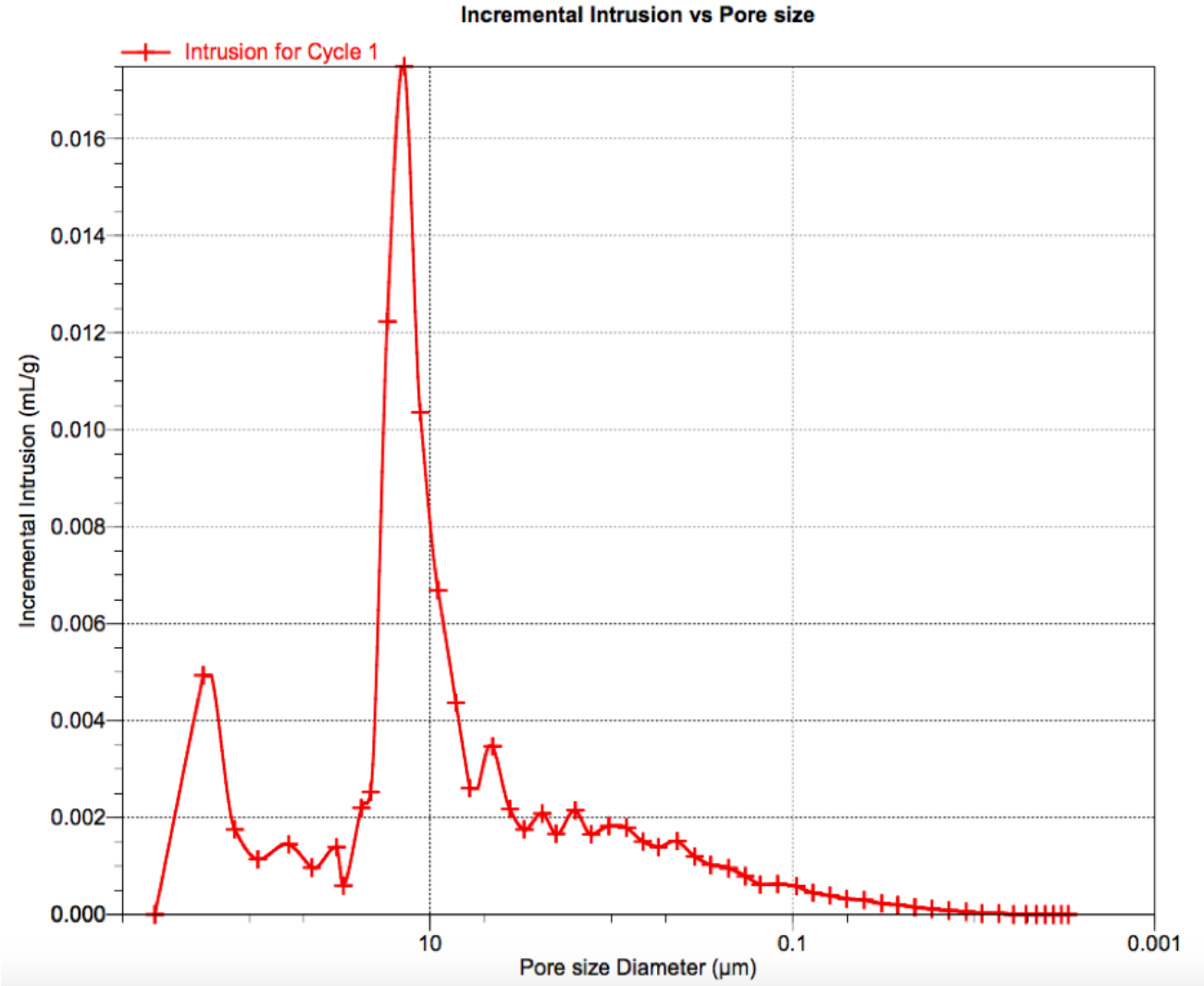

Figure 49. Pore size distribution for core sample 7.

Table 16. Porosity and average pore diameter for core sample 7.

Core Sample Number	Porosity (%)	Average Pore Diameter (µm)
Core Sample 7	21.1524	0.91250

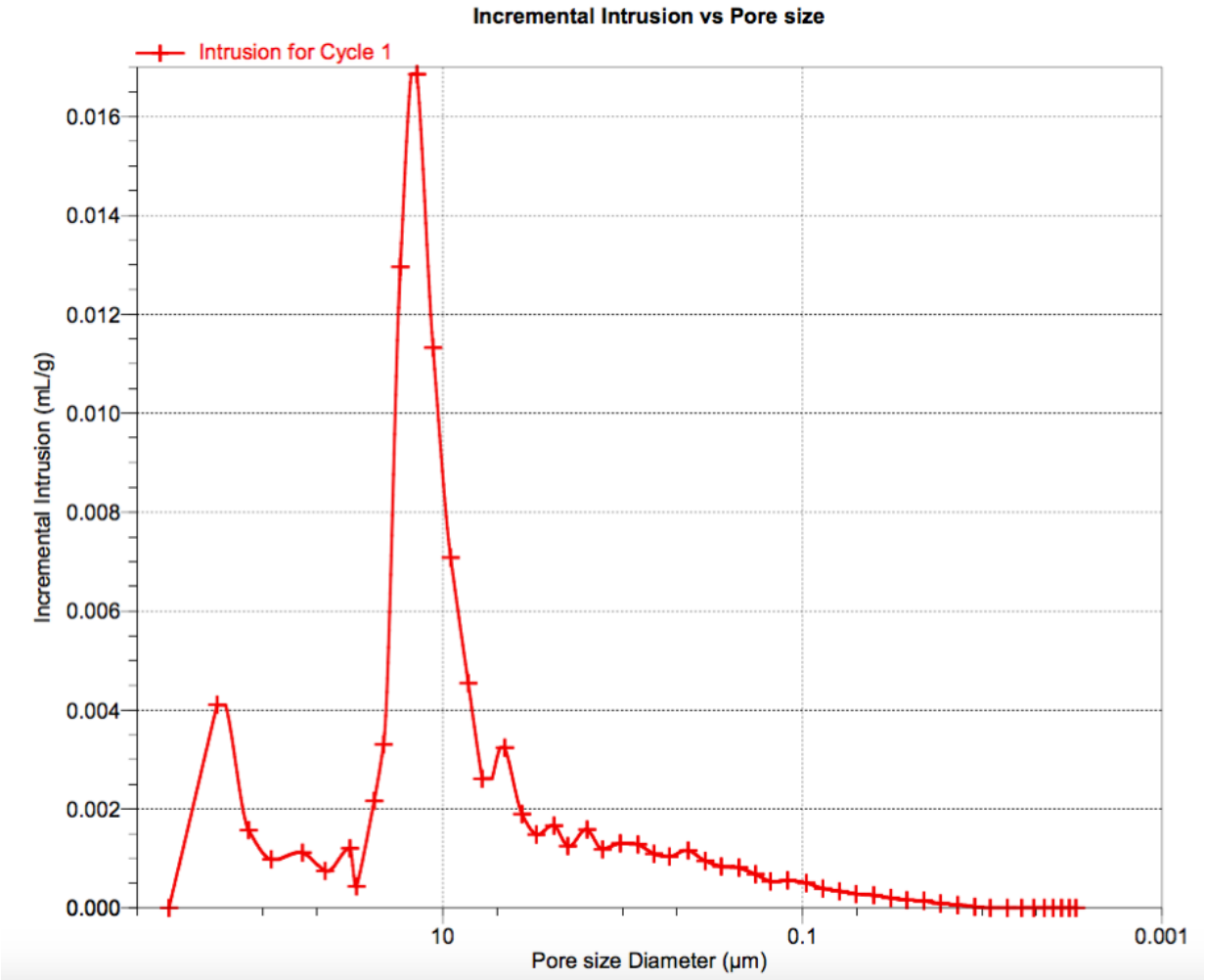

Figure 50. Pore size distribution for core sample 8.

Table 17. Porosity and average pore diameter for core sample 8.

Core Sample Number	Porosity (%)	Average Pore Diameter (µm)
Core Sample 8	19.9519	1.09089

Appendix B

Ultrasonic Results and Sample Characteristics

In this appendix we present in more detail the characteristics of the samples used in this work as well as the ultrasonic results generated for them. The column "Rock pieces" represent which pieces of rock composed that sample, from top to bottom of the sample.

Table 18. Characteristics of the samples tested at 250 kHz and their acoustic wave velocities.

Wave frequency: 250 kHz										
Sample Characteristics								Arrival time (milisec.)	Face to Face Time (milisec.)	Velocities (m/s)
Sample	Rock pieces	Weight (g.)	Ave. Porosity (fraction)	Sw (%)	Density (g./c.c.)	Diameter (mm)	Height (mm)	P-wave	P-wave	Vp
C-1.1	4.1	115.16	0.2131	0%	2.17	51.47	25.56	15.64	4.26	2246.05
C-1.1	4.1	115.16	0.2131	0%	2.17	51.47	25.56	15.68	4.26	2238.18
C-1.1	4.1	115.16	0.2131	0%	2.17	51.47	25.56	15.68	4.26	2238.18
C-1.2	4.4	220.13	0.2131	0%	2.10	51.47	50.45	25.78	4.26	2344.33
C-1.2	4.4	220.13	0.2131	0%	2.10	51.47	50.45	25.82	4.26	2339.98
C-1.2	4.4	220.13	0.2131	0%	2.10	51.47	50.45	25.78	4.26	2344.33

Wave frequency: 250 kHz										
Sample Characteristics								Arrival time (milisec.)	Face to Face Time (milisec.)	Velocities (m/s)
Sample	Rock pieces	Weight (g.)	Ave. Porosity (fraction)	Sw (%)	Density (g./c.c.)	Diameter (mm)	Height (mm)	P-wave	P-wave	Vp
C-1	4.1 / 4.4 / 4.2	450.90	0.2131	2%	2.10	51.47	103.43	50.24	4.26	2249.46
C-1	4.1 / 4.4 / 4.2	450.90	0.2131	2%	2.10	51.47	103.43	50.30	4.26	2246.52
C-1	4.1 / 4.4 / 4.2	450.90	0.2131	2%	2.10	51.47	103.43	50.28	4.26	2247.50
C-4	3.2 / 4.4 / 3.3	464.98	0.2124	47%	2.19	51.47	101.83	46.92	4.26	2387.01
C-4	3.2 / 4.4 / 3.3	464.98	0.2124	47%	2.19	51.47	101.83	46.94	4.26	2385.90
C-4	3.2 / 4.4 / 3.3	464.98	0.2124	47%	2.19	51.47	101.83	46.88	4.26	2389.25
C-5	4.1 / 3.4 / 4.2	478.00	0.2124	49%	2.20	51.47	104.58	47.14	4.26	2438.90
C-5	4.1 / 3.4 / 4.2	478.00	0.2124	49%	2.20	51.47	104.58	47.12	4.26	2440.04
C-5	4.1 / 3.4 / 4.2	478.00	0.2124	49%	2.20	51.47	104.58	47.06	4.26	2443.46
C-9.1	3.3	122.42	0.2117	93%	2.29	51.47	25.72	14.12	4.26	2608.52
C-9.1	3.3	122.42	0.2117	93%	2.29	51.47	25.72	14.16	4.26	2597.98
C-9.1	3.3	122.42	0.2117	93%	2.29	51.47	25.72	14.18	4.26	2592.74
C-9.2	3.4	246.88	0.2117	95%	2.30	51.47	51.6	23.52	4.26	2679.13
C-9.2	3.4	246.88	0.2117	95%	2.30	51.47	51.6	23.54	4.26	2676.35
C-9.2	3.4	246.88	0.2117	95%	2.30	51.47	51.6	23.52	4.26	2679.13
C-9	3.2 / 3.4 / 3.3	491.73	0.2117	94%	2.28	51.47	103.85	43.70	4.26	2633.11
C-9	4.1 / 3.4 / 4.2	491.73	0.2117	94%	2.28	51.47	103.85	43.60	4.26	2639.81
C-9	4.1 / 3.4 / 4.2	491.73	0.2117	94%	2.28	51.47	103.85	43.56	4.26	2642.49

Table 19. Characteristics of the samples tested at 100 kHz and their acoustic wave velocities.

Wave frequency: 100 kHz										
Sample Characteristics								Time to arrival (milisec.)	Face to Face Time (milisec.)	Velocities (m/s)
Sample	Rock pieces	Weight (g.)	Ave. Porosity (fraction)	Sw (%)	Density (g./c.c.)	Diameter (mm)	Height (mm)	P-wave	P-wave	Vp
C-1	8.1 / 8.4 / 8.2	449.10	0.1995	0%	2.09	51.47	103.07	51.88	5.24	2209.91
C-1	8.1 / 8.4 / 8.2	449.10	0.1995	0%	2.09	51.47	103.07	51.68	5.24	2219.42
C-1	8.1 / 8.4 / 8.2	449.10	0.1995	0%	2.09	51.47	103.07	51.62	5.24	2222.29
C-2	8.1 / 5.4 / 8.2	467.39	0.2053	37%	2.17	51.47	103.37	54.98	5.24	2078.21
C-2	8.1 / 5.4 / 8.2	467.39	0.2053	37%	2.17	51.47	103.37	54.94	5.24	2079.88
C-2	8.1 / 5.4 / 8.2	467.39	0.2053	37%	2.17	51.47	103.37	54.56	5.24	2095.90
C-3	5.1 / 8.4 / 5.2	466.48	0.2053	38%	2.17	51.47	103.3	53.48	5.24	2141.38
C-3	5.1 / 8.4 / 5.2	466.48	0.2053	38%	2.17	51.47	103.3	53.54	5.24	2138.72
C-3	5.1 / 8.4 / 5.2	466.48	0.2053	38%	2.17	51.47	103.3	53.52	5.24	2139.60
C-4	3.2 / 8.4 / 3.3	468.89	0.2056	49%	2.19	51.47	102.74	47.56	5.24	2427.69
C-4	3.2 / 8.4 / 3.3	468.89	0.2056	49%	2.19	51.47	102.74	47.66	5.24	2421.97
C-4	3.2 / 8.4 / 3.3	468.89	0.2056	49%	2.19	51.47	102.74	47.54	5.24	2428.84
C-5	8.1 / 3.4 / 8.2	472.20	0.2056	49%	2.20	51.47	103.31	47.30	5.24	2456.25
C-5	8.1 / 3.4 / 8.2	472.20	0.2056	49%	2.20	51.47	103.31	47.14	5.24	2465.63
C-5	8.1 / 3.4 / 8.2	472.20	0.2056	49%	2.20	51.47	103.31	46.84	5.24	2483.41

Wave frequency: 100 kHz										
Sample Characteristics								Time to arrival (milisec.)	Face to Face Time (milisec.)	Velocities (m/s)
Sample	Rock pieces	Weight (g.)	Ave. Porosity (fraction)	Sw (%)	Density (g./c.c.)	Diameter (mm)	Height (mm)	P-wave	P-wave	Vp
C-6	3.2 / 8.1 / 3.3 / 8.2	470.19	0.2056	49%	2.19	51.47	103.09	46.78	5.24	2481.70
C-6	3.2 / 8.1 / 3.3 / 8.2	470.19	0.2056	49%	2.19	51.47	103.09	46.72	5.24	2485.29
C-6	3.2 / 8.1 / 3.3 / 8.2	470.19	0.2056	49%	2.19	51.47	103.09	46.82	5.24	2479.32
C-7	5.1 / 5.4 / 5.2	484.77	0.2110	72%	2.25	51.47	103.6	56.28	5.24	2029.78
C-7	5.1 / 5.4 / 5.2	484.77	0.2110	72%	2.25	51.47	103.6	56.30	5.24	2028.99
C-7	5.1 / 5.4 / 5.2	484.77	0.2110	72%	2.25	51.47	103.6	56.36	5.24	2026.60
C-8	3.4 / 8.2 / 3.2	481.84	0.2087	73%	2.25	51.47	102.98	45.24	5.24	2574.50
C-8	3.4 / 8.2 / 3.2	481.84	0.2087	73%	2.25	51.47	102.98	45.20	5.24	2577.08
C-8	3.4 / 8.2 / 3.2	481.84	0.2087	73%	2.25	51.47	102.98	45.12	5.24	2582.25
C-9	3.2 / 3.4 / 3.3	491.99	0.2117	95%	2.30	51.47	102.98	42.80	5.24	2741.75
C-9	3.2 / 3.4 / 3.3	491.99	0.2117	95%	2.30	51.47	102.98	42.84	5.24	2738.83
C-9	3.2 / 3.4 / 3.3	491.99	0.2117	95%	2.30	51.47	102.98	42.78	5.24	2743.21